070
wes
str.
m.s.

Structural analysis of the Mariana inner
AC .H3 no.W91 15541
Wessel, Jill K.
SOEST Library

JUN 14 1991

School of Ocean and
Earth Science and Technology
LIBRARY

A Structural Analysis of the Mariana Inner Forearc at 22° N

Jill Kathleen Wessel

A thesis submitted to the Graduate Division of the University of Hawaii
in partial fulfillment of the requirements for the degree of

MASTER OF SCIENCE
in
GEOLOGY AND GEOPHYSICS

AUGUST 1991

THESIS COMMITTEE:

Patricia Fryer, *Chairperson*
Gerard J. Fryer
Brian Taylor

DATE DUE

AUG 0 6 1991			
DEC 1 0 1991			

HIGH SMITH REORDER #45-230

We certify that we have read this thesis and that, in our opinion, it is satisfactory in scope and quality as a thesis for the degree of Master of Science in Geology & Geophysics.

THESIS COMMITTEE

Patricia Fryer
Chairperson

Gerard J. Fryer

Brian Taylor

THIS THESIS IS DEDICATED TO THE MEMORY OF MY MOTHER,

EDITH MORRIS MAHONEY,

WHO INSPIRED MY BROTHERS AND ME TO PURSUE HIGHER EDUCATION

AND TAUGHT US TO WORK TOWARDS OUR DREAMS.

ACKNOWLEDGMENTS

I extend my greatest appreciation to Fred Duennebier, Patty Fryer, John Mahoney, John Sinton and all of those who lobbied for my admittance into the Geology & Geophysics graduate program and for their continued support and belief in my abilities during my years here. I would like to thank Patty for her patience and understanding during the first three years of graduate school during which I was very ill and got little more done than my course homework in the halls of Kaiser after treatments. I would also like to thank my doctors for telling me I'd never walk again and thereby inspiring me to not only give my oral defense standing up, but to run again. I'm grateful to Nancy Hulbirt and Brooks Bays for their aid in the drafting of this thesis. As much as I hate being couped up on a rolling ship, I thank John Sinton and Sandy Shor for the opportunity to go to sea because 1) they paid my salary and 2) it allowed me to travel to remote islands such as Easter and Iceland.

It has been my fortune to have friends and fellow students, to numerous to name here, who have helped me survive the doldrums of graduate school; and past and present office mates—Scott Rowland, Joan Hayashi, James Granahan—who have tolerated my idiosyncrasies. The aid that Paul Anderson, Gerard Fryer, Phil Jarvis, and Pål Wessel gave over the years in my struggles to program is greatly appreciated.

I appreciate the time and helpful suggestions my committee members have given on my thesis. Without the support and guidance from Brian Taylor and Pål Wessel, this thesis would still be in a primitive stage. Finally, the faith, patience, and encouragement my husband, Pål Wessel, has given this final year in graduate school has made all the difference in the quality of my life.

ABSTRACT

Seismic reflection, SeaMARC II acoustic imagery and bathymetric data, covering a region 110 km by 60 km across the northern Mariana island arc, portrays dense, high-angle, normal faulting of the arc and inner forearc. Displacements of less than 10 m and up to 500 m cut a thick sequence of stratified, relatively undeformed sediments. The major faults display a sinuous or zigzag trace commonly associated with rifting and are indicative of a single event of triaxial strain that requires two contemporaneous conjugate pairs in orthorhombic symmetry. Regionally, both the west and east boundary faults of the northern Mariana backarc basin also display the typical zigzag expression of orthorhombic symmetry. Interpretation and statistical analyses of the data show activity since the last sedimentary deposition and concurrent fault development of two distinct fault populations—one associated with the backarc basin's EBF and the other with extension in the forearc. Inspection shows that extensional ridges in the backarc basin have approximately the same trend as the EBF and associated faulting in the survey area. The direction of minimum principal strain for the backarc basin and the EBF at 22° N is estimated at 41° ± 4°, orthogonal to the extensional strain direction measured in the inner forearc. The change in strain is distinct and abrupt, occurring across a 20 km wide zone along the arc massif. Within this "interference region", the intermediate and minimum principal strain directions are nearly equal in magnitude with orientations midway between the dominant forearc trend and backarc basin principal direction. This zone appears to be a region where the stress field is reorienting itself. Analysis shows that the strain from either backarc or forearc regime is not transmitted across this narrow zone, which enables the two incompatible strain regimes to coexist virtually juxaposed in the overriding plate. The formation of two orthogonal extensional fault regimes within the Mariana platelet may be explained by assuming that (1) a weak, neutral zone exists where stresses can be more easily relieved and adjusted for, or (2) that the East boundary fault plane behaves like a "free edge," causing the maximum principal direction of stress (compression) to rotate parallel to the fault plane with proximity. In conclusion, the data support models that require radial forearc deformation resulting from increasing arc-trench curvature of the northern half of the Mariana island arc.

TABLE OF CONTENTS

Acknowledgments iv
Abstract v
List of Tables vii
List of Illustrations ix
Introduction 1
Regional Geology 4
Seismic Reflection, Side-Scan Sonar, Bathymetry and Interpretation 6
Seismic Reflection Data 6
SeaMARC II Data. 11
Data Interpretation Summary. 14
Data Analysis 17
Determining Fault and Lineament Trends 17
Estimating Errors 22
Solving for Multiple Modes 26
Calculating Strain Orientation. 31
Results. 32
Preferred Models and Multiple Modes 32
Data Distribution and Fault Patterns 43
3-D Fault Geometry 46
Principal Strain Directions 47
Discussion and Conclusions 53
Tables 60
Appendix A. 67
Appendix B. 97
References 101

LIST OF TABLES

1a	Preferred model solutions of minor faults and lineaments from zone 1a	60
1b	Preferred model solutions of minor faults and lineaments from zone 1b	60
1c	Preferred model solutions of minor faults and lineaments from zone 2	60
1d	Preferred model solutions of minor faults and lineaments from zone 3	60
2a	Preferred model solutions of major faults from zone 1a	61
2b	Preferred model solutions of major faults from zone 1b	61
2c	Preferred model solutions of major faults from zone 2	61
2d	Preferred model solutions of major faults from zone 3	61
3a	Preferred model solutions of combined faults and lineaments from zone 1a	62
3b	Preferred model solutions of combined faults and lineaments from zone 1b	62
3c	Preferred model solutions of combined faults and lineaments from zone 2	62
3d	Preferred model solutions of combined faults and lineaments from zone 3	62
4a	Summary of preferred models of minor faults and lineaments from zone 1a	63
4b	Summary of preferred models of minor faults and lineaments from zone 1b	63
4c	Summary of preferred models of minor faults and lineaments from zone 2	63
4d	Summary of preferred models of minor faults and lineaments from zone 3	63
5a	Summary of preferred models of major faults from zone 1a	64
5b	Summary of preferred models of major faults from zone 1b	64
5c	Summary of preferred models of major faults from zone 2	64
5d	Summary of preferred models of major faults from zone 3	64
6a	Summary of preferred models of combined faults and lineaments, zone 1a	65
6b	Summary of preferred models of combined faults and lineaments, zone 1b	65
6c	Summary of preferred models of combined faults and lineaments, zone 2	65
6d	Summary of preferred models of combined faults and lineaments, zone 3	65
7	Mode and strain orientations	66
A-1a	Synthetic data one-mode solutions	92
A-1b	Synthetic data two-mode solutions	92
A-1c	Synthetic data three-mode solutions	92
A-1d	Synthetic data four-mode solutions	92
A-2	Summary of synthetic solution models	92

A-3a Solution I one-mode model 93
A-3b Solution I two-mode model 93
A-3c Solution I three-mode model 93
A-4 Summary of solution I models 93
A-5a Solution II one-mode model 94
A-5b Solution II two-mode model 94
A-5c Solution II three-mode model 94
A-5d Summary of solution II models with background noise. 94

LIST OF ILLUSTRATIONS

1	Location of the Mariana island arc	2
2	Location of the survey area in the northern Mariana island arc	3
3	Mixed frequency seismic reflection profiles of survey area	7
4a	3-D Interpretation of seismic reflection profiles looking north	9
4b	3-D Interpretation of seismic reflection profiles looking south	10
5	SeaMARC II side-scan sonar acoustic image of survey area	13
6	SeaMARC II bathymetry of survey area	15
7	Geological interpretation of the survey area	16
8	Interpretation map of faults and lineaments divided into zones	18
9	Interpretation map of minor faults and lineaments	20
10	Interpretation map of major faults	21
11a	Estimating the error in azimuth from the layover effect	24
11b	Schematic diagram of worst case error in azimuth in the forearc	24
12a	Error in azimuth estimated from combined uncertainties	25
12b	Cumulative error in bin length	25
13a	Histograms of oriented data from zone 1a	27
13b	Histograms of oriented data from zone 1b	28
13c	Histograms of oriented data from zone 2	29
13d	Histograms of oriented data from zone 3	30
14a	Residuals for zone 1a	33
14b	Residuals for zone 1b	34
14c	Residuals for zone 2	35
14d	Residuals for zone 3	36
15a	Sector diagrams of oriented data from zone 1a	37
15b	Sector diagrams of oriented data from zone 1b	38
15c	Sector diagrams of oriented data from zone 2	39
15d	Sector diagrams of oriented data from zone 3	40
16a	Areally correct sector diagram.	41
16b	Visually distorted sector diagram	41
17	Schematic convolution of data distributions.	44
18	Zigzag geometry of boundary faults	48
19	Estimating the bias in extension direction about local trends	50
20	Strain ellipses for combined faults and regional trends	51
21	Strain ellipses for major faults and regional trends	52
22	Extensional ridges in the backarc basin at 22° N.	54
23	Strain regime across the northern Mariana island arc.	55
A-1a	Histogram of synthetic data	73
A-1b	Sector diagram of synthetic data	74
A-2a	Histogram of synthetic data with solutions	75
A-2b	Sector diagram of synthetic data with solutions	76
A-3a	Location of sample area	78
A-3b	Fault data used in real-life example	79
A-4a	Opposite angle sector diagram of fault data	80
A-4b	Double angle sector diagram of fault data	81
A-5a	Histogram of real data solutions I	83
A-5b	Residual distribution from real data solutions I	84

A-6a Histogram of real data solutions II. 86
A-6b Residual distribution from real data solutions II 88
A-7 Sector diagram of real data solutions II. 89

INTRODUCTION

With the advent of plate tectonics, deep earthquakes associated with island arcs were explained as major zones of convergence and downward movements of lithospheric plates [*Isacks et al.*, 1968; *Oliver and Isacks*, 1967]. Simplistically, regional compression was thought to be the natural expression of plate convergence [*Chase*, 1978]. This basic model assumed the axis of maximum compressive stress was parallel to the motion of the subducting slab and the axis of least compressive stress was perpendicular to the trench for non-oblique subduction [*Isacks et al.*, 1968]. However, extensional basins behind island arcs, tensional earthquakes observed along subduction zones, and variations in island arc shapes were some of the first clues that convergent margins could not easily be explained by a first order plate-tectonic model.

The substantial differences between arc-trench systems have been attributed to differences in tectonic environment, duration of subduction, convergence rate and angle, buoyancy of aseismic ridges on the subducting plate, and other factors [e.g., *Jarrard*, 1986; *Vogt et al.*, 1976]. In the evolution of an island arc, subduction related stresses may change with time as well as location along strike, subjecting forearc regions to variable deformation and metamorphism [*Fryer et al.*, 1990; *Hussong and Uyeda*, 1981].

Lying east of the Philippines and south of Japan, the Mariana island arc borders the southeast edge of the Philippine plate above the subducting Pacific plate (Figure 1). Acoustic and bathymetric SeaMARC II data collected by the R/V Kana Keoki (KK830116 leg 4; Figure 2) of the northern Mariana island arc has been reprocessed, analyzed, and interpreted along with single channel, mixed frequency and 3.5 kHz seismic reflection records to map the structure across the arc at 22° N. Analysis of the intense normal faulting of the inner forearc reveals yet another facet of island arc systems.

The goal of this study was to determine if the densely faulted region of the inner forearc and volcanic arc at 22° N was the result of a change in stress regime in this region that was either temporal or spatial in nature, or simply the sinuous expression of unimodal extension. To investigate this, I have mapped in detail the fault and lineament distribution over 1° of island arc crust and undertaken a statistical analysis of the dominant trends of these oriented features, from which the direction of maximum extensional strain is estimated. This study shows that two distinct fault populations are the manifestation of opposing and orthogonal extensional strain regimes within the Mariana platelet. The distinct partitioning of strain occurs across a narrow 20 km wide zone along the arc massif.

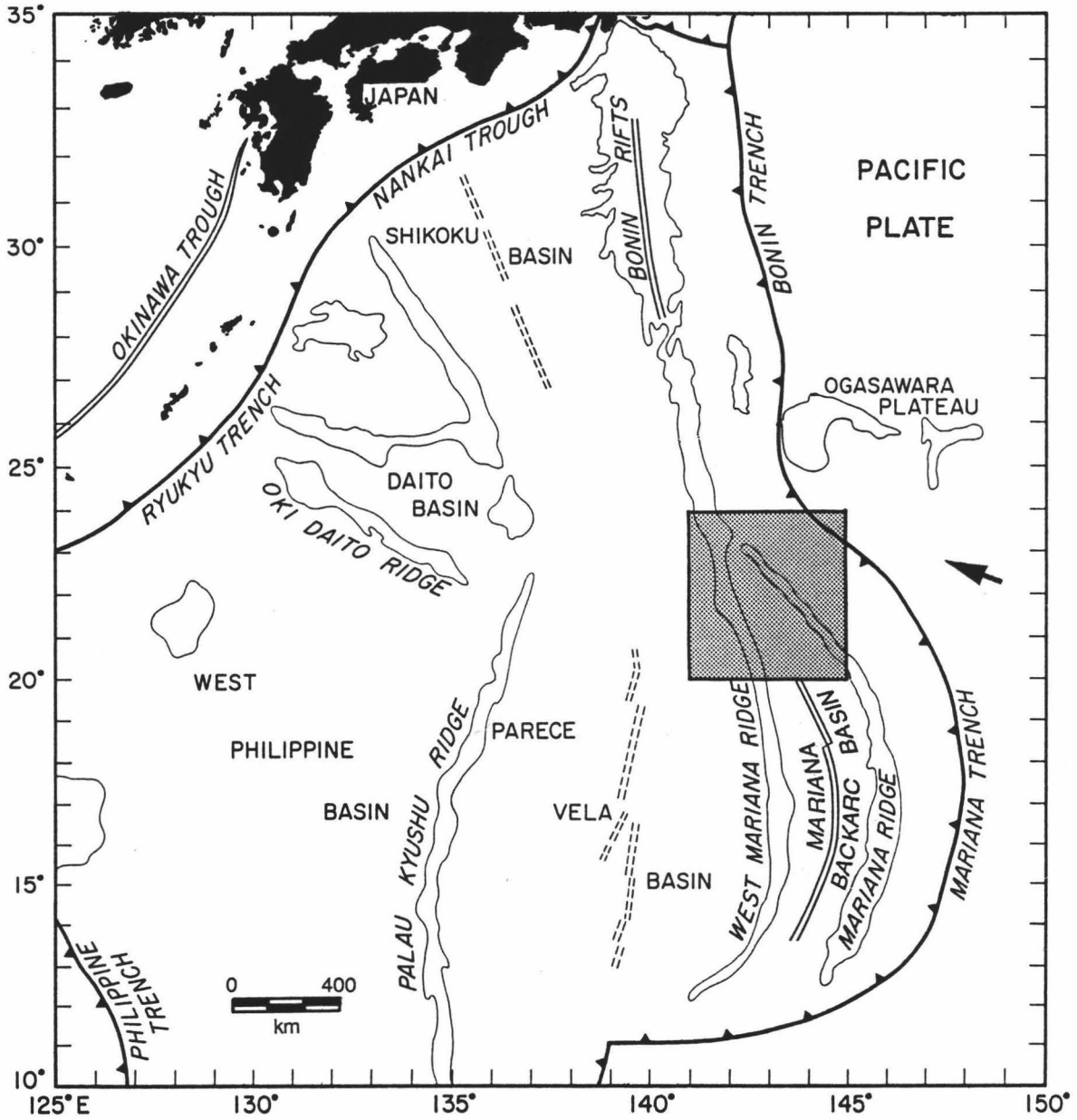

Fig. 1. Tectonic setting and location of the Mariana island arc. The arrow shows the motion of the subducting Pacific plate. The shaded region shows the location of Figure 2.

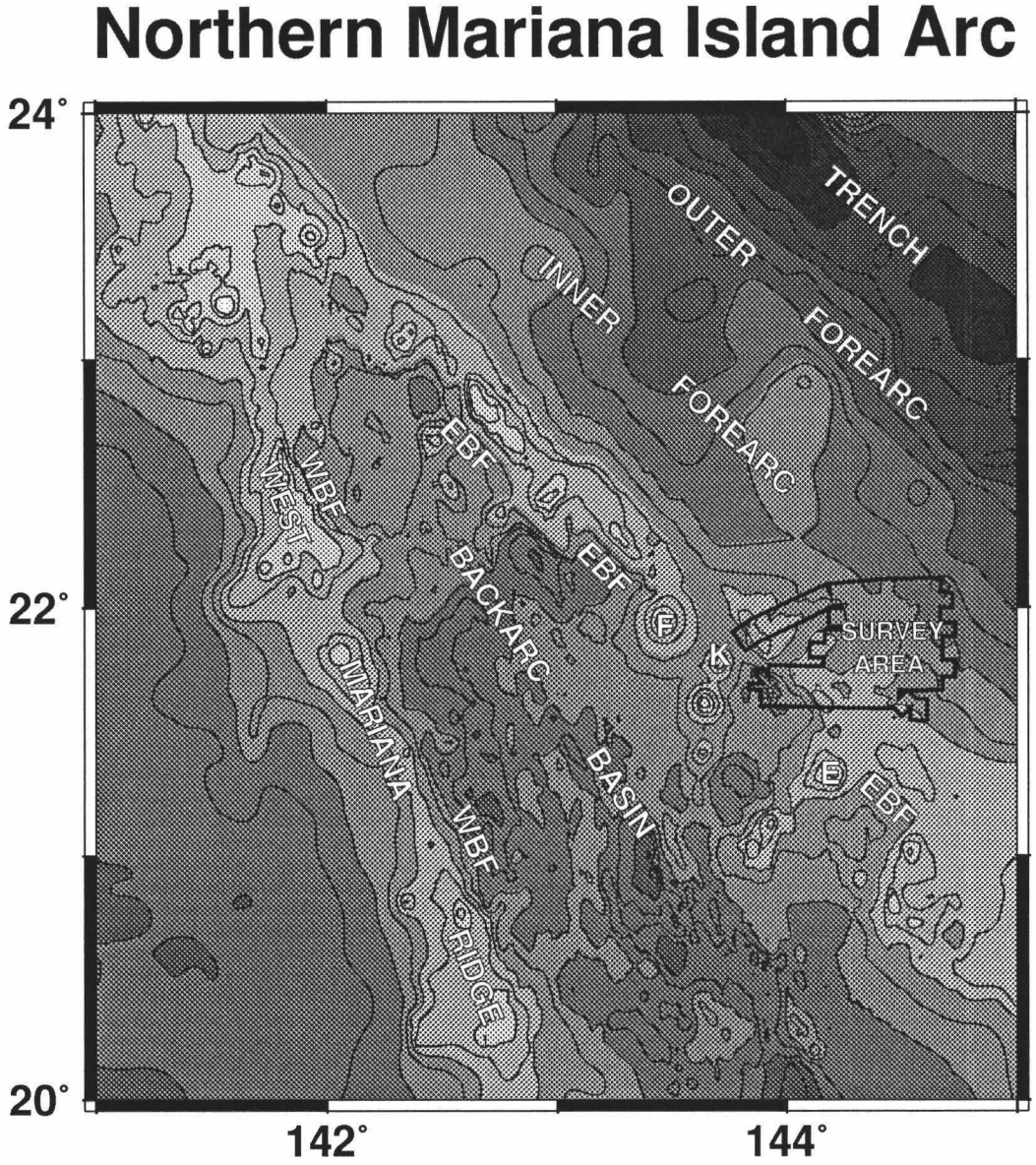

Fig. 2. The location of the survey area in the northern Mariana island arc is shown by the heavy outline. Bathymetry is compiled from 3.5 kHz echograms and SeaMARC II data in the area. Contour interval is 100 m. The nearby submarine volcanoes are labeled as F for Fukujin, K for Kasuga and its associated volcanic cross-chain, E for Eifuku and its associated volcanic cross-chain. The East boundary fault (labeled EBF), along which the volcanic arc trends, marks the division between the backarc basin and the forearc. The West boundary fault (labeled WBF) delineates the west margin of the Mariana backarc basin.

The analysis implies that arc-parallel stretching of the northern half of the Mariana forearc is occurring, and that the Mariana backarc basin at 22° N may be undergoing active, basin-wide extension, rather than localized deformation and organized spreading.

REGIONAL GEOLOGY

The Mariana island arc is bound by two aseismic ridges—the Marcus-Necker (or Michelson) Ridge, which includes the Ogasawara Plateau in the north, and the Caroline Ridge in the south (Figure 1). The Mariana magmatic arc lies 190-220 km west of the Mariana trench and is comprised of 15 small islands and many active submarine volcanoes [*Cloud et al.*, 1956]. The islands of Guam, Rota, Tinian, and Saipan comprise a portion of uplifted forearc 20 km east of the magmatic arc. The larger volcanic islands lie along the central part of the arc between 17° to 20° N. To the north and south, volcanism is submarine.

The larger seamounts north of 20°, such as Fukujin and Nikko, have summits at depths less than 500 m and some are recently active [*Jackson*, 1989; *Smoot*, 1988; *Stern et al.*, 1990]. Kaitoku at 26° N and Fukutoku-oba-no-ba at 24.75° N have had phreatic explosive eruptions in which the volcano broke the sea surface and was later eroded [*Smoot*, 1988]. Discolored water, upwelling and floating lapilli have been observed during these eruptions [*Smoot*, 1988]. At depths greater than 3100 m, the pressure becomes too great to allow explosive submarine eruptions [*Cas and Wright*, 1987]. On the other hand, near surface and subaerial explosive eruptions in the Mariana and other island arcs have, in the past, shown the ability to produce ash plumes that deposit substantial volumes of sediment, but the area of coverage is unknown (personal communication, Rowland, 1991). The implication is that although there are no islands and the submarine volcanoes sit on backarc basin floor within the vicinity of the surveyed area, some sedimentation of the forearc may have been possible over the last 3 Ma.

The Mariana backarc basin is a mature rift graben extending more than 1300 km in length from 12° N to about 24° N where the West Mariana Ridge, a remnant arc, and the active Mariana Ridge join to form the Volcano arc. This basin is bounded by two rift flank uplifts—the West boundary fault borders the eastern margin of the West Mariana Ridge and the East boundary fault, hereafter called the EBF, bounds the western edge of the Mariana Ridge. As the arc volcanoes grow, usually beginning on the down-dropped side of the EBF, they eventually bury it. The northern portion of the Mariana backarc basin is

structurally distinct from the central and southern portions. At 22° N the spreading center is not well-defined and by 23° N it is unidentifiable [*Beal*, 1987; *Stern et al.*, 1990].

Detailed bathymetry reveals lineaments that cross the backarc basin at a highly oblique angle to its strike and have an apparent alignment to cross chain volcanoes along the Mariana ridge and to cross trends along the East Mariana Ridge [*Hussong and Fryer*, 1983; *Karig et al.*, 1978; *Smoot*, 1990]. These features appear to be sediment filled fracture zones with an extensional component [*Eguchi*, 1984; *Karig et al.*, 1978; *Smoot*, 1990] and whose orientation varies from north to south along the length of the backarc basin [*Karig et al.*, 1978; *Smoot*, 1990]. One such lineament occurs at 21° N along the trend of the Eifuku volcanic cross-chain and the forearc faults in the study area [*Beal*, 1987; *Eguchi*, 1984].

At 20° N, the relative motion of the Pacific plate with respect to the Philippine plate is 4.4 cm/yr towards 300°, nearly tangent to the Mariana trench [*Eguchi*, 1984]. Some of the variables contributing to the strain regime in the overriding plate include convergence direction and rate [*Jarrard*, 1986]. The overall horizontal strain on the overriding plate is likely to depend more on the horizontal component of coupling than on local magnitude of coupling. Rapid strain changes occur in the overriding plate along the subduction zone as well as over time [*Jarrard*, 1986].

Numerous models deal with the opening of the Mariana backarc basin and the curvature associated with this arc-trench system. *Stern et al.* [1984] proposed that the Mariana backarc basin was opening by northward "unzipping" of the Izu-Bonin-Volcano arc. The propagator tip is at 23.5° N according to the model of *Stern et al.* [1984]. Predictions from the Newtonian flow model of *Hsui and Youngquist* [1985] give an excellent fit to the curvature of the Mariana trench and account for the paleomagnetic rotations of Guam and Saipan. According to their model, deformation should be uniform along the forearc. They suggest that the northward termination of the Mariana backarc basin is a consequence of slower spreading resulting from the collision of the arc-trench system with the Ogasawara plateau at 26° N. This model requires anticlockwise rotation of the northern forearc and, to accommodate extension of the forearc, normal faulting perpendicular to the arc trend. The buoyant, aseismic Michelson Ridge together with the large Ogasawara Plateau abutting the trench at 26° N is hypothesized to be resisting subduction and in essence "pinning" the Mariana subduction zone at its northern end [*Hsui and Youngquist*, 1985; *Karig et al.*, 1978; *Vogt et al.*, 1976]. Whereas *Vogt et. al.* [1976] and *Hsui and Youngquist* [1985] hypothesize that the Mariana trench is pinned at both ends, *Karig et. al.* [1978] believes the south behaves as a "free" end in which the large strike-slip features south of Guam

accommodate the arc parallel extensional strain in the platelet produced by increased arc curvature over the evolutionary course of the Mariana island arc.

"Trench rollback" can affect the state of stress in the overriding plate. Hinge migration or "rollback" is the seaward retreat of the subduction hinge under the influence of gravity [*Carlson and Melia*, 1984; *Carlson and Mortera–Gutierrez*, 1990; *Dewey*, 1980; *Molnar and Atwater*, 1978]. Hinge migration has been proposed to explain extensional backarc basin development [e.g., *Carlson and Melia*, 1984; *Molnar and Atwater*, 1978] if the overriding plate does not compensate for the retreat of the subduction zone [*Malinverno and Ryan*, 1986]. *Jarrard* [1986] calculated a seaward rollback for the Mariana trench. Analysis by *Carlson and Melia* [1984] and *Carlson and Mortera–Gutierrez* [1990], however, show that the seaward direction of the rollback is relative; the hinge is advancing westward (landward) slower than the Philippine plate is retreating west. They calculate a variable rate of hinge migration westward along the Izu-Bonin-Mariana arcs with a large increase from the central Mariana trench at 18° N to the Ogasawara Plateau at 27° N. Their model predicts increased curvature of the arc and arc parallel extension [*Carlson and Mortera–Gutierrez*, 1990].

SEISMIC REFLECTION, SIDE-SCAN SONAR, BATHYMETRIC DATA AND INTERPRETATION

Seismic Reflection Data

Mixed frequency (20-50/70-200 Hz) single channel and 3.5 kHz seismic reflection data were collected during the SeaMARC II survey. Although unmigrated sections do not reveal the true geometries of subsurface structures, there is still some information to be extracted. Faults are indicated on the mixed frequency profiles in Figure 3 by point source diffractions that are generally hyperbolic near the sediment-water interface. The density of hyperbolae, on both the mixed frequency and the 3.5 kHz records, and offset horizons on the mixed frequency sections indicate intense faulting throughout the entire survey area. Diffractions originating from faults striking at less than about 75° to the line of profile or at depth tend to lose their hyperbolic character making them more difficult to recognize [*Tucker and Yorston*, 1973] on the seismic records. Final geologic interpretation was based on the correlation of the seismic reflection data with SeaMARC II data.

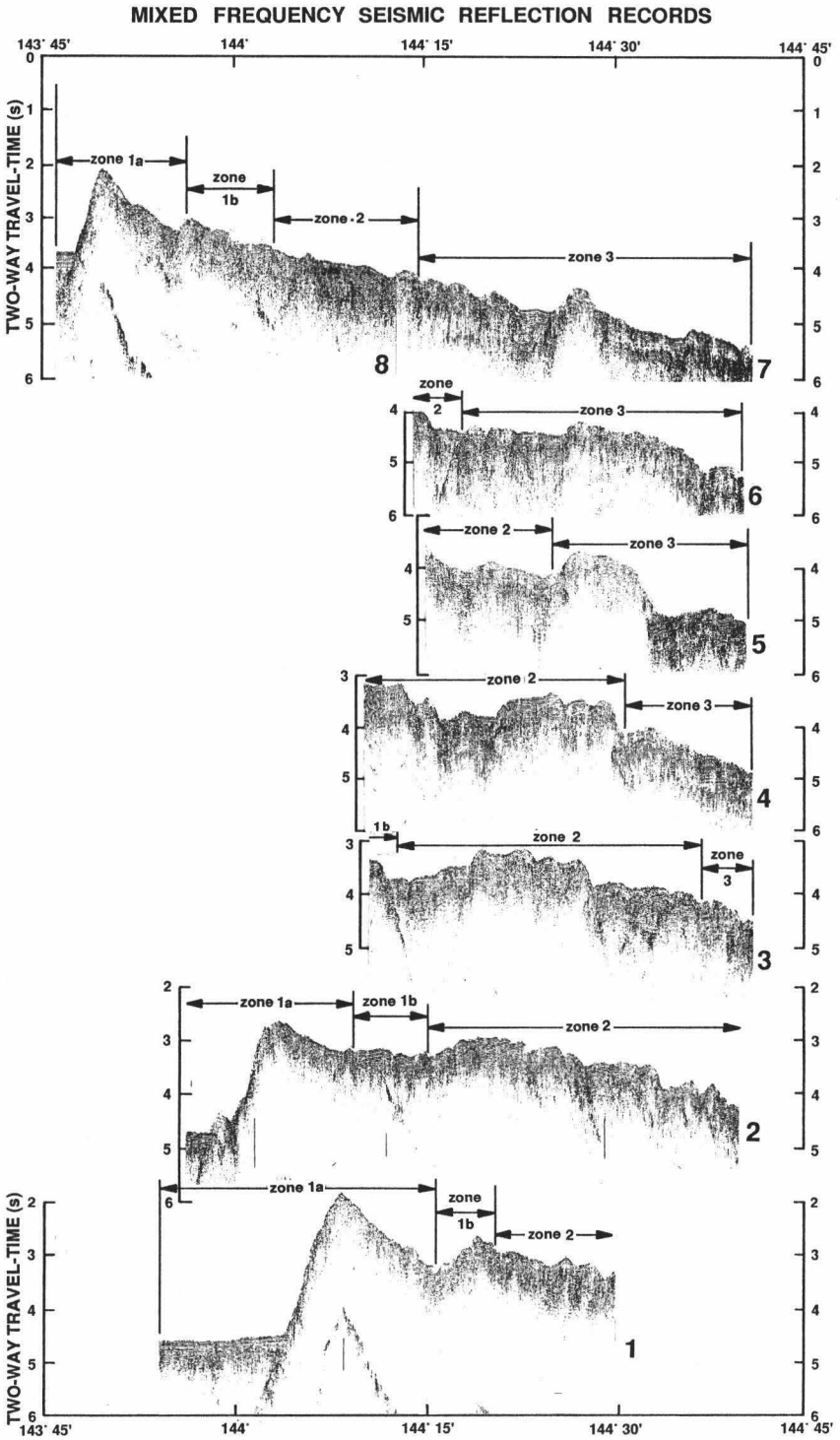

Fig. 3. Mixed frequency seismic reflection profiles of the area surveyed. The profiles are numbered from 1 (southernmost) to 8. From left to right note the flat backarc basin floor, the steep face of the EBF, the back slope of its hanging wall, and the more gently sloping, but intensely faulted inner forearc. The region was divided into 4 zones for a statistical study. Note: profiles 1, 2, and 8 show the break in slope of the back slope of the EBF's hanging wall, where the eastern boundary for zone 1a was chosen. Vertical exaggeration is 10x.

The error associated with fault dip measurements from these unmigrated profiles can be quite significant as a result of the inability of the seismic section to show depth points from steeply dipping reflectors in their correct spatial position [*Tucker and Yorston*, 1973]. Using a combination of echograms, mixed frequency reflections, and SeaMARC II bathymetry the direction of dip can, nevertheless, be determined (Figure 4a). All faults show normal dip-slip motion with no evidence of strike-slip or reverse-slip motion. I assume that the faults are high-angle simply from the intensity and close spacing of the faulting.

The strong bubble pulse in the seismic reflection data and intense faulting make it difficult to determine the subsurface geometry. Ringing multiples from the bubble pulse will mimic horizontal horizons [*Tucker and Yorston*, 1973]. The multibles in the survey area are predominantly horizontal and probably representative of fairly flat-lying sediment horizons that are relatively undistorted except where offset by faulting. Occasional fault blocks have been tilted with later deposition of sediment creating angular unconformities (see lines 1, 2 and 3 in Figure 4a). There appears to be some fault-block rotation along listric faults (see the west end of line 2 in Figure 4a), however this interpretation is speculative because the subsurface geometry is distorted in unmigrated sections. Line 2 shows the beginning of a horst and graben which becomes well developed in lines 3 through 5, then begins to bifurcate in lines 6 and 7. Energy was lost beyond 1 second (two-way travel time) before acoustic basement was penetrated. Sub-bottom horizons suggest that faulting has been active in the past as well as the present during the ongoing process of sedimentation of the forearc. Lines 3, 7, and 8 show fractured horizons with a later deposition of sediments which, in turn, have been faulted, perhaps by continued movement along the lower, sub-surface faults (Figure 4b).

The relationship of echo character to sediment type on 3.5 kHz reflection profiles varies from region to region because of the affect of micro-topography and the acoustic nature of the material [*Damuth*, 1975; 1980]. The final interpretation of sediment type depends on environment. The 3.5 kHz echograms have uniform echo character throughout the surveyed area consisting of indistinct bottom echoes averaging .02 seconds (two-way travel time) of penetration with no sub-bottom reflectors. In the backarc basin and the small basins and sediment traps of the forearc the bottom echoes are prolonged and horizontal. Between these areas are numerous, irregular and closely spaced hyperbolae of

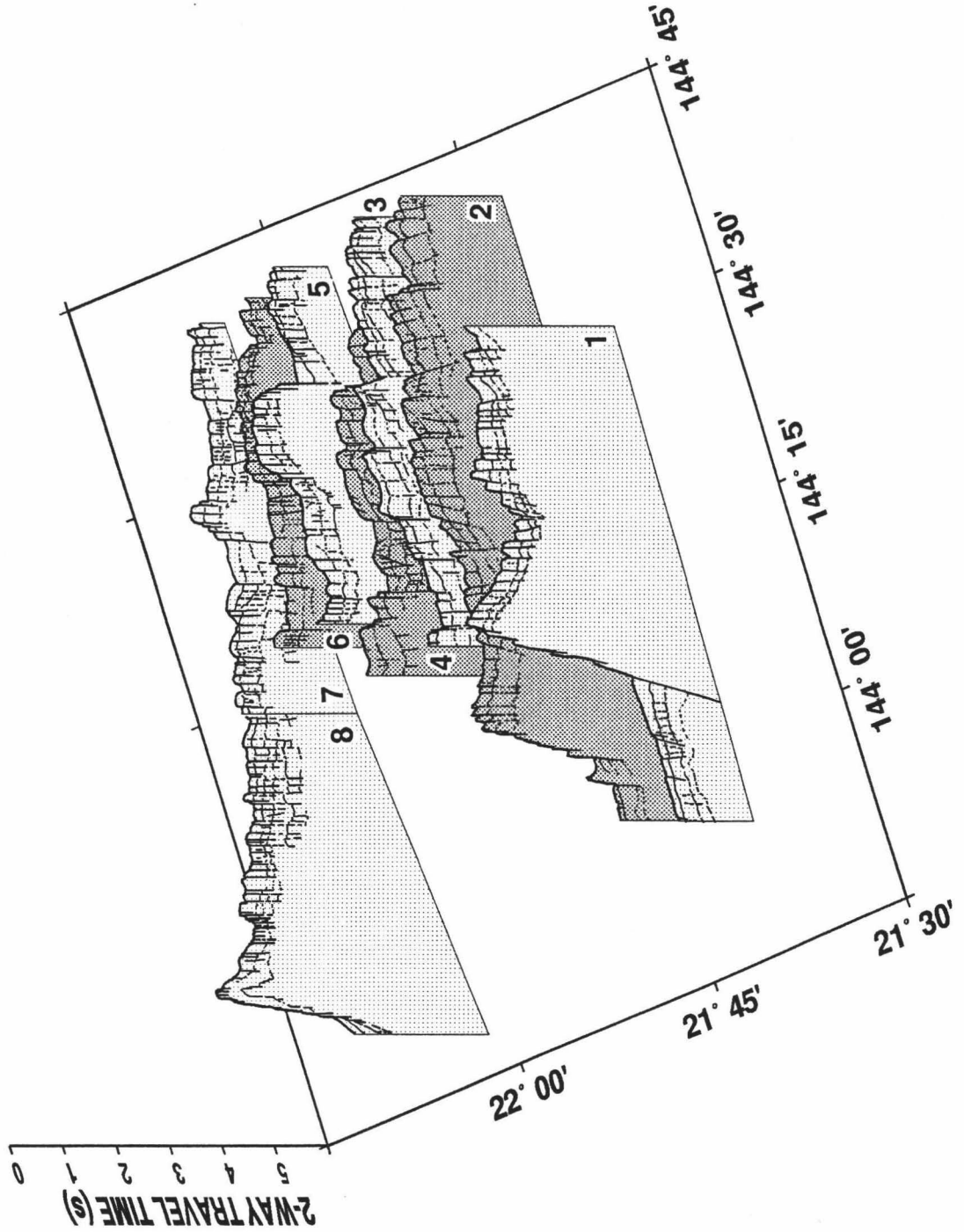

Fig. 4a. Interpretation of seismic reflection profiles in a 3-D perspective looking north. Vertical exaggeration is 10x. The forearc displays intense, high angle, normal faulting of flat lying sedimentary horizons. Note the somewhat listric fault blocks in profile 2.

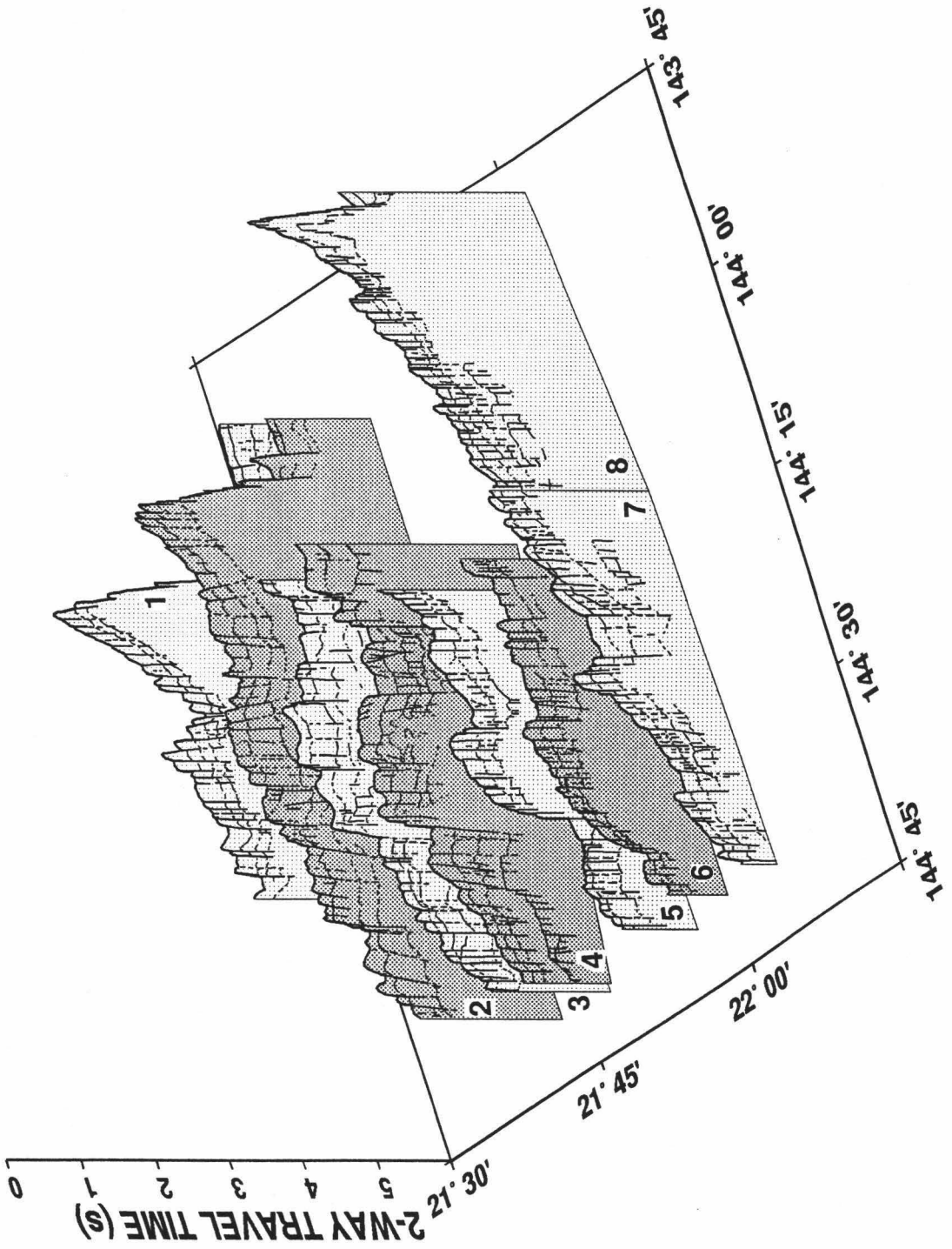

Fig. 4b. The same as figure 4a only looking south. The interpreted subsurface horizons are more visible from this perspective. Note the flower structure and possible intrusions in profile 4 and the horsts and grabens structures crossing the forearc.

varying size having the same indistinct bottom echoes. Regions of rugged micro-topography generally return hyperbolic echoes [*Belderson et al.*, 1972; *Damuth*, 1980], but in the survey area the hyperbolae result from numerous faults.

Three echo types characterize most oceanic basins and have been correlated to the distribution and relative abundance of sediments. One of these is the indistinct, prolonged bottom echoes with no sub-bottom reflectors that is found throughout the survey area. This echo character is indicative of regions of large amounts of silt/sand [*Damuth*, 1980]. Therefore the sediment in this region is interpreted to be a thick sequence of unconsolidated volcanoclastics. All the data show that these sediments are intensely faulted with the majority of faults breaking the surface. Vertical offsets were measured off the 3.5 kHz sections ranging from 5 m to 780 m. No sediment draping is evident on the reflection records. Evidence of strike-slip motion could not be identified, nor any significant compressional features, with the single exception of a local feature in Line 4 (west end, Figure 4b) which exhibits a "flower structure" with small scale folding and minor reverse faults. This is possibly the result of uplift from an intrusion or a strike-slip component to a fault obliquely crossing the ship track, but it represents a very minor component of strike-slip motion at the most. In the center of Line 3 a minor fold appears to be caused by the rotation along a listric extensional fault, and not from compression (Figure 4b).

The same indistinct and prolonged bottom echoes with no sub-bottom reflectors found throughout the survey suggests that the surface sediment is of uniform lithology from the backarc basin into the forearc. Throughout the surveyed area numerous normal faults have recently displaced horizontally lying sediment. The vast majority of faults observed in the seismic sections break the surface of these sediment horizons. 3.5 kHz records reveal very little variation in penetration depth (between 0.01-0.005 seconds, two-way travel time) indicating an even distribution of unconsolidated sediments, suggestive of contemporaneous development among fault populations. The forearc features a series of variably-sized horsts and grabens.

SeaMARC II Data

The SeaMARC II side-scan sonar produces an acoustic image based on back-scattered and specularly reflected sound. The resultant image is thus a combination of scattering by micro-bathymetry of the seafloor and mirror-like reflections from essentially smooth facets facing the towfish. A mosaic of the side-scan sonar acoustic image is displayed in Figure

5. During processing of the side-scan image, local contrast stretching was applied every 15 minutes to enhance the small scale features throughout the survey.

The final side-scan sonar image ultimately has what *Johnson and Helferty* [1990] call "instrumental" resolution that is range and orientation dependent. The resolution varies with distance from nadir, depression angle, and the texture-orientation of a feature. Pixel overlap reduces this resolution, and affects across-track resolution because an acoustic target must be unique to one pixel in order to be resolved [*Johnson and Helferty*, 1990]. Overlap near the center of the swath is the greatest, decreasing towards the edge. Along track the overlap increases towards the distal edges causing images and their shadows to appear elongated parallel to the track line. Therefore, at best, a feature measuring tens of meters in linear dimension is resolvable in the side-scan sonar image. For a feature of unfavorable orientation (perpendicular to the ship's track) and at the distal end of the swath, the resolution might approach 100 m [*Johnson and Helferty*, 1990]. The central horst in Line 5 shows several faults with throws of less than 20 m on the seismic reflection profiles, but they are not resolvable and probably cross perpendicular to the track line on the side-scan sonar image.

In the side-scan sonar image of the survey area, five different acoustic characters are identified. The most prominent and abundant features are those of fault planes having distinct returns with a large specular component and strong backscatter. These faults are often accompanied by acoustic shadows (white on the image), depending on the view direction of the towfish relative to the feature. Between the faults lie very light gray expanses resulting from weak acoustic returns in which much of the signal was diffracted away from the towfish. Such areas are interpreted as smooth, uniform, unconsolidated sediment. Stronger backscatter—the darker grey, grainy patches—are the result of either small scale bathymetric undulations in sedimented areas, or, in some cases, "volume reverberation" [*Johnson and Helferty*, 1990; *Vogt and Tucholke*, 1986]. The latter is common in areas where thick sediment has accumulated and sound is reflected from sub-bottom interfaces and scattered from small-scale inhomogeneities within the sub-bottom sediments. Several volcanic features along the EBF and in the forearc can be recognized by strong acoustic returns from the ensonified side of circular bathymetric highs, and associated acoustic shadows. These are interpreted as volcanic cones. Younger, unsedimented lava flows associated either with volcanic structures or faults, contribute much backscattered energy from surface micro-reflectivity, which appears almost black in the acoustic image. Patches of strong backscatter interspersed in areas of weak backscatter

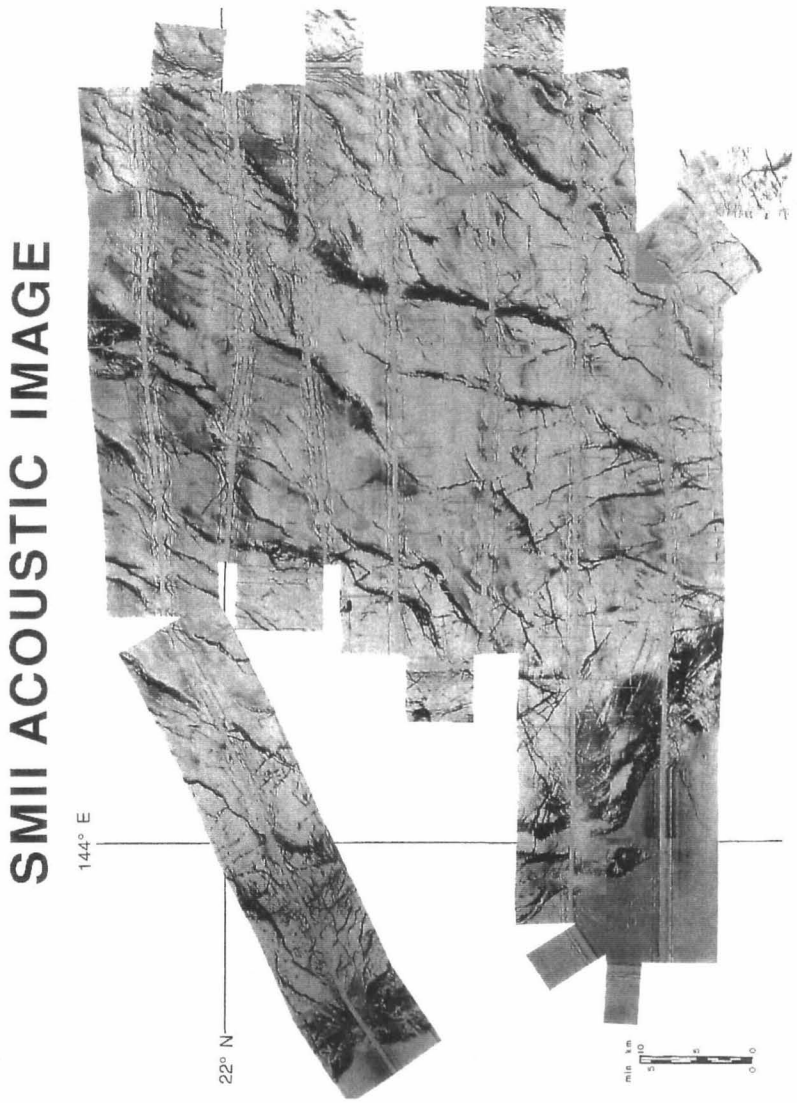

Fig. 5. SeaMARC II side-scan sonar acoustic image of the surveyed area at 22°N. The side-scan is plotted so that the amplitude of returned acoustic energy corresponds to a grey scale in which strong returns approach the black end and weak returns approach the white end of the spectrum. The side-scan data in this image was contrast stretched on a "local" basis. This type of processing enhances the fine scale features in the data allowing for better structural interpretation, but does not allow a comparison of acoustic signal strength from features across the region [*Sender et al.*, 1989].

are found in association with volcanic structures and faults. These features have been interpreted as either older, partially sedimented flow fields or regions of hummocky topography. The blotchy pattern, found along steeper slopes or at the base of faults on the acoustic image, is generated by variable weak and strong returns and interpreted as debris slumps.

The backarc basin in the survey area is characterized by uniform backscatter with occasional slight variations producing faint undulations in the acoustic image that may represent buried faults, sediment waves, or short channels in a flat and smoothly sedimented basin. Several small faults with offsets of 15 m and less on the seismic reflection records contrast little with the surrounding sediment and are therefore virtually invisible on the side-scan sonar image. The acoustic character of the EBF is one of alternating soft and hard acoustic reflectors (creating a blotchy pattern on the image) from the presence of debris and interspersed extrusive flows associated with faults in the walls of the escarpment and with small volcanic structures built on the slopes of the EBF.

The evidence is very scarce as to the relative age of the EBF versus the faulting in the forearc. The offset relationships of one group of faults over another is inconsistent. Comprising each dominant trend are sinuous major faults, that become somewhat anastomosing towards the mid-forearc. There is no evidence of overprinting, of older more heavily sedimented areas, or of cross-cut features in order to form this sinuous pattern. As is common in rift environments, sinuous (or zigzag) fault development appears to be synchronous and have a fairly equal distribution of opposing dips.

Noise in the starboard side of the SeaMARC II towfish during data collection has reduced the resolution of the bathymetry to the order of hundreds of meters, whereas the side-scan sonar data were relatively unaffected and therefore have a much better resolution (tens of meters; Figure 6). The bathymetry has been heavily filtered to reduce the noise level and therefore has lost much detail, but the trends of the major faults and the horst and grabens in the forearc are discernable. The along track lows at the swath edges are artifacts created by occasional bad pings (returns).

Data Interpretation Summary

The geologic interpretation in Figure 7 was based on the backscatter characteristics of the side-scan sonar image, single channel, mixed frequency seismic reflection records, and SeaMARC II bathymetry. Fault throws were measured from 3.5 kHz echosounder records

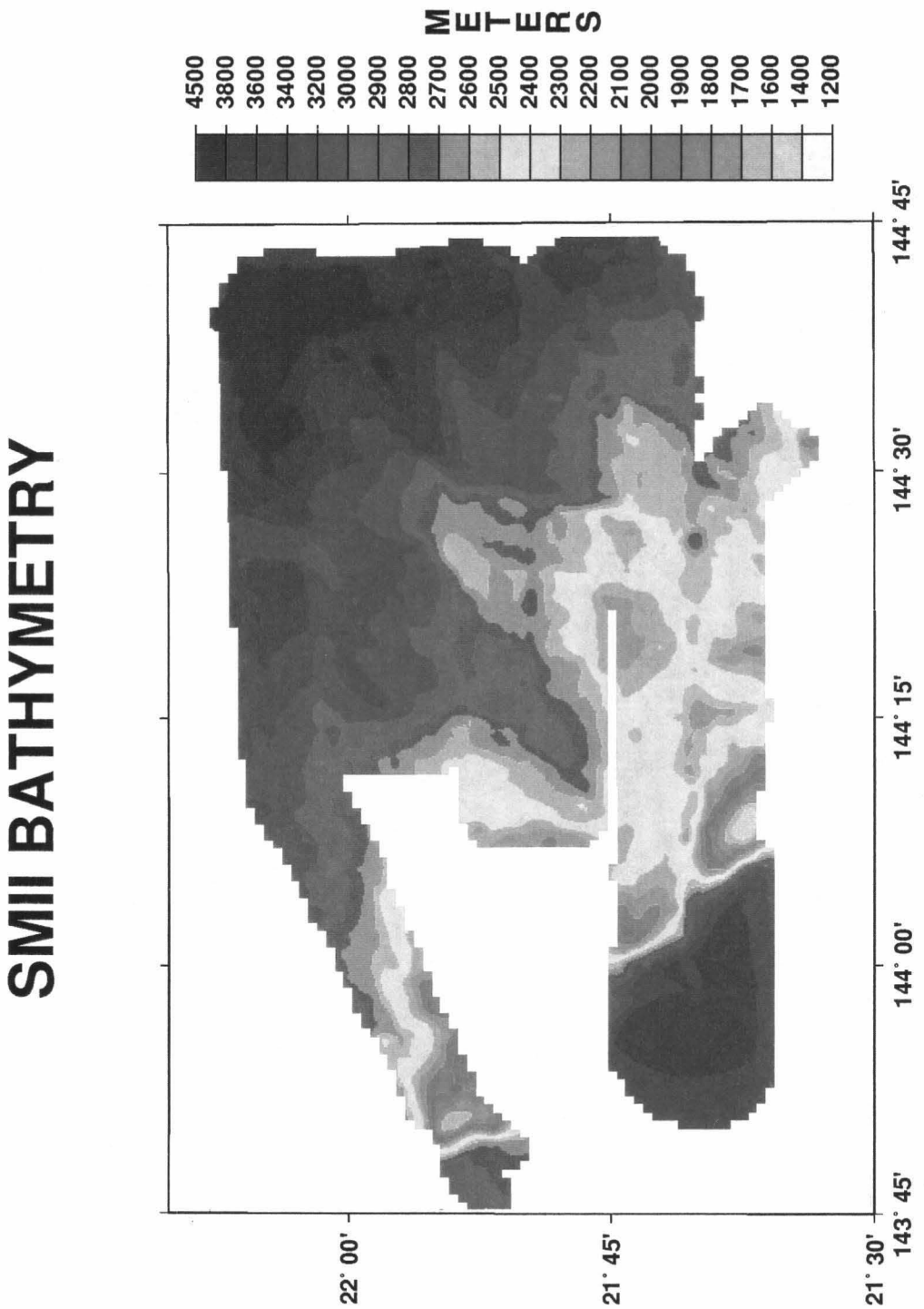

Fig. 6. SeaMARC II bathymetry of the survey area. Contour interval is 100 m. Noise in the starboard side introduced during data collection resulted in reduced resolution and along track artifacts at the swath edges.

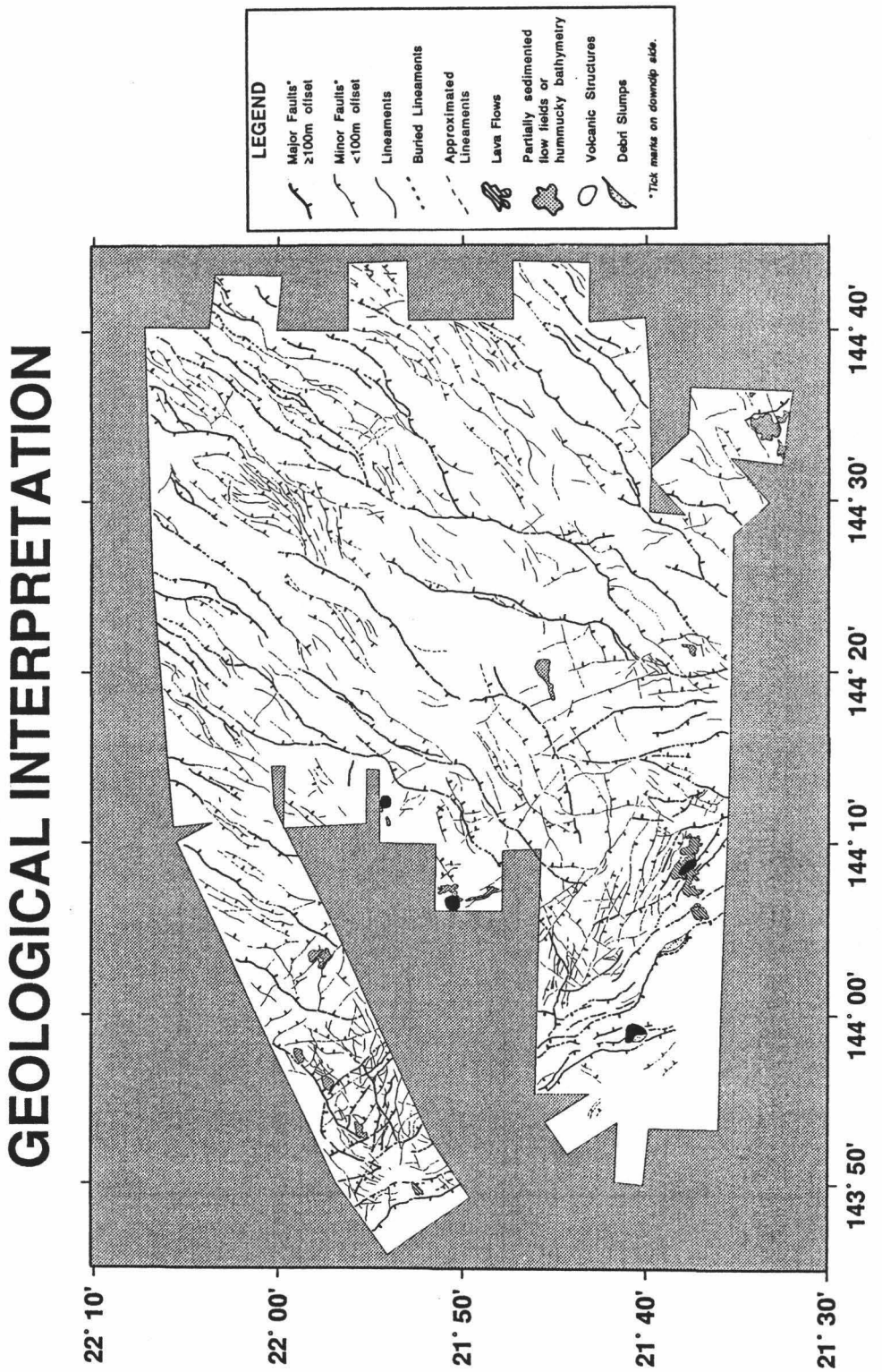

Fig. 7. Geological interpretation of the surveyed area using acoustic, bathymetric, and seismic reflection data. Tick marks are on the down dip side of the faults. Thick lines indicate major faults with offsets ≥ 100 m. Thin lines indicate lineaments, and minor faults with offsets < 100 m. Black areas represent volcanic features. Dotted areas display hummocky topography or partially sedimented lava flows. Striped regions are lava flows. Debri slumps are shown by the lightly dotted areas.

and SeaMARC II bathymetry. Dip direction was determined from both the 3.5 kHz and mixed frequency reflection records and SeaMARC II bathymetry. The resulting interpretation presents minor rift-related volcanism along the EBF and in the backarc basin and a dense distribution of normal faults with throws reaching 490 m in the forearc and a cumulative throw of 1475 m along the EBF. Note, however, that volcanism is highly variable from one rift environment to the next and can occur at any stage of rift evolution [*Rosendahl*, 1987]. The faults visible on the side-scan acoustic image correlate with those visible on the seismic reflection records. Faults with throws less than approximately 10 m (measured on the echograms) or oriented perpendicular to the track line were not detected in the side-scan image and therefore not drawn in the map view interpretation (Figure 7). Lineaments were drawn when it was not possible to measure dip direction from either the seismic reflection records or SeaMARC II bathymetry. The EBF and the forearc faults appear as two dominant trends at right angles to each other, each population displaying a sinuous, zigzag pattern with both synthetic and antithetic minor faults (Figure 7).

DATA ANALYSIS

Since fault orientation and geometry are a function of strain at the time of formation [*Ramsey*, 1967], it is essential to identify possible fault populations and their relationship to one another. The processes that create fractures and lineaments may, however, result in overprinting of fault generations, spatial variation, or a stress field reorientation over the course of fault formation. Considering such cases, I have chosen to divide the survey area into smaller regions where the stresses responsible for the deformation may be essentially constant and solve for the principal directions within each region.

Determining Fault and Lineament Trends

The survey area was divided into four zones based on fault and lineament patterns on the acoustic image, morphology on the bathymetry, and geologic structure seen in the seismic reflection records (Figure 8). Zone 1a includes the 1.5 km high EBF and a portion of the Mariana backarc basin. Its eastern boundary is defined by a break in slope along the back slope of the hanging wall of the EBF as observed on seismic reflection profiles 1 and 8 in Figure 3. The break in slope becomes somewhat obscure in profile 2, and the fracture pattern to the northeast becomes one of crisscrossing faults and lineaments on the side-scan

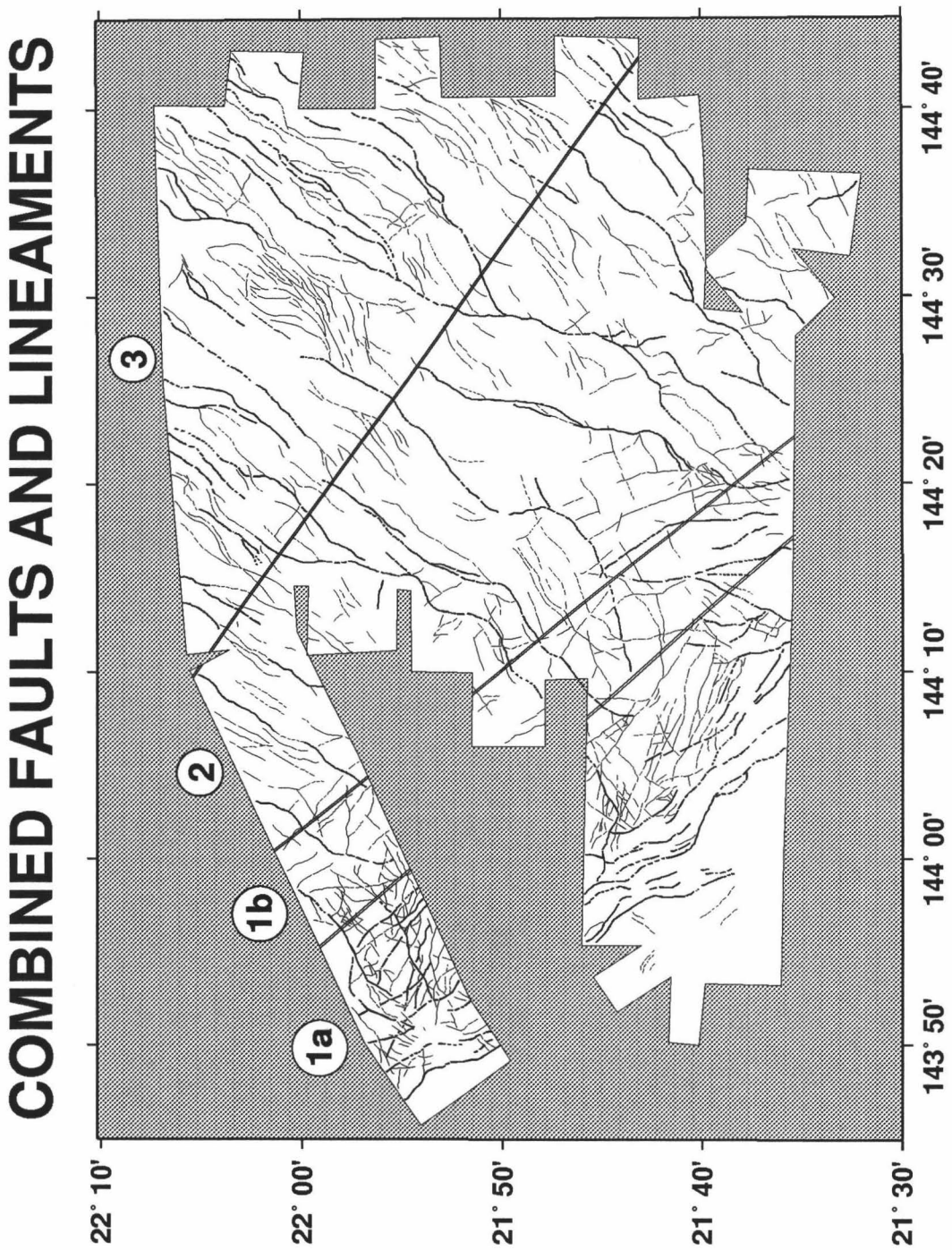

Fig. 8. Interpretation map of the survey area showing only fault and lineament traces and the four zones used in the statistical analysis. Thick lines represent major faults. Thin lines represent minor faults and lineaments.

image in Figure 5. At first glance, this region appears to be influenced by stresses along the EBF and may not be representative of the stresses acting further out on the forearc. Therefore, this narrow zone is labeled 1b; its eastern boundary being drawn where the crisscross pattern begins to die out and the large northeast trending forearc faults become dominant. Corresponding to this is another break in slope in profile 8 (Figure 3). Zone 2 is dominated by faults, with displacements greater then 100 m, bounding horst and graben features in the forearc (Figures 6 and 8). Zone 3 displays a different fracture geometry exhibited particularly well in the side-scan sonar image (Figure 5). The major faults in the forearc begin to splay in zone 3 with an increased abundance of small, subparallel, anastomosing faults.

The faults within each zone were subdivided by offset into "minor" faults with throws of less than 100 m (Figure 9), and "major" faults with throws of 100 m or greater (Figure 10). Lineaments, not identified as faults, were included with the minor faults. The choice of 100 m as the subdivision between these faults was not arbitrary. The dominant faults indicated by bathymetry and strong acoustic backscatter as the bounding faults of horst and graben structures tend to be greater than 100 m, whereas the synthetic faults and fault splays associated with these major faults commonly have throws between 30 and 90 m. The principal stress directions may become reoriented by the onset of faulting giving rise to "second-order" fractures that are oblique to the primary fault [*Hobbs et al.*, 1976]. Since any part of a fault plane may have been adjacent at one time or another to the edge of a fracture or of a slipped region, it is possible that temporary perturbation of the regional stress field may have occurred at any point and may have been responsible for certain "secondary" features. Alternatively, some "secondary" feature may have formed before the through-going fault developed [*Hobbs et al.*, 1976]. Thus, using 100 m as the criterion may enable us to separate primary from secondary fracturing and provide a clearer picture of the regional strain field.

Azimuths of the faults and lineaments were determined by digitizing points along each straight line segment of a lineament from the geologic map and calculating the distance according to the map projection and global position (a program written for this purpose is shown in Appendix B). In this way a sinuous fracture is represented by a sum length of straight segments with unique azimuths, rather than by an unweighted and visually determined average strike.

To determine multiple modes in the lineament and fault traces of each zone, I follow the method of *Wessel and Wessel* [submitted], outlined in Appendix A. First, a technique

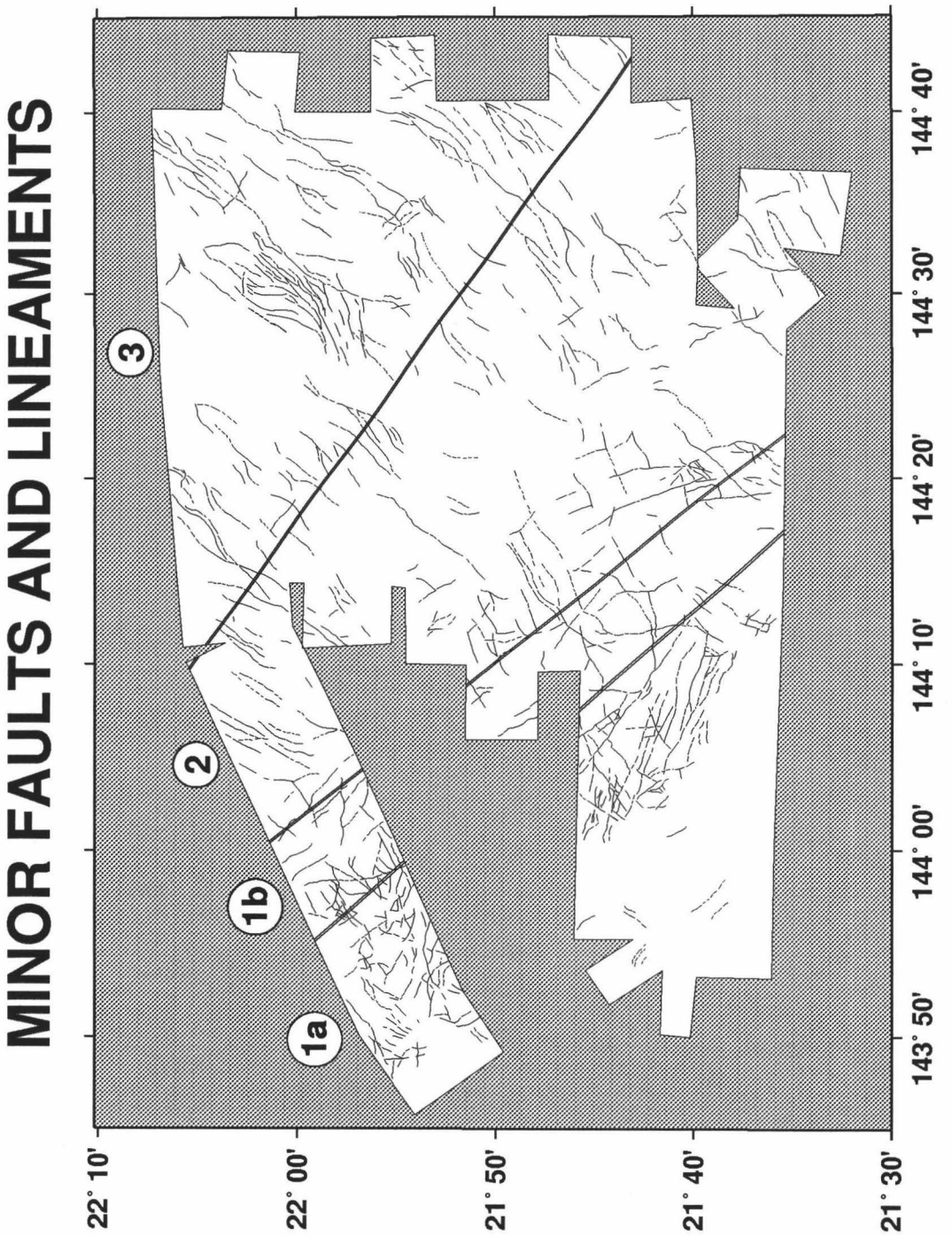

Fig. 9. Interpretation map of the survey area showing only minor fault and lineament traces and the four zones used in the statistical analysis.

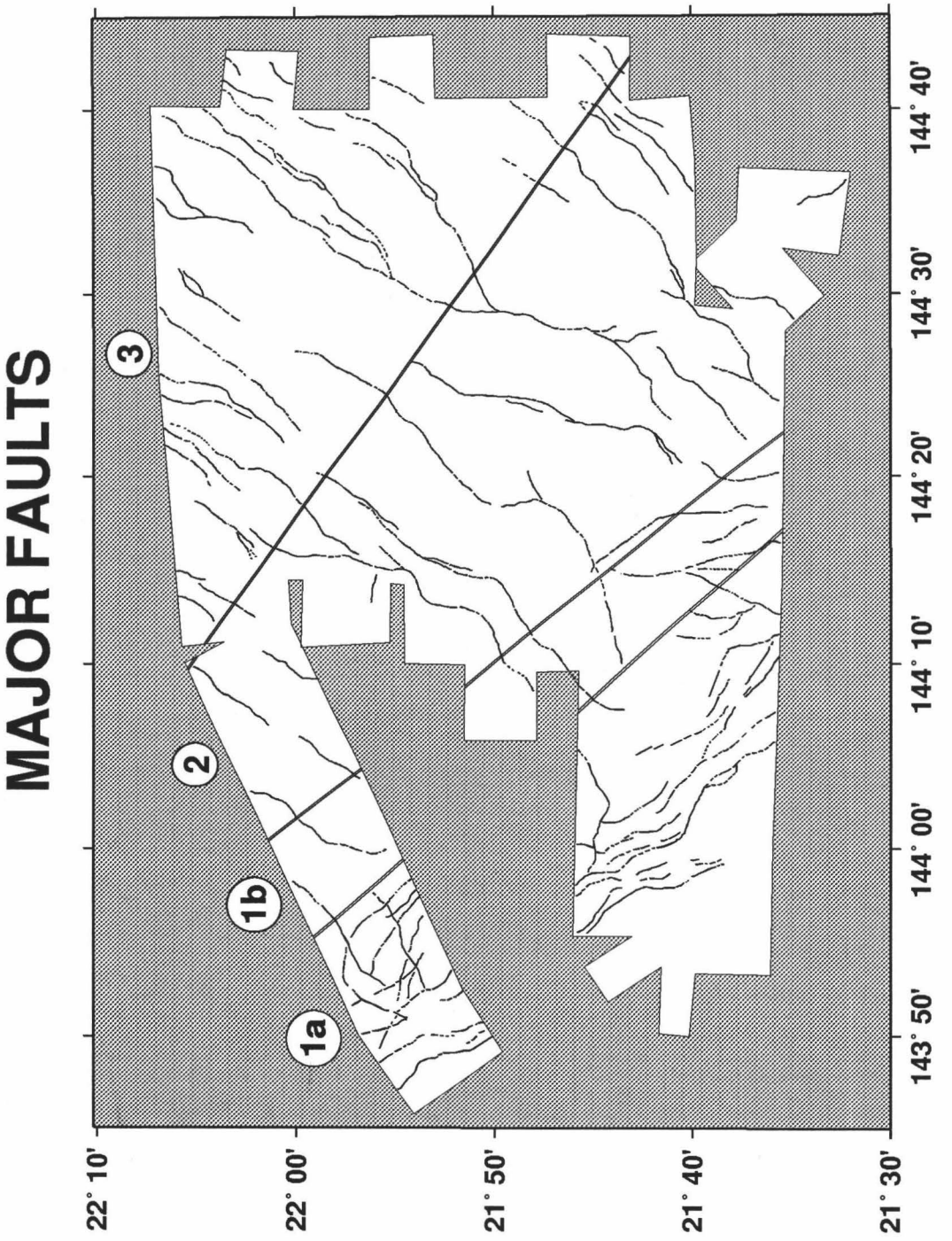

Fig. 10. Interpretation map of the survey area showing only major fault traces and the four zones used in the statistical analysis.

proposed by *Krumbein* [1939] is enlisted to take care of the mathematical difficulties inherent in oriented data that calls for the azimuth of each lineament to be doubled. A fault trace may be expressed as either of two opposite directions. The doubling of its azimuth allows us to calculate, among other statistics, the parameters of each distribution without any ambiguity. The result is that the principal orientations of the sample will be preserved regardless of the directional sense in which the lineaments were recorded. To recover the true modes, the calculated values and the associated errors are divided by 2 [*Davis*, 1986; *Krumbein*, 1939].

Estimating Errors

When measuring azimuths and lengths of linear features off the interpreted seismic reflection and SeaMARC II maps, errors in lineament location are introduced. Navigational errors, such as drift, can directly affect the placement of seafloor features on maps. In this study, it appears that any error in fracture location has most likely shifted the true location of the survey area as a unit rather than randomly altered the position of individual faults, thereby skewing their orientation with respect to one another. The small amount of mismatch of features in the SeaMARC II overlapping side-scan swaths is one indicator of this.

The most significant source of error comes from the flat bottom assumption used in the side-scan processing [*Johnson and Helferty*, 1990]. This error affects the fault azimuth as well as the length. This is an important consideration in this study, because noise has reduced the resolution of the bathymetry. Thus, determining the location of small faults and lineaments was based primarily on the side-scan sonar acoustic characteristics and correlation with the seismic reflection sections. Regional slope and variable bathymetry, however, can cause geometric error in the location and therefore the azimuth of an acoustic feature [*Johnson and Helferty*, 1990; *Reed and Hussong*, 1989]. This "layover effect" is a consequence of calculating the across-track placement of a pixel of averaged acoustic energy based on the assumption that the seafloor is flat when, in fact, the sonar beam has crossed an area of great relief. The flat bottom assumption is generally a good approximation, but it causes incorrect positioning of pixels in these occasional instances. Correction for this effect in across-track distance can be achieved by using the swath bathymetric depth, Z_b, at a pixel target point, P, then recalculating across-track distance from nadir, X_b, since the bathymetric calculation of distance from nadir and depth of target

are independent of the flat bottom assumption (see Figure 11a). A rough estimate of azimuthal error caused by the "layover effect" was achieved by calculating the slant range to target, $(SR = \sqrt{X_u^2+Z_u^2})$, then using the bathymetric depth at the target point, the correct distance is found by simple trigonometry $(X_c = \sqrt{SR^2-Z_b^2})$.

The greatest amount of distortion in angle occurs when there is a significant gradient across-track for a structure crossing the track line at a highly oblique angle. The largest discrepancy in this survey occurs along a major fault in the forearc, for which pixel location errors reach 280 m on a fault segment perpendicular to the track, and 38 m to 161 m along oblique segments (Figure 11b). At worst the error in azimuth is less than 3° for very short segments, but measured over several swaths the azimuthal error averages out to less than 0.5°. Regional slope will tend to dislocate pixels across track. This will bend the feature near the track line, but the average strike will remain approximately the same across the swath. The regional slope of the Mariana forearc in the survey area is less than 2° deepening toward the northeast corner. Such a slope creates errors in azimuth of less than 1°. The mismatch of acoustic features in overlapping swaths are much less than 200 m. This mismatch also suggests that layover errors, even in areas of variable local terrain, are minimal in this data set. Finally, the survey was conducted in a manner that minimizes geometrical errors by towing the SeaMARC II fish nearly perpendicular to 45° to major bathymetric features, reducing across-track relief. The estimated total error in azimuth for any fault or lineament in the survey area is less than 1°. In the statistical analysis, data were distributed into 5° bins, so the inherent azimuthal error is smaller than the bin size.

The location of a digitized point along a fracture was estimated to have a standard deviation σ_P of 50 m as a consequence of cumulative errors in interpreting location, distortion in drafting, and accuracy of digitizing. The error in azimuth depends on the distance between two digitized points; for most segments in this study, this error amounts to less than 5°, the bin width chosen for the data analysis (see Figure 12a). Therefore, these uncertainties in azimuth will probably not significantly affect the overall shape of the data set. The assumption can then be made that there are no systematic errors in the azimuth estimates. This makes the problem of solving for multiple modes more tractable. The error in length, however, has a maximum of $\sqrt{2}\sigma_P$ (using the standard deviation of the difference between two means). For segments with a cumulative fracture length less than $\sim 3\sigma_P$ the error in length will approach σ_P, because the fracture length between any two points defining a fault must always be positive. The total fault length for a given bin is

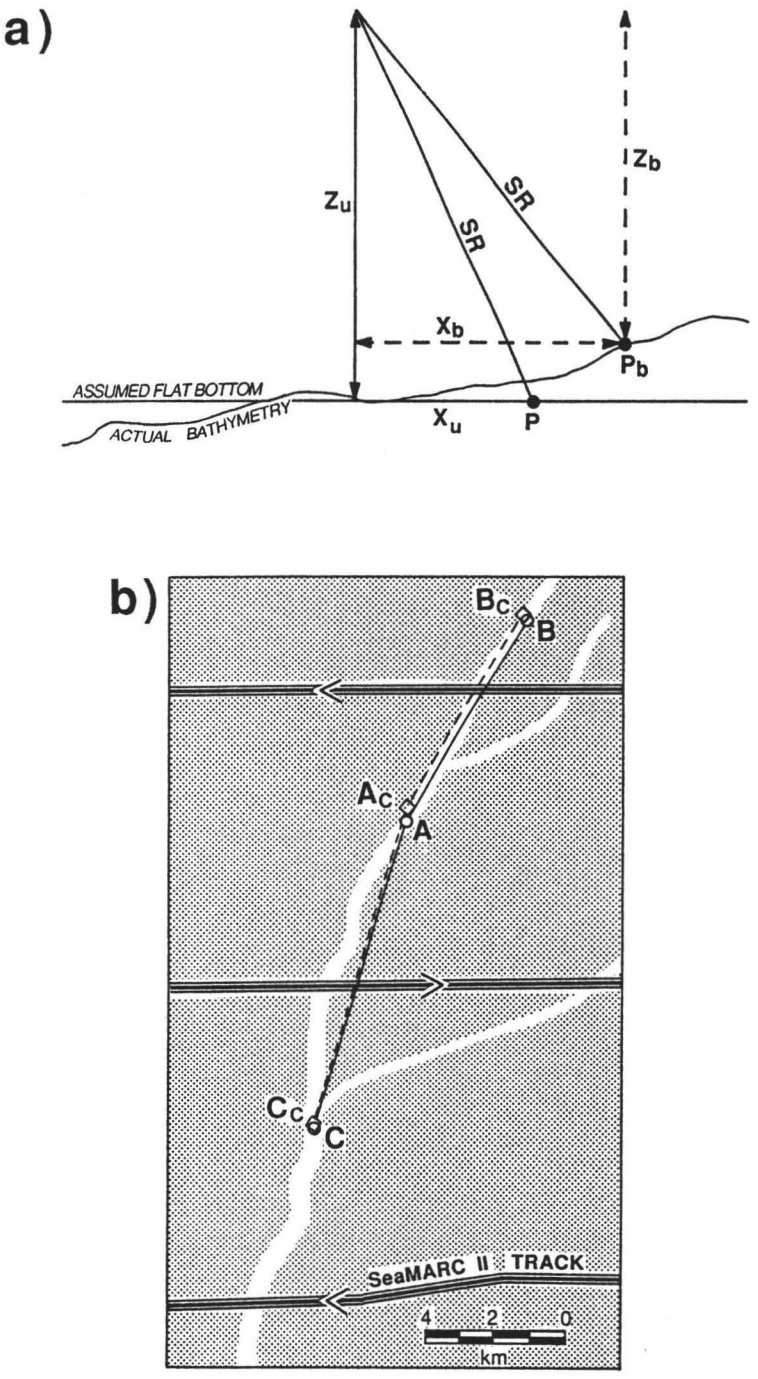

Fig. 11. a) Estimating error in azimuth resulting from the "layover effect." Pixel position is corrected by obtaining the depth, Z_b, from SeaMARC II bathymetry and 3.5 kHz data then recalculating the across-track distance, X_b. b) Schematic diagram shows the worst possible case in the survey area of error in the azimuth of a feature occurring in the side-scan sonar data as a consequence of an incorrect flat bottom assumption. A fault with 400 m relief lies obligue to the ship tracks. The circles show the original, incorrect placement of three points along solid line segments. The corrected position is shown by the diamonds and dashed corresponding segments. The discrepancy for point A is 280 m, point B is 161 m, point C is 38 m. Averaged across three swaths, the difference in azimuth is < 1°.

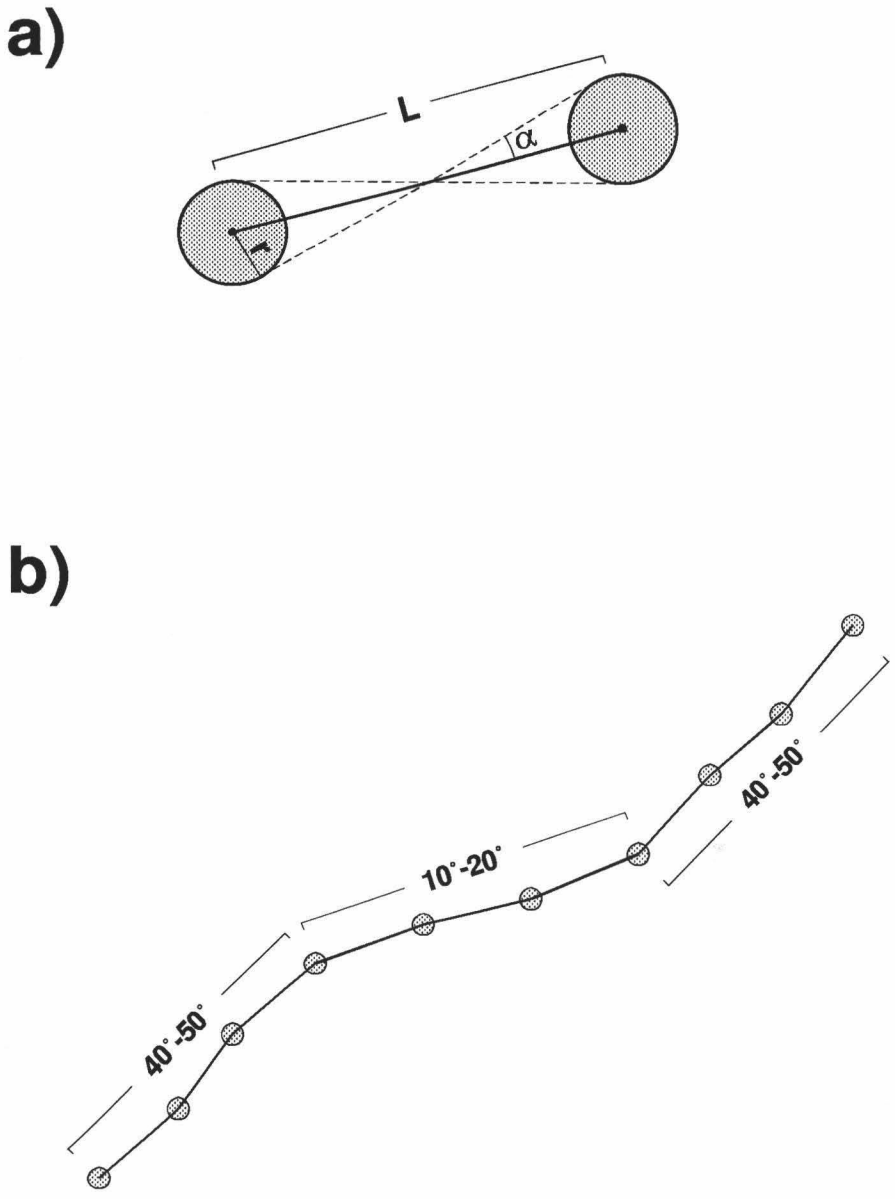

Fig. 12. a) Uncertainty ("intrinsic errors") in azimuth estimated from combined uncertainties in digitizing and point location. b) Cumulative uncertainty in bin length of multiple segments.

made up of contributions from many segments of individual faults (Figure 12b). Therefore, the error associated with each bin will depend on the number of continuous segments and the estimated error of each segment; this produces the error bars of different lengths represented in the doubled azimuth histograms (Figures 13a-d; discussed in the following section).

Solving for Multiple Modes

Assuming that the uncertainties (intrinsic errors) associated with each zone are of approximate Gaussian distribution, the method of finding trends in the azimuthal data is one of non-linear curve fitting. Each model fitted was the superposition of Gaussian functions (one function for each resolvable lineament trend), each characterized by its center position (i.e., the mode), width, and amplitude. An additional parameter representing uniform background noise was also included (see Appendix A). To choose between competing models (i.e., models with different numbers of lineament trends), the following three criteria were considered: (1) whether the model was significant at a confidence level of 95%, (2) whether the model had a reasonable goodness of fit, and (3) the degree that the residuals resembled a Gaussian distribution. The choice of a model with uniform background noise is based primarily on the Gaussian distribution of the residuals. For the case of combined data sets (major plus minor faults and lineaments in a zone), to be consistent I choose to make background noise a sum of the component sets (i.e., from the best fit models of the major and minor faults), rather than a new parameter. The danger is that this reduces the degrees of freedom, allowing more complicated models to have higher confidence levels. Most of the solutions for a single data set (zone subset), however, are not significantly different enough to cause a major discrepancy in lineament trends. A fourth criterion was added: that the sum of background noise from component data be a constant. In some cases the best model cannot satisfy all these criteria; the various dashed and dotted lines represent these next best solutions (Figures 13a-d).

The lineament data for each zone was binned into 10° (double azimuth) intervals. The preferred single and multiple mode solutions—azimuthal mode (2μ), height (h), and full width ($2w$)—are presented in Tables 1a-d and graphically illustrated by the solid curve in Figures 13a-d. The solution parameters are listed in Table 2. The true mode (μ) and associated (1σ) standard deviation are half the calculated double azimuth values—both are reported in Tables 1a-d, 2a-d, and 3a-d. For undoubled data binned in 5° sectors, the

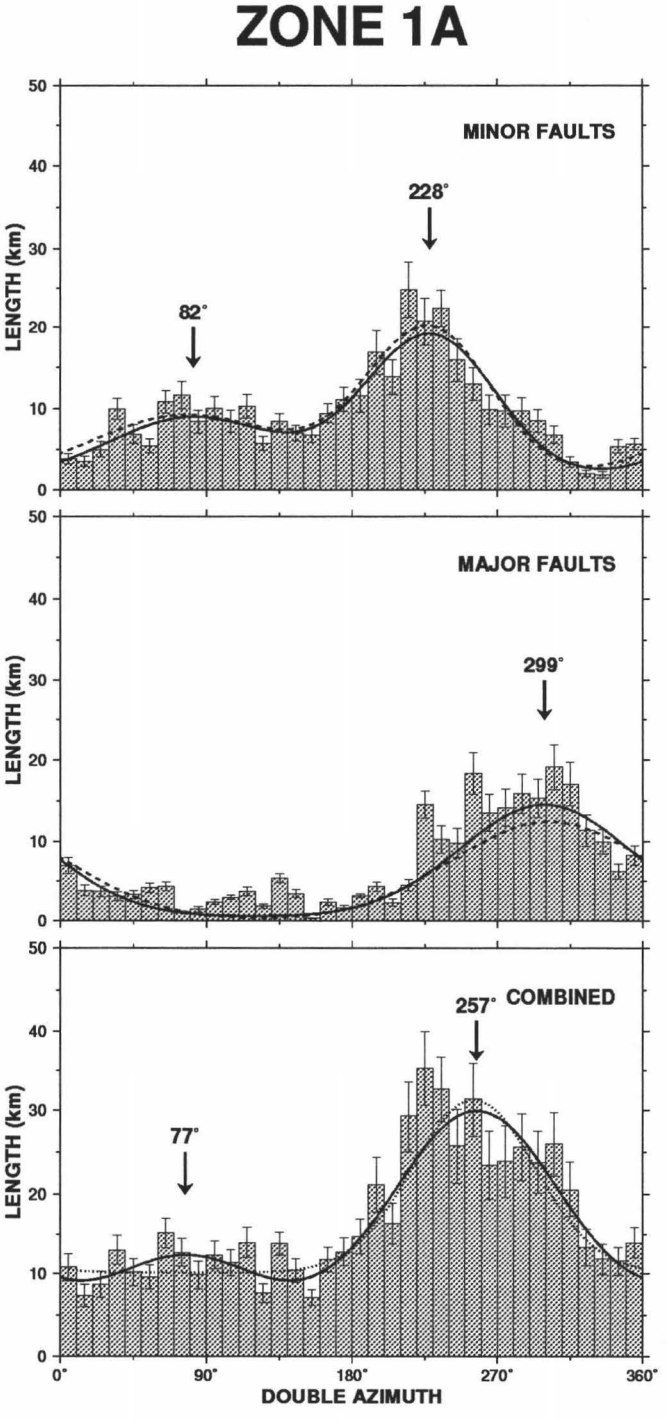

Fig. 13a. Histograms of doubled azimuth minor faults (<100 m throw) and lineaments, master faults (≥ 100 m throw), and all faults and lineaments from zone 1a, using a 10° bin width. Error bars show the error in length for each set of binned lineaments. The solid line represents the preferred solution for which the center position (mode), height, and full width are listed in Tables 1–3 and the model parameters in Tables 4–6. The arrows point to the modes of the preferred model. The criterion for choosing one solution over another is based first on whether the improvement offered by the model is significant at a confidence level of 95%, secondly on a reasonable goodness of fit, Q, and third on the Gaussian distribution of the residuals. The choice of a model with uniform background noise over a model without constant noise is based primarily on the Gaussian distribution of the residuals. In some cases not all three criteria hold. The various dashed and dotted lines represent the next best solutions.

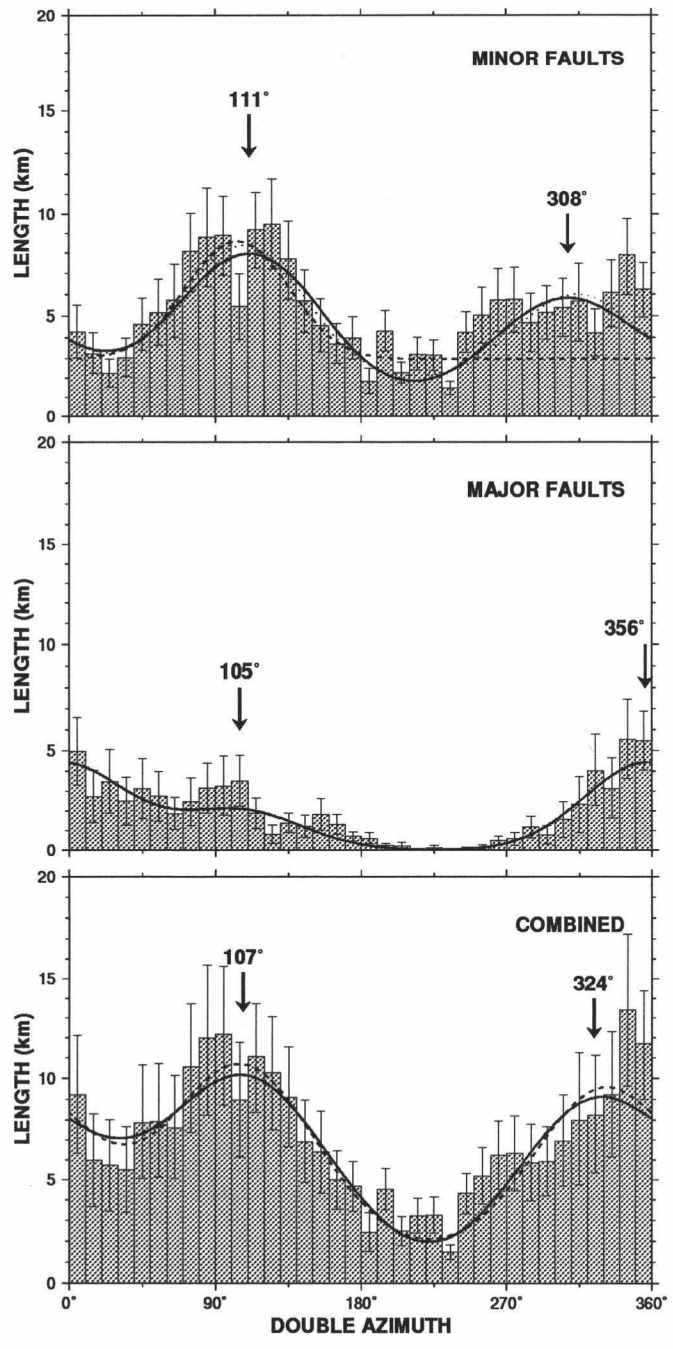

Fig. 13b. The same as in figure 13a except for zone 1b.

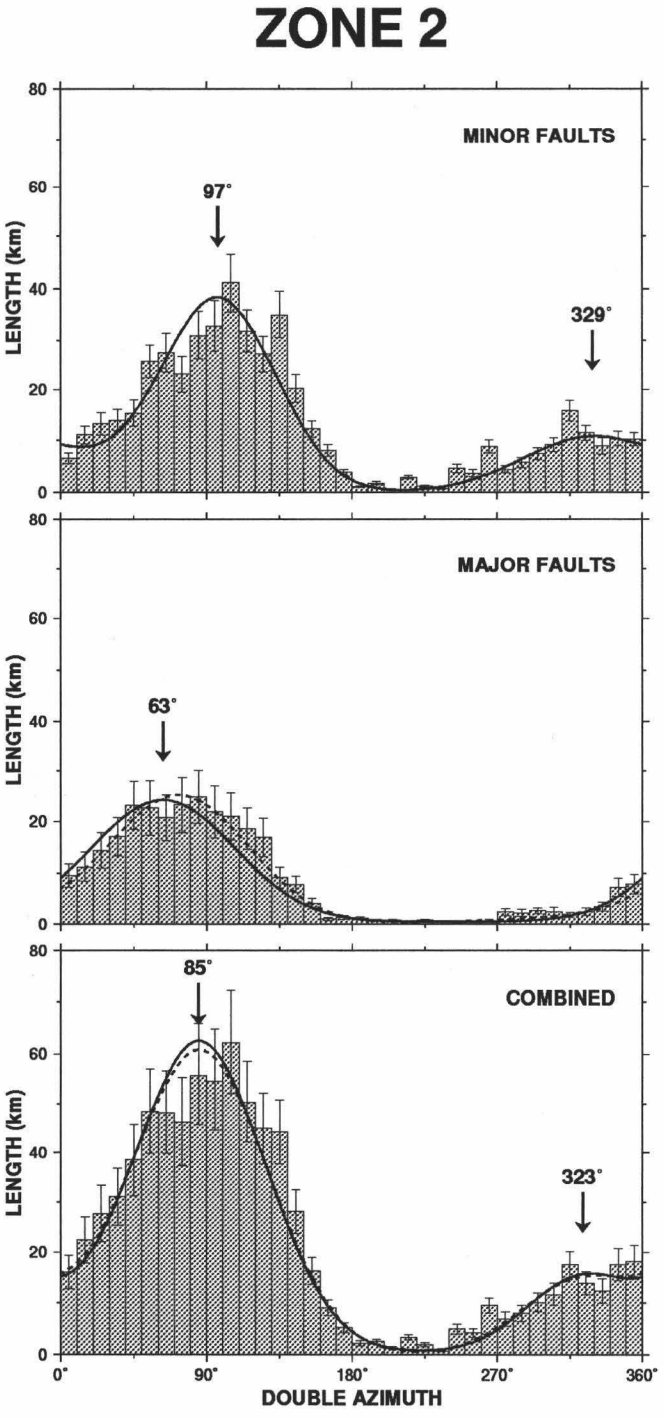

Fig. 13c. The same as in figure 13a except for zone 2.

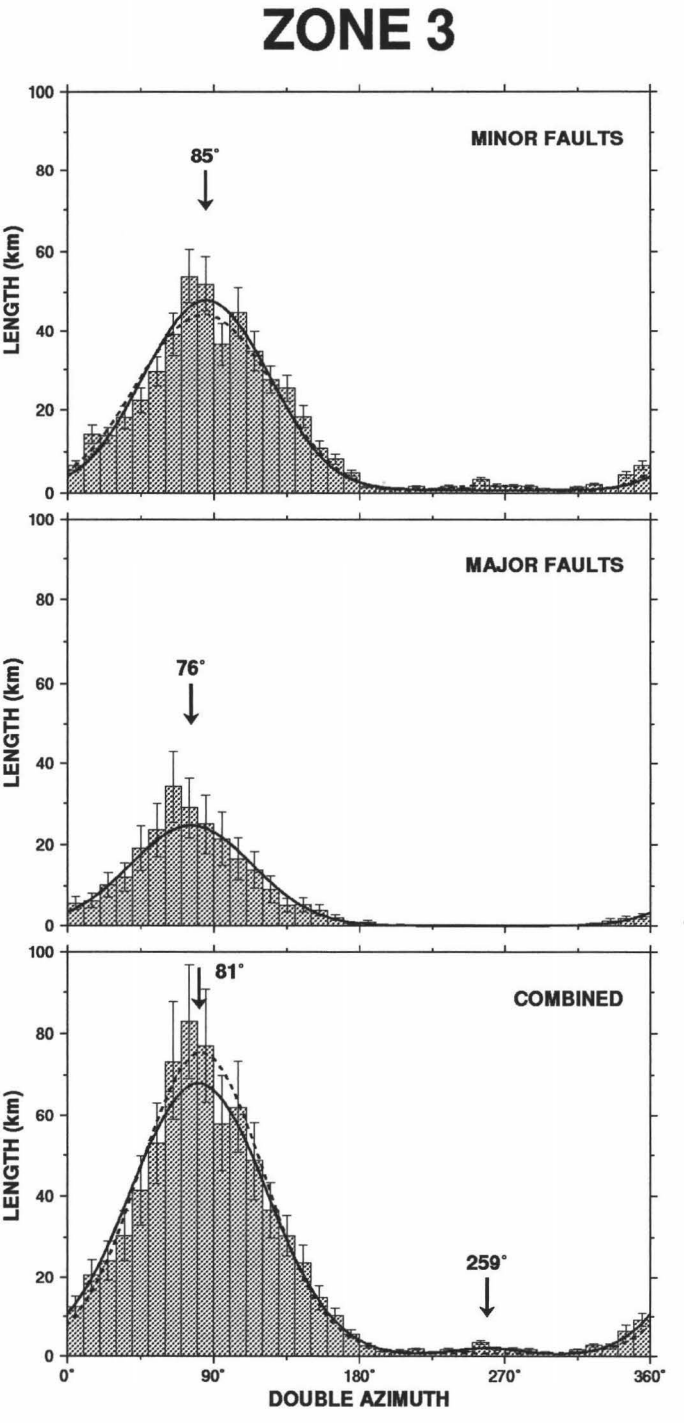

Fig. 13d. The same as in figure 13a except for zone 3.

magnitude (h) is approximately the same as the calculated height (h) of the Gaussian curve (provided the doubled angle data is grouped in 10° bins). Similarly, uniform noise approximates the calculated doubled azimuth value. Since fault traces are oriented features, opposite angles for each fracture are appended to the data sets making their orientation unbiased when displayed in a traditional rose diagram.

Calculating Strain Orientation

The development of fault geometries can be described by several strain models [e.g., *Anderson*, 1951]. Anderson's classic model on faulting was based on the Mohr-Coulomb law of rock failure which predicts a conjugate fault set should form whose intersection lies along the intermediate principal stress and strain axes on which there occurs no slip [*Anderson*, 1951]. Normal faults result when the axis of maximum extension is perpendicular to the line of strike of the conjugate sets in the horizontal plane, and the axis of shortening is vertical to the earth's surface. The resulting deformation is biaxial or plane strain (strain is accommodated along two principal axes). Conjugate faults are a special case of fault geometries predicted for triaxial strain [*Krantz*, 1988a; 1983; *Reches and Dieterich*, 1983]. Rather than a single conjugate fault set, it is much more common to find two conjugate pairs of faults arranged in orthorhombic symmetry in nature [*Freund and Merzer*, 1976]. (The term "Orthorhombic symmetry", as used here, refers to the three planes of symmetry defined by *Reches* [1983]). For the case of plane strain, this could only be possible with at least two episodes of faulting. *Oertel* [1965] demonstrated experimentally and *Reches* [1983] confirmed theoretically that this zigzag pattern is the result of a single event of triaxial strain that requires four sets of normal faults (two contemporaneous conjugate pairs) in orthorhombic symmetry. This assumes that the faults have to accommodate the applied strain field by strain along all three mutually perpendicular principal axes. A zigzag pattern results from the maximum and intermediate compressive stresses interchanging orientations during the yielding events [*Reches and Dieterich*, 1983]. These zigzag surface expressions are observed in small-scale features on the order of a few kilometers, as well as regional features, such as rift systems, encompassing hundreds of kilometers [*Reches*, 1983]. The acute angle between the two fault set trends depends on the angle of internal friction and the ratio of strains along the principal strain axes [*Reches and Dieterich*, 1983]. The axis of maximum extension, ε_3, lies in the horizontal plane, perpendicular to the acute angle bisector of the strikes of the two fault sets.

The criterion for identifying orthorhombic symmetry (without precise dip angle) is the synchronous development of fault sets having equal and opposite senses of displacement [*Hobbs et al.*, 1976; *Kelsey and Carver*, 1988]. For conjugate faults formed under plane strain, a single azimuthal trend dominates as the strikes of both fault sets are the same. If there are two conjugate sets (i.e., non-synchronous development under biaxial strain), one will overprint the other. In an orthorhombic system four sets of normal faults in two pairs, each pair having its own strike, are separated by an acute angle of less than approximately 60°, though more commonly between 20° and 40° [*Freund and Merzer*, 1976]. Each of the two strike populations must have alternate dipping faults. Rejuvenation or superimposed episodes of faulting may create a diffuse fault pattern diverging from orthorhombic or conjugate symmetries [*Kelsey and Carver*, 1988; *Krantz*, 1988a; *Reches*, 1983].

RESULTS

Preferred Models and Multiple Modes

The preferred models of fault and lineament orientation for each zone and its subdivisions (minor faults and lineaments, major faults, all faults and lineaments) are represented by the solid line in the doubled azimuth histograms in Figures 13a-d (for solution parameters see Tables 4a-d, 5a-d, 6a-d). Competing statistical models that failed to meet the criteria stated previously are shown as dashed or dotted lines (for detail see Tables 1a-d, 2a-d, 3a-d). The residuals for the preferred models show the best approximation to a Gaussian distribution amongst the competing models (Figures 14a-d). Several cases, however, display non-Gaussian residuals. I surmise that this is a ramification of the discontinuous steps in the data, and will return to this point later.

Corresponding sector diagrams of undoubled angles show the true azimuthal modes, as well as true magnitude and width of the preferred solution (Figures 15a-d). These sector diagrams are not areally correct, but are of the form most commonly presented in the literature [*Upton and Fingleton*, 1989]. Orientation is proportional to length rather than area along a wedge-shaped bin in the traditional rose (sector type) diagram. Therefore, dominant trends are visually exaggerated and minor trends become nearly invisible with proximity to the center of the diagram (Figure 16). The histograms in Figures 13a-d give the correct sense of areal proportion.

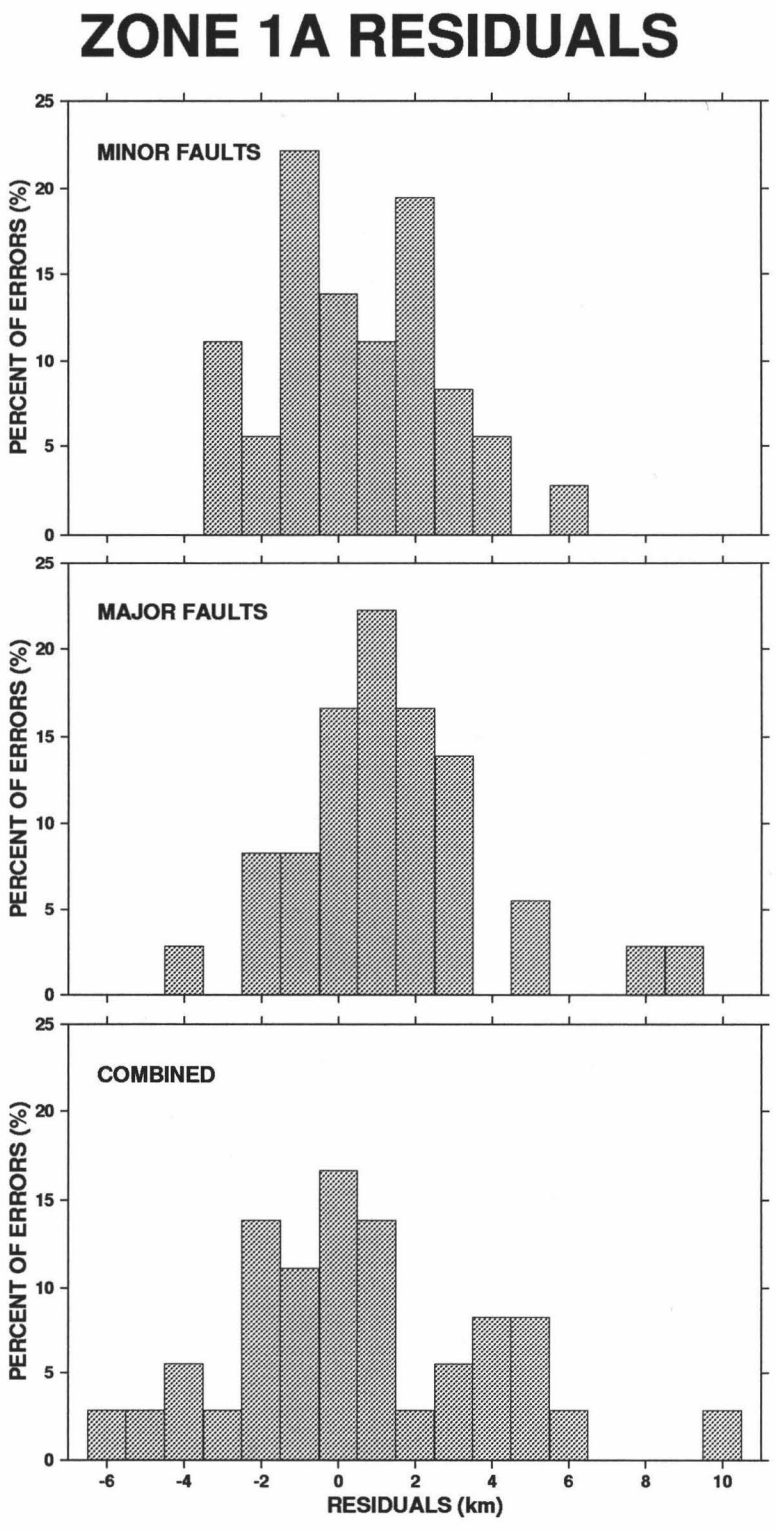

Fig. 14a. Zone 1a residuals after the solid line model has been subtracted from the corresponding data set in figure 13a. Bin width is 1 km. Note that the residual distributions for the minor faults and the combined data are not Gaussian.

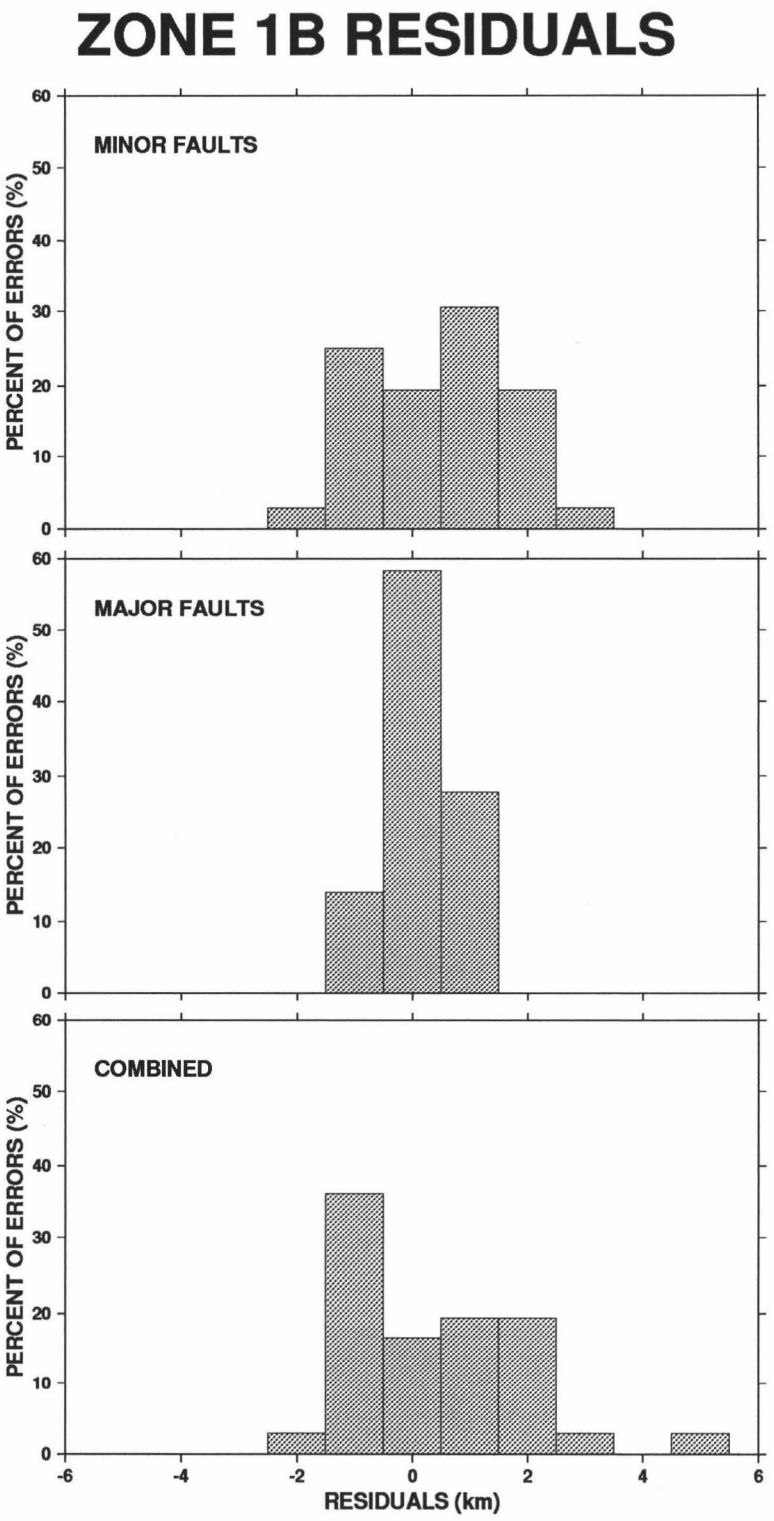

Fig. 14b. Zone 1b residuals after the solid line model has been subtracted from the corresponding data set in figure 13b. Bin width is 1 km. Again, the residual distributions for the minor faults and the combined data are not Gaussian.

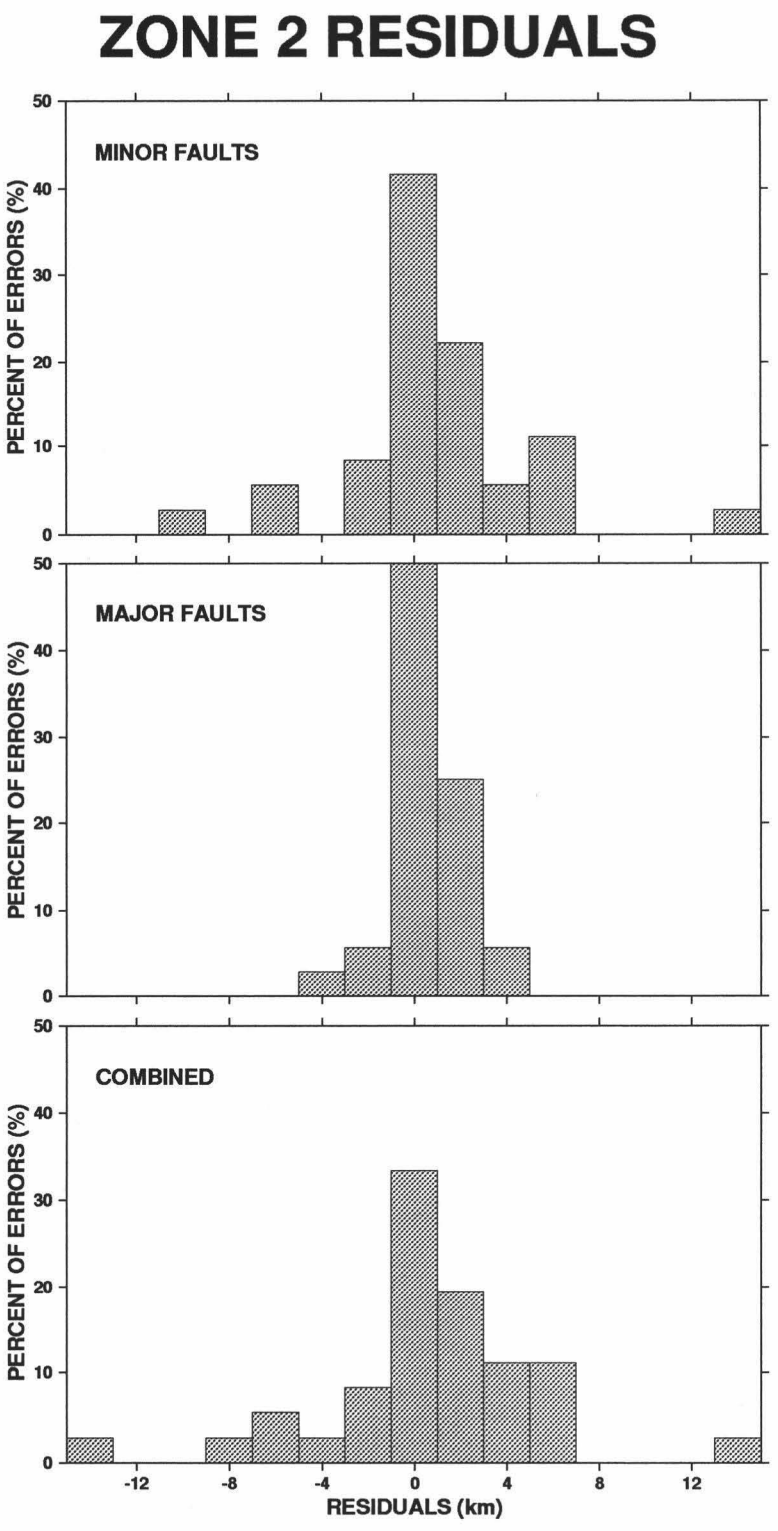

Fig. 14c. Zone 2 residuals after the solid line model has been subtracted from the corresponding data set in figure 13c. Bin width is 2 km. Here, the residual distributions for the major faults and the combined data are not Gaussian.

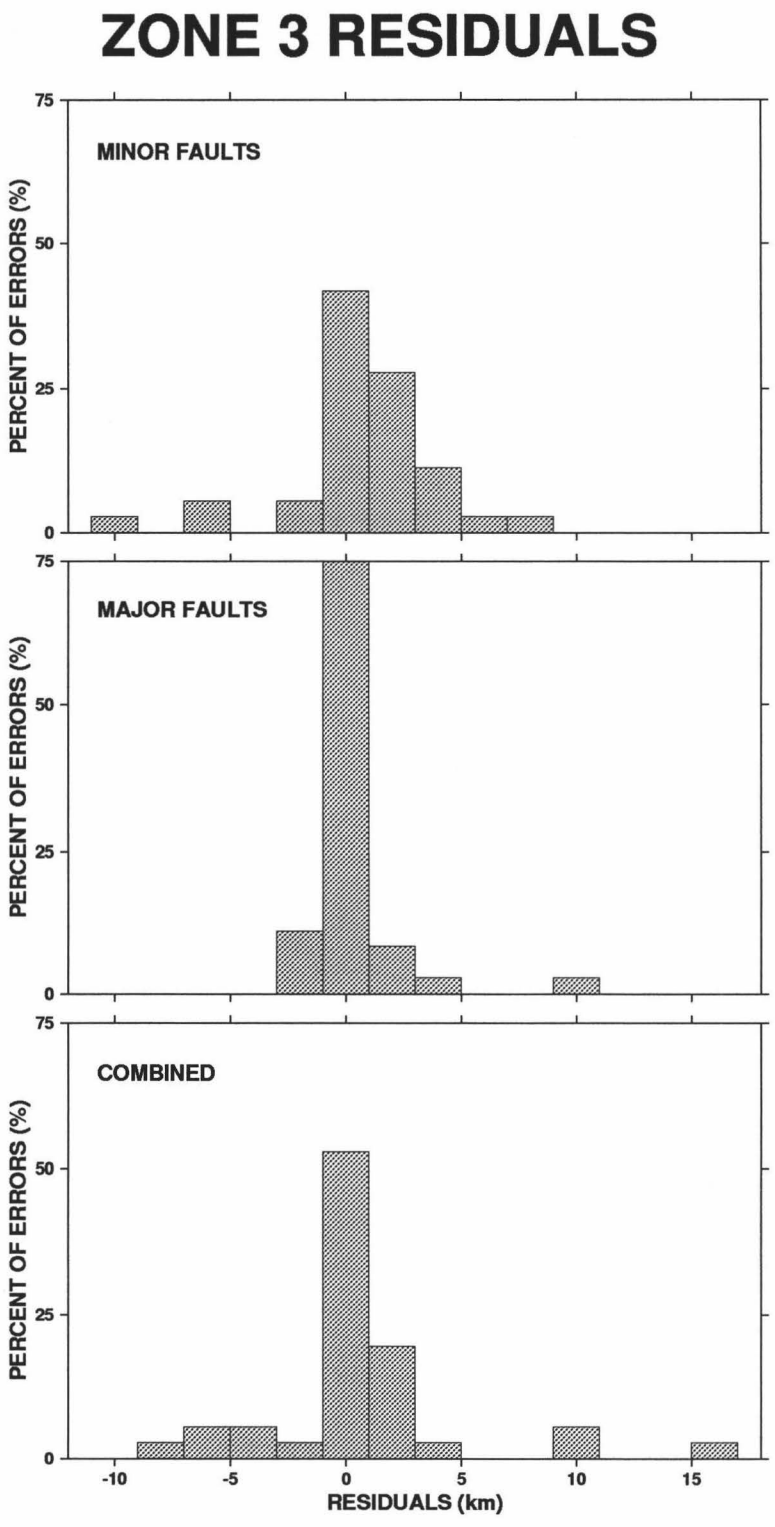

Fig. 14d. Zone 3 residuals after the solid line model has been subtracted from the corresponding data set in figure 13d. Bin width is 2 km. Note that the residual distribution for major faults are not Gaussian and not very Gaussian for both the combined and minor fault data.

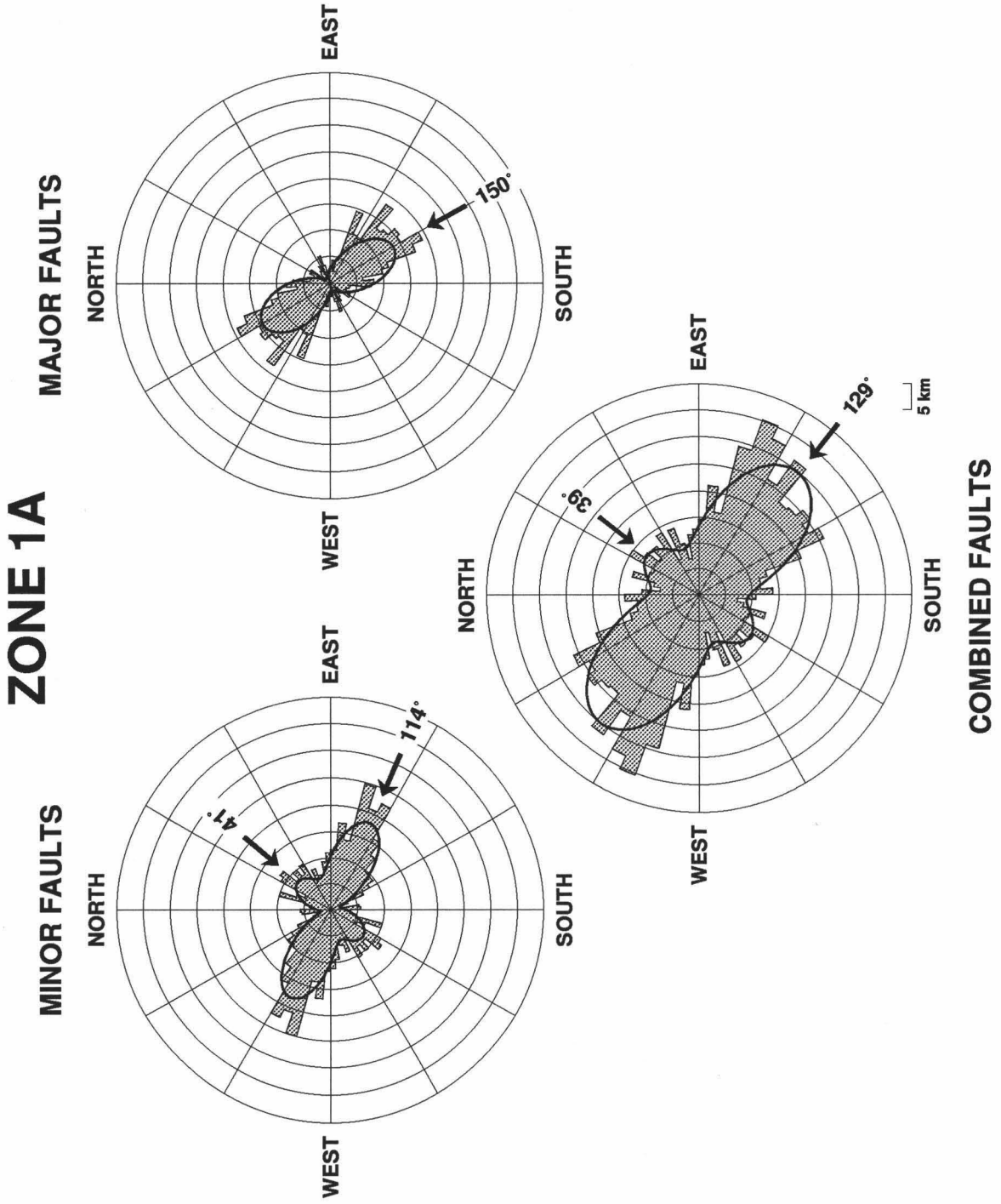

Fig. 15a. Zone 1a fault and lineament orientations for minor, master, and combined faults plotted in traditional sector (rose type) diagrams with corresponding best fit models shown in figure 13a. The arrows indicate modal directions for the models. The data has been grouped into 5° bins. The radial grid represents fracture length and is constant for each zone to visually show relative abundance. For each measured azimuth, its opposite is also plotted so as not to bias the data set, as fault traces are orientated features.

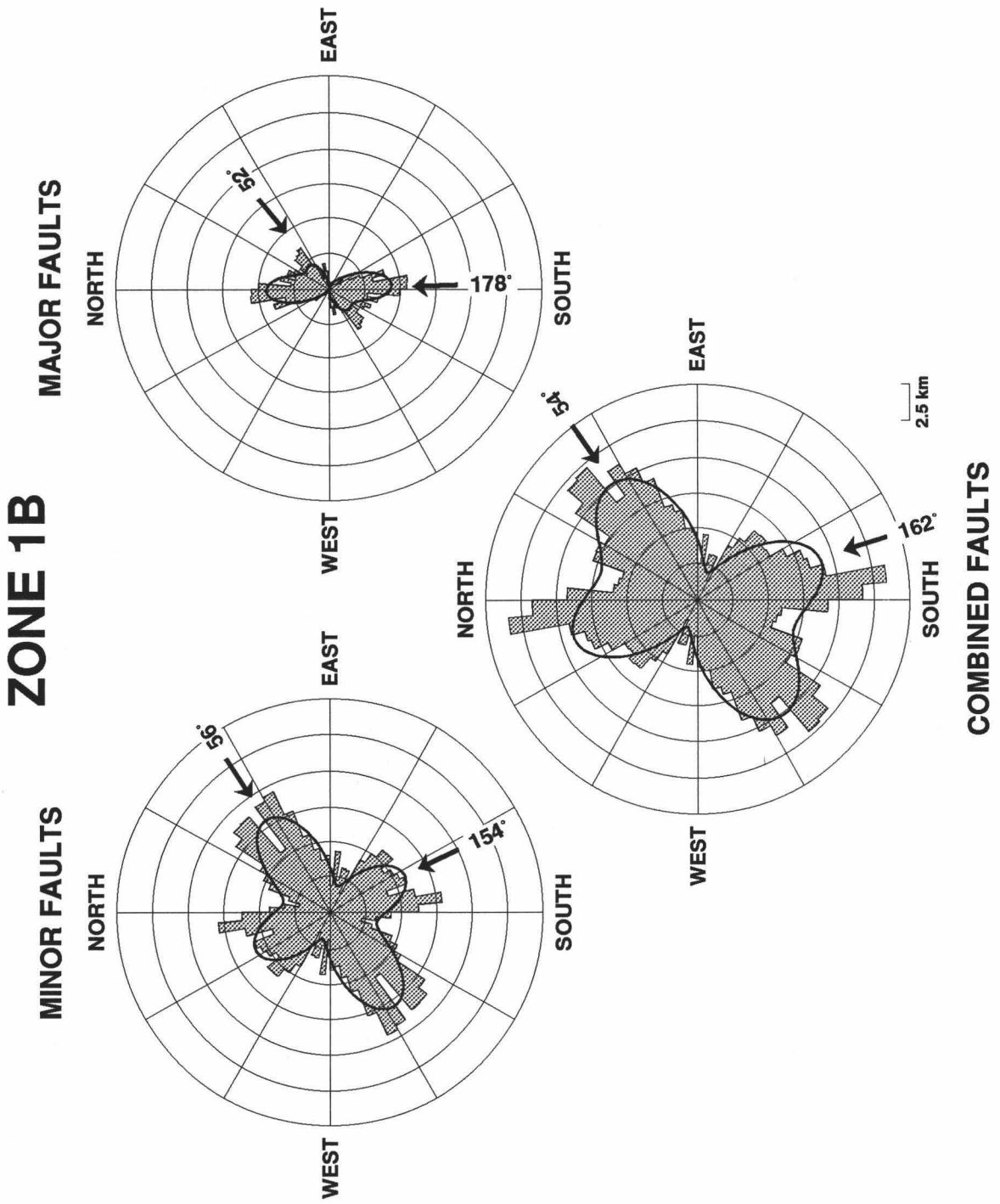

Fig. 15b. The same as figure 15a, except for zone 1b.

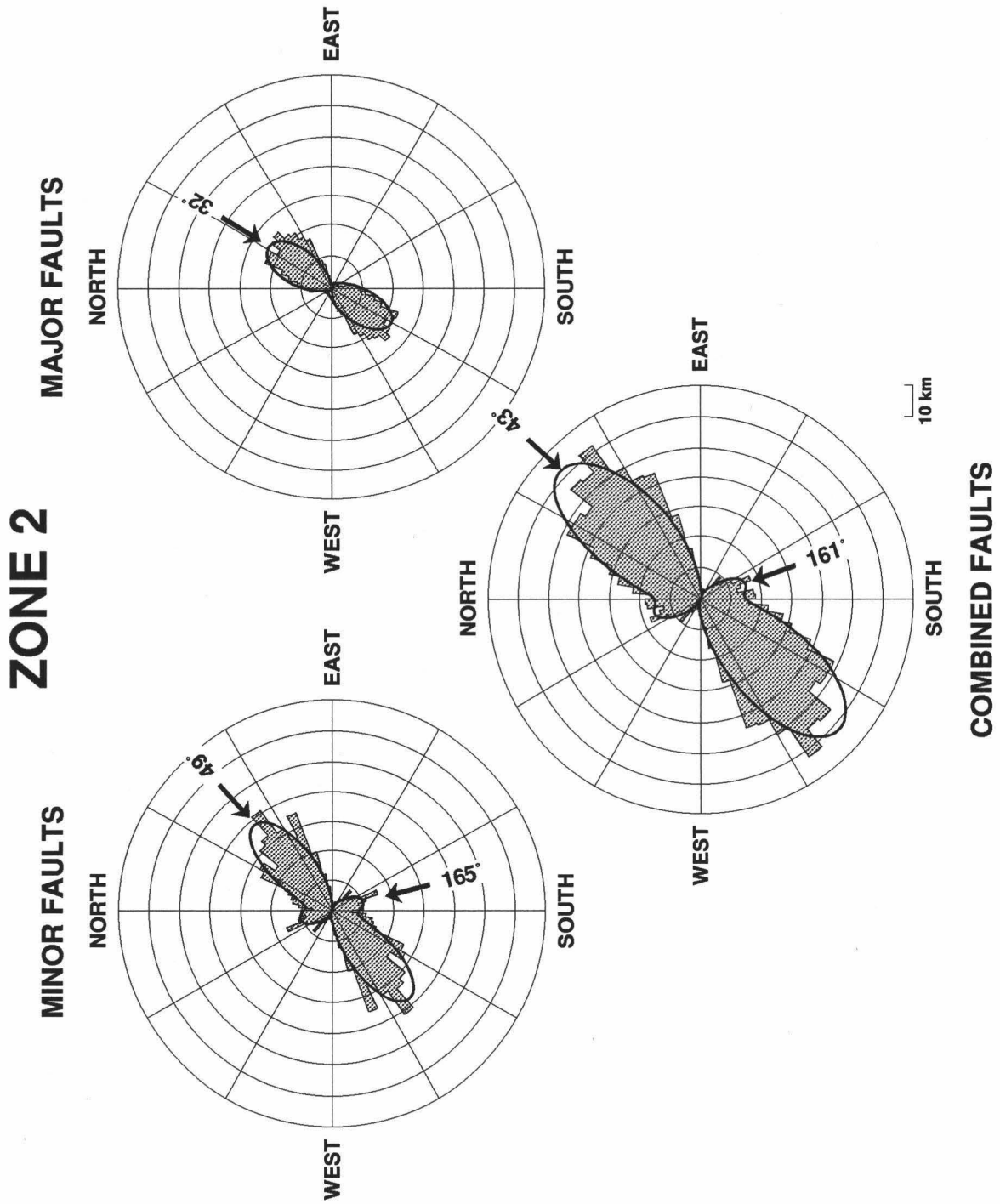

Fig. 15c. The same as figure 15a, except for zone 2.

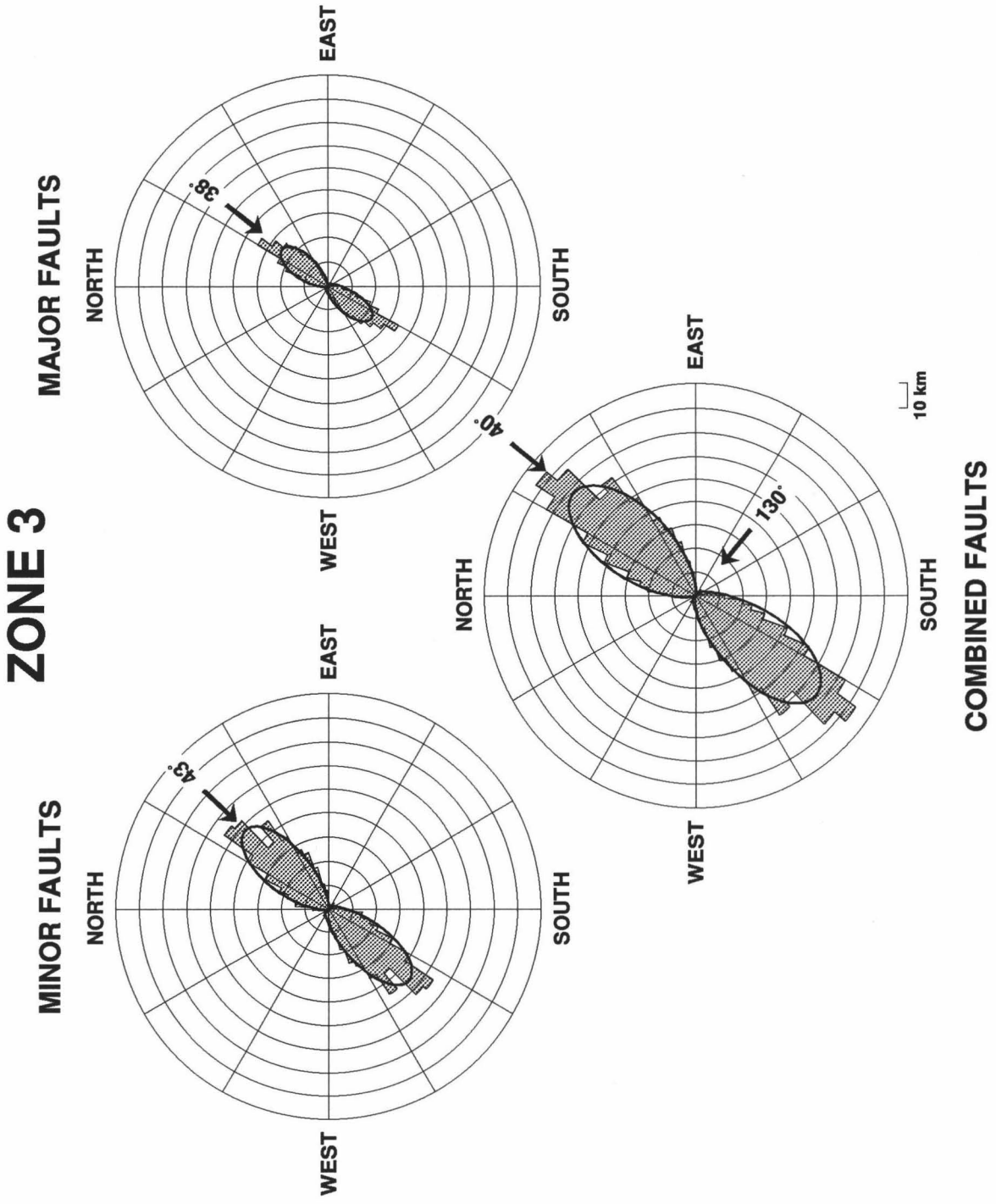

Fig. 15d. The same as figure 15a, except for zone 3.

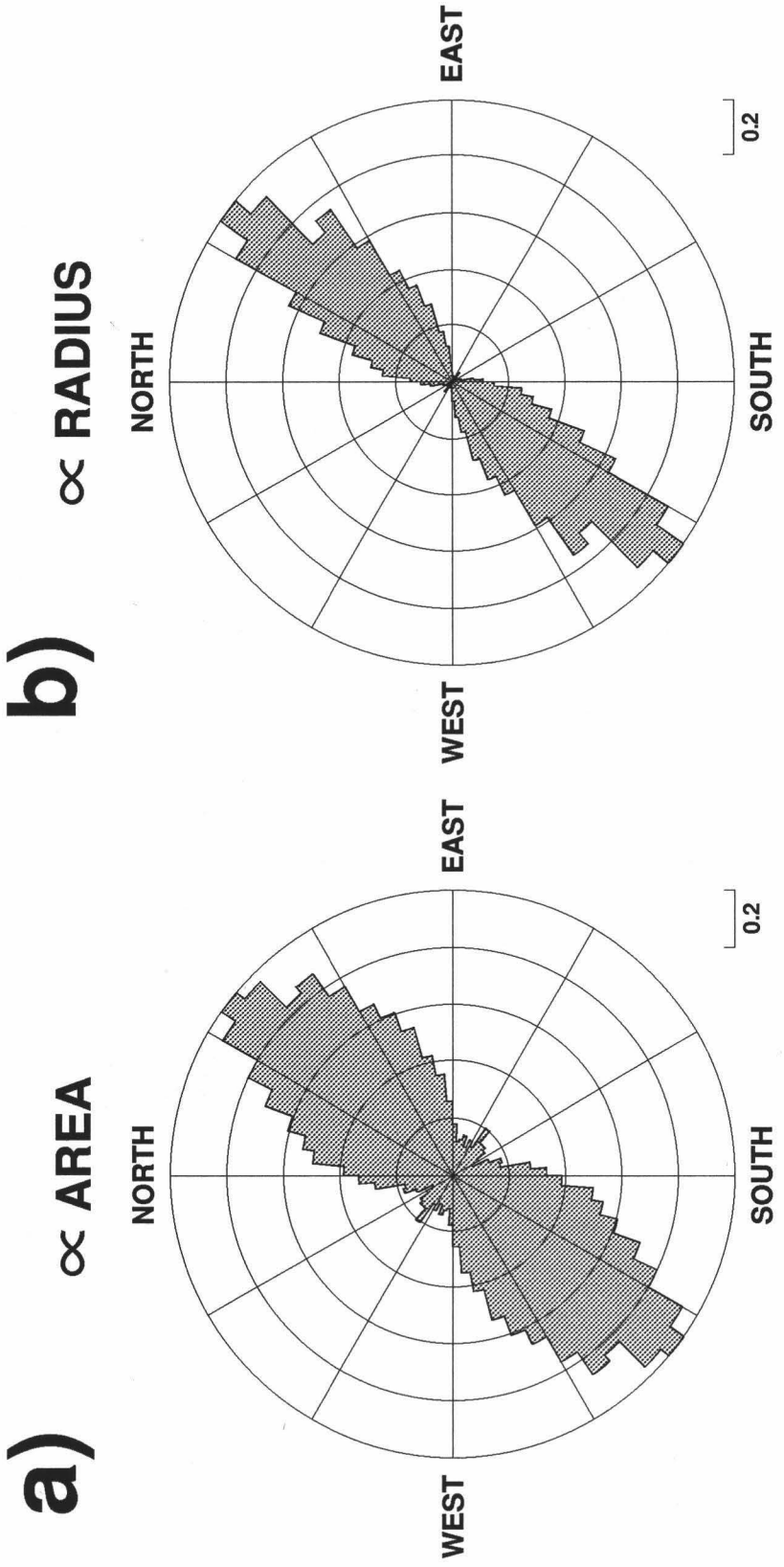

Fig. 16. a) Areally correct sector diagram, i.e., area of sector is proportional to length. b) Standard (traditional rose-type) sector diagram, i.e., radius of sector is proportional to length.

The results of this analysis show that two dominant, yet spatially separate trends exist—one associated with the EBF in zone 1a, the other in the forearc (zones 2 and 3). I will refer to the preferred principal direction for combined faults and lineaments in zone 1a as the "principal EB mode" and the preferred principal direction for combined faults and lineaments in zones 2 and 3 as the "principal forearc (FA) mode." The values for these modes will be given in the proceeding discussion (for a summary see Table 7).

Zone 1a, dominated by the EBF, has a mode of 129°±1° for combined faults and lineaments (Figure 15a; Table 4a). This is the trend of the principal EB mode. The major faults in this zone account for most of the offset along the face of this 1.5 km scarp and have a single mode of 150°. The major faults of the forearc that cross into the eastern half of zone 1a (see Figure 10) do not comprise a statistically significant population in comparison with the major faults comprising the EBF in this region. Nevertheless, the interference of these two opposing sets of major faults has created large fault bounded blocks in both zones 1a and 1b. Although data coverage is sparser in these zones, it appears that the fault sets are contemporaneous because their cross-cutting relationships show no preference.

It becomes clear from the histograms and sector diagrams (Figures 13a-d and 15a-d) that zone 1b is significantly different from the other zones; exhibiting much broader trends of an orientation that appears rotated or distorted from both principal EB and forearc modes. For major faults, the slightly more dominant mode of zone 1b (Figure 15b) trends nearly north-south and is approximately the bisector of the acute angle between the dominant mode of the major faults in zone 1a and zones 2 and 3. The preferred models for subdivisions and the combined fault data show bimodal distribution nearly equal in magnitude (Figure 15b). The northerly trend for the combined faults is 162°±7°. I will refer to this as the EB-interference mode. The northeasterly mode in the combined fault data is 54°±6°, which I will refer to as the forearc-interference mode.

Figures 15c and 15d show the dominant modes of the combined faults and lineaments in zones 2 and 3 to be 43°±1° and 40°±1°, respectively. These two modes are thus statistically different, though the difference is quite small. The minor and major faults show more variation between their dominant modes—as much as 7° and as little as 4°. This small difference is indicative of a minor change in fault orientation, that in turn can be attributed mostly to the assignment of spatial zones. Closer inspection of the minor faults in zone 2 (Figure 9) reveals that fault orientation changes near the southern half of the 1b-2 zone boundary. In fact, a minor, secondary trend at 161° in the minor faults of zone 2 is

the same mode, within one standard deviation, as found in the combined faults of zone 1b (Figure 15). Therefore, the majority of faults and lineaments in zone 2 have the same trend as in zone 3, except in areas near the 1b boundary where the minor faults appear to be relieving some of the stresses felt in zone 1b. This has altered the overall azimuthal distribution resulting in a slightly different modal solution than for zone 3. In general, zones 2 and 3 are representative of the fault distribution in the Mariana forearc at 22° N, and the principal forearc mode, taken to be the average between the dominant modes of the combined faults in zones 2 and 3, is then 42°±1°.

The combined faults and lineaments in zone 3 display a very minor mode at 130° (Figures 13d and 15d) comprised of high angle, antithetic minor faults. Its significance in the statistical model results from decreased noise level with increased sample size. This is the same trend as the principal EB mode found in zone 1a. Whether the relationship is purely incidental or not is unclear.

Data Distribution and Fault Patterns

The method used in the previous section to determine multiple modes in circular data (Appendix A) assumes that faults and lineaments can be characterized by one or several discrete directions, each associated with normally distributed errors. The observed distribution of data in the double azimuth histograms (Figures 13a-d), however, proves to be more complicated. As noted previously, several of the residuals are not of Gaussian distribution. In general, the observed distribution of data in the histograms can be characterized by two different shapes. Both minor and major faults display a broadly distributed Gaussian mode with a 10° wide local minimum near the central peak (e.g., Figure 13c, major faults). Some degree of "blockiness" or discontinuous steps may also be associated with this type of distribution peak. The second type of distribution is characterized by asymmetry and discontinuous steps occurring in the lower amplitude trends (e.g., Figure 13b, major faults).

These nuances in distribution shape can graphically be illustrated by the convolution of a preferred mode with an "Earth filter" (normally distributed random noise) to produce a probability distribution (Figure 17). In the simplest case, one generation of faulting produces linear traces in a single preferred direction. This fault geometry would display precisely the Gaussian distribution assumed by the curve fitting technique used. The 3-D orthorhombic symmetry described by *Reches and J. H. Dieterich* [1983] gives rise to the

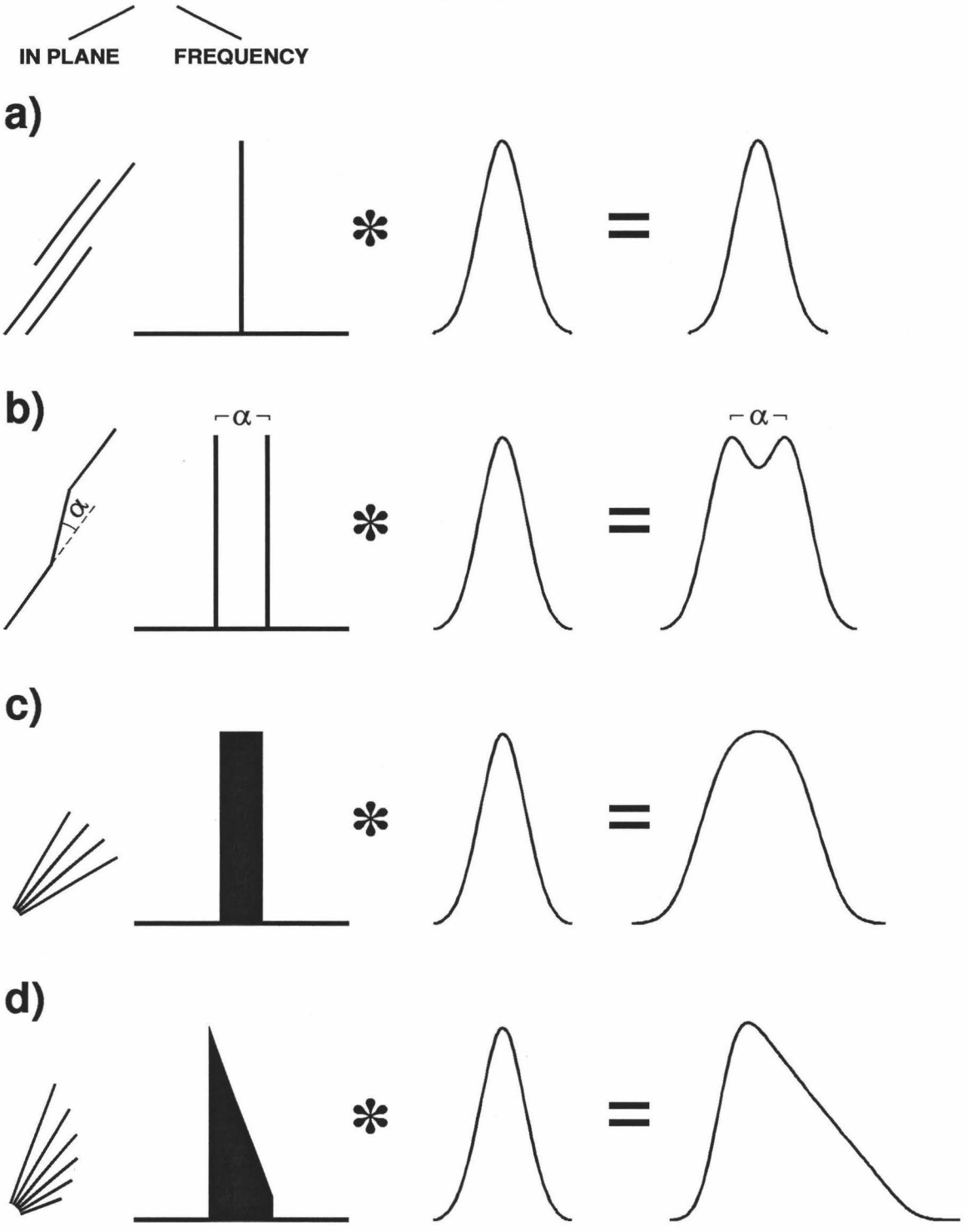

Fig. 17. Schematic convolution diagram for nuances in observed data distributions resulting from various fault patterns. These distributions may be unresolvable using the curve-fitting method employed.

zigzag surface expression commonly found in rift environments [*Lowell*, 1985]. Two end-member distributions can occur depending on the sharpness of the fault bend comprising a zigzag fault trace. An angular zigzag pattern would give rise to two discrete azimuthal modes separated by the acute angle, α, between the fault sets. Convolution with an "Earth filter" would generate two Gaussian curves separated by α. For a small α the curves would closely overlap resulting in a broad distribution with a local minimum in the center (Figure 17b). Resolution of the local minimum depends on the width of the noise filter and the angle α between the two modes. Usually α is not large, between 20°-40°, in sinuous or zigzag rift faults [*Freund and Merzer*, 1976]. A discontinuous fault pattern, possibly a consequence of overprinting or an abrupt reorientation of the stress regime, could also produce the same distribution. If the bend in the zigzag is smooth (i.e., a sinuous fracture), then the function between the two main modes is continuous, approaching a "box car" shape in the extreme case. This produces the flat topped, broad curve in Figure 17c. Width of the curve and flatness of the top likewise depend on the width of the "Earth filter" and the angle α between the two modes. A continuous change in fault orientation could also produce this shape of curve. Variations and rotations in the stress field, either time or spatially dependent, could generate discrete modes of variable amplitude. The probability distribution from the convolution would be asymmetric (Figure 17d).

Whereas the non-linear curve fitting technique may not be able to resolve the subtleties in data distribution shape that may cause non-Gaussian residuals, this simple convolution gives us insight into the type of fault geometries that might create such observed distributions. However deconvolution of the data might be feasible, without the constraint of *a priori* geologic knowledge, it would be very tempting to over-interpret such distributions. The above convolution scheme may provide an explanation for the two differently shaped distributions observed in the histogram data and for the resulting non-Gaussian residuals. The large error bars, in comparison to such subtleties as the local minimum, however, prohibit us from going beyond speculation.

The major faults of zones 1a and 2, the minor faults of zones 3 and some in 2 exhibit a sinuous, zigzag surface geometry (Figure 8) that correlates with a local minimum near the central peak of their dominant modes (Figures 13a, 13c, and 13d). This local minimum may result from two overlapping modes, roughly 10° to 20° apart, each representing one of the two trends of the zigzag set. There is a hint of a local minimum in the mode from zone 1a major fault data. Resolution of a local minimum can be affected by a number of factors: the sample size may be too small or there may exist a minor orientation shift from the south

to the north, blurring the two trends of the zigzag together. In fact, the mode is flat topped—a possible indicator of continuous fluctuation in orientation. Zone 1b minor faults and lineament data (Figure 13b) are comprised of short segments that are either curved or, more commonly, linear. They lack the length to have much sinuosity. Therefore the local minimum observed in the 1b data might represent two overlapping linear trends approximately 15° apart and subparallel to the forearc minor fault trend.

The character of zones 1a and 1b differs slightly from that of zones 2 and 3. The minor faults and lineaments show a large amount of uniform background noise with a greater frequency of discontinuous steps (compare Figures 13a and 13b with 13c and 13d). The interference of the forearc trending major faults with the nearly perpendicular EB major faults creates large fault blocks in zones 1a and 1b within which the minor faults occur in a wide array of azimuths oblique to the major faults (Figure 8). I speculate that these minor faults (comprising much of the background noise in the histogram data) represent the alleviation of small stresses within the rigid fault blocks caused by movement along the major bounding faults.

Figure 17c suggests that a continuous change in orientation, either spatially or through time, generates a flat-topped, broad distribution. Such distributions are common in the modes of data from the "interference region". The "interference region" includes zone 1b and portions of zones 1a and 2 that border zone 1b. The asymmetry of the distribution suggests that the change in fault azimuth is variable. Lack of evidence for strike-slip motion and compression, evidence for contemporaneous fault development, and lack of deformation in the sediments between the faults, indicates that the faults formed in place. They have not since been rotated nor distorted. I thus propose that the orientational change, suggested by the broad distributions, is spatial and not time-dependent as might be caused by a rotating stress field.

3-D Fault Geometry

I conclude that the three-dimensional geometry of the major and the larger minor faults in all zones display othorhombic symmetry (Figures 4a and 7). The two trends of the zig-zaging faults each have opposing dips, and as discussed previously, fault development along these sinuous faults appears to be synchronous and equally favored in both directions. Though unresolvable as separate modes, as a consequence of the noise level, each of the two subtle azimuthal trends show up as a single broad distribution with a local

minimum near the peak. Zone 3 major faults have a higher frequency, lower amplitude sinuosity or small angle, α, between the zigzag trends (Figure 10) causing a narrower and sharper observed distribution (Figure 13d).

Principal Strain Directions

Normal faults are generally oriented perpendicular to the direction of maximum extension [*Anderson*, 1951; *Hobbs et al.*, 1976]. In the case of orthorhombic symmetry, the direction of maximum extension, ε_3, lies perpendicular to the bisector of the acute angle between the two fault trends comprising the zigzag surface pattern [*Reches and Dieterich*, 1983]. Since the models could not resolve the two trends of the orthorhombic system, the mode of the dominant, double-peaked trend approximates the bisector and its normal is taken to be the principal axis of maximum extension. Table 7 lists the resulting orientations of the extensional principal strain axes for each mode.

The maximum difference between dominant modes of major faults versus combined faults is 20° which is observed in zone 1a. The difference in other zones is much less. *Reches and Dieterich*'s slip model [1983] is relevant only for faults displaying orthorhombic symmetry. Often small faults do not display such symmetry, but are related to the major faults in that they relieve the small stresses imposed by movement along the larger faults. In this study the choice of 100 m division between faults was based on the large structural features in the forearc, although many of the faults with 80-90 m throws display orthorhombic symmetry. Thus, I will use the combined faults in each of the four zones for determining the average strain.

Before any conclusions about the strain field can be reached, we must first consider possible deviations in the direction of maximum extension. There is little information to constrain the principal forearc extension direction in zones 2 and 3, other than the standard deviation in the mode that is less than 3°. Better constraint of the principal EB extension direction can be reached by considering the regional structure of the EBF. On a gross scale it is arcuate (Figure 1). Closer inspection of the northern portion of the Mariana island arc using detailed SeaMARC II data and SASS bathymetry [*Smoot*, 1988] reveals zigzag fault traces of both bounding faults to the backarc basin (Figure 18). Though much of the detailed geometry of the EBF is obscured by large arc volcanoes built on top of this rift flank uplift, portions of a zigzag geometry can be identified for about 100 km along both east and west boundary faults near 22° N (Figure 18a-c). The implication is that the

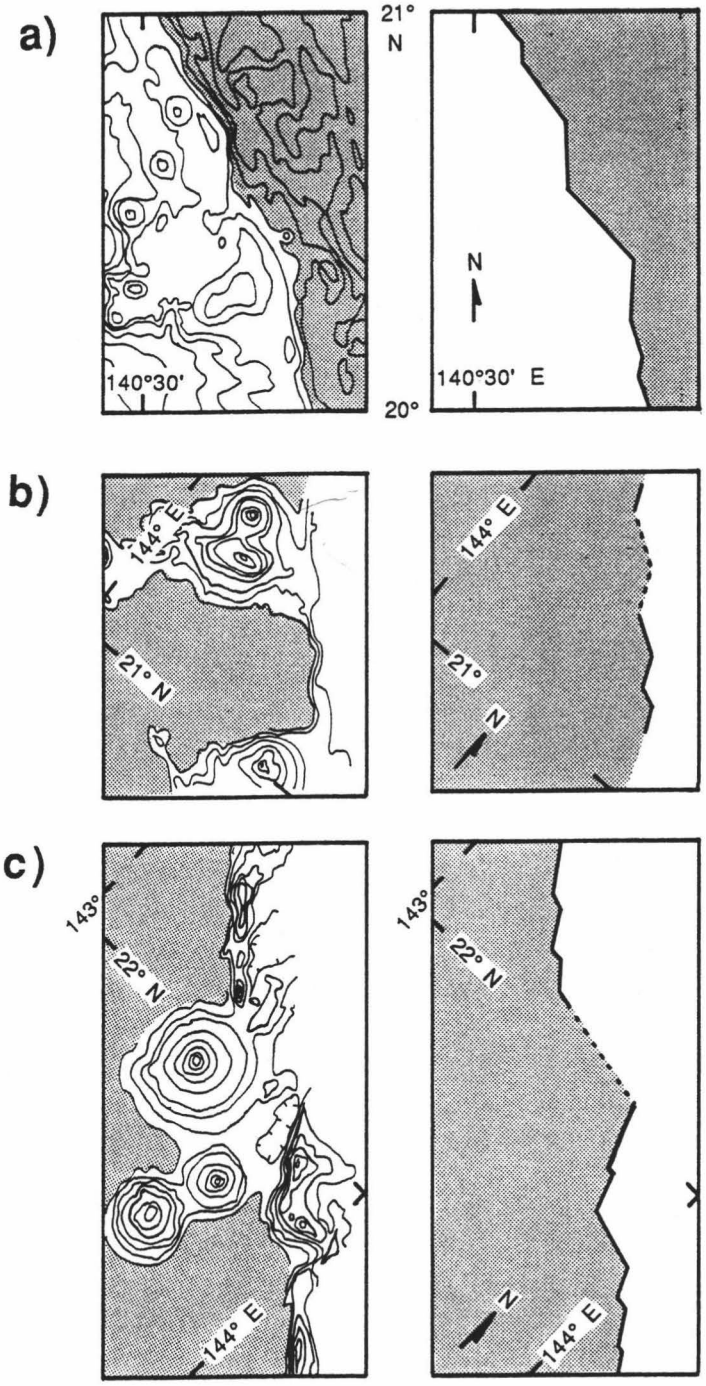

Fig. 18. Zigzag trends of the boundary faults of the Mariana backarc basin (shaded region). Although arc volcanoes have obscured much of the rift flank uplift, the visible portions exhibit a zigzag fault geometry. The figures on the right show SASS bathymetry (after *Smoot* [1988]) and the figures on the left display the corresponding fault trace interpretation (dashed where buried by arc volcanoes). a) trend 1 = 7°, trend 2 = 330°, bisector = 349° for the West boundary fault. b) trend 1 = 298°, trend 2 = 334°, bisector = 316° for the EBF at 21° N. c) Approximated zigzag trend of EBF near 22° N. Trend 1 = 290°, trend 2 = 334°, bisector = 312°. Average bisector for the EBF from b and c is 314°.

boundary faults comprise an orthorhombic set, formed under triaxial strain during rifting, of which the maximum direction of extension is the perpendicular bisector of the bounding fault sets. Along a 2° segment of the EBF, between 21° N and 23° N, the mean bisector of the zigzag trends measured 314°. As I am able to measure only one "branch" of this zigzag in the survey area, my estimate of maximum extension direction, ε_3, must be biased. This bias is assessed by measuring the difference between the "local" EB principal mode and the bisector to the "regional" zigzag EBF trace (Figure 19a). On a more regional scale of at least 2°, ε_3 perpendicular to the bisector at 314°, and not to the modes calculated in the survey, is required to produce the EBF. It can be seen that the EB major fault mode in the survey represents the northern branch of the zigzag. Therefore, the bias in maximum extension direction estimated from the major fault data of zone 1a is as much as -18°, and +5° if estimated from the combined faults of zone 1a (Figure 19b).

The finite strain ellipsoids deduced from the combined fault data represent the mean strain accommodated by faulting over an entire zone (Figure 20), whereas the major faults are a better indicator of the strain associated with the major structures (Figure 21; see Table 7 for a summary). In the case of zone 1b, where the two modes are nearly equal in magnitude, extension may alternate between two directions, being either spatial or time dependent. A single compromising extension direction would demand a substantial shear component in both trends. Of course, lack of strike-slip evidence does not preclude its existence, but there is no reason to demand strike-slip motion when alternative explanations are feasible.

In both the combined and major fault data a systematic and progressive change in the strain field across the region is evident. From zones 1a to 3, combined fault data show an apparent reorientation in extension of 91° locally and 86° regionally. The major fault data have a relative reorientation of 68° locally and 86° regionally (Figures 20 and 21). (Where the "regional" strain field accounts for the large-scale orthorhombic symmetry of the boundary faults, and the "local" strain field refers to that deduced from only the fault data within the survey area.) The slight difference in local strain regimes between major and combined faults in zones 1a and 1b result from the increased variability of the minor faults in the interference region. These minor faults may be a result of the interference pattern between the EB and forearc major faults. Again, the end result shows that over an area 60 by 90 km two nearly normal extensional fault regimes have formed.

Next, I analyze the strain regime across the Mariana platelet at 22° N to consider the influence of backarc spreading and oblique subduction on the survey area. Deformation in

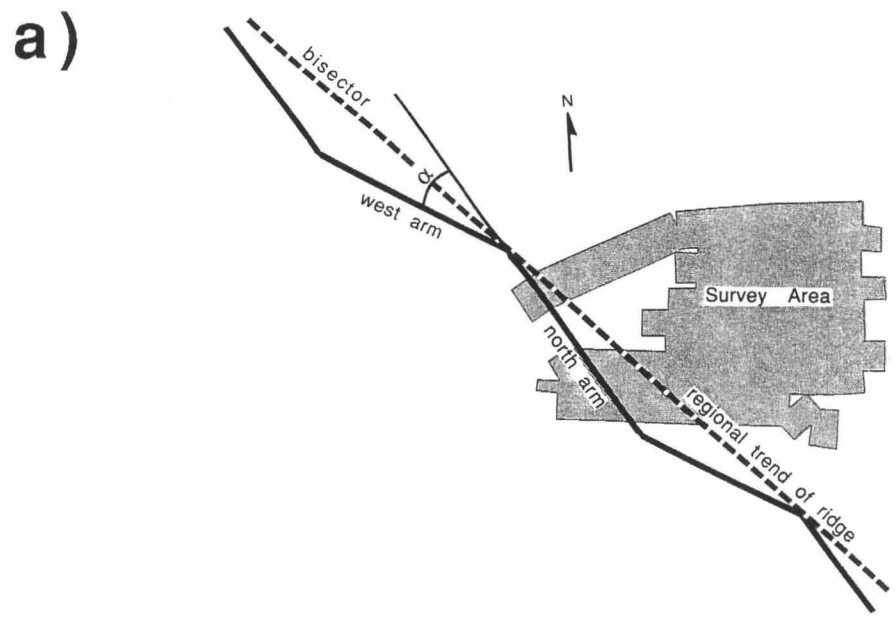

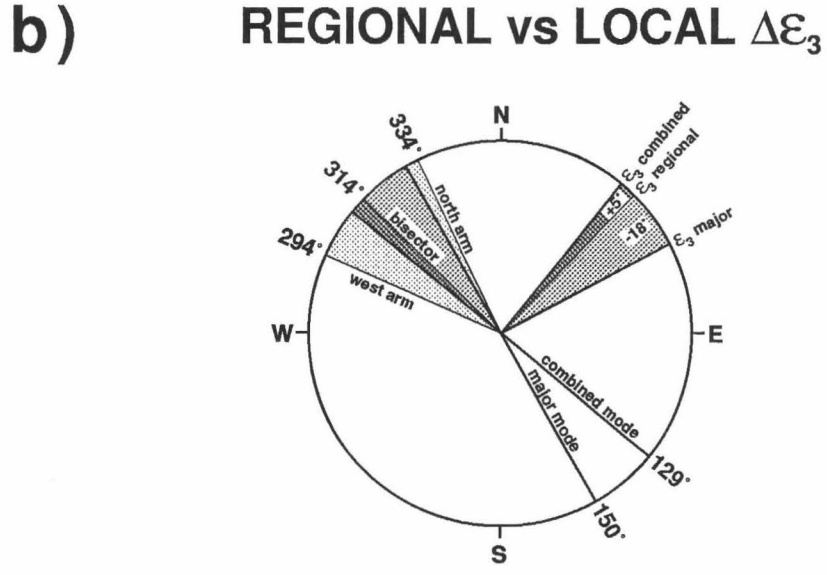

Fig. 19. Estimating the bias in the maximum direction of extension about local trends resulting from surveying only one arm of the regional zigzag EBF trace. a) Schematic diagram of the survey area and the EBF. Dashed line shows the bisector of the acute angle, α, between zigzag trends, which is also the regional trend of the Mariana ridge between 20° and 22° N. b) Using the average bisector of 314° determined for the regional zigzag trend of the EBF in figure 18, the bias in local extension directions for master faults is -18° and for combined faults is +5°. Note that the major faults approximate the trend of the north arm of the zigzag, and the combined faults appear to comprise both west and north arm faults resulting in a mean azimuth near the regional bisector. This is possible because the majority of major and minor faults are spatially separate in zone 1a.

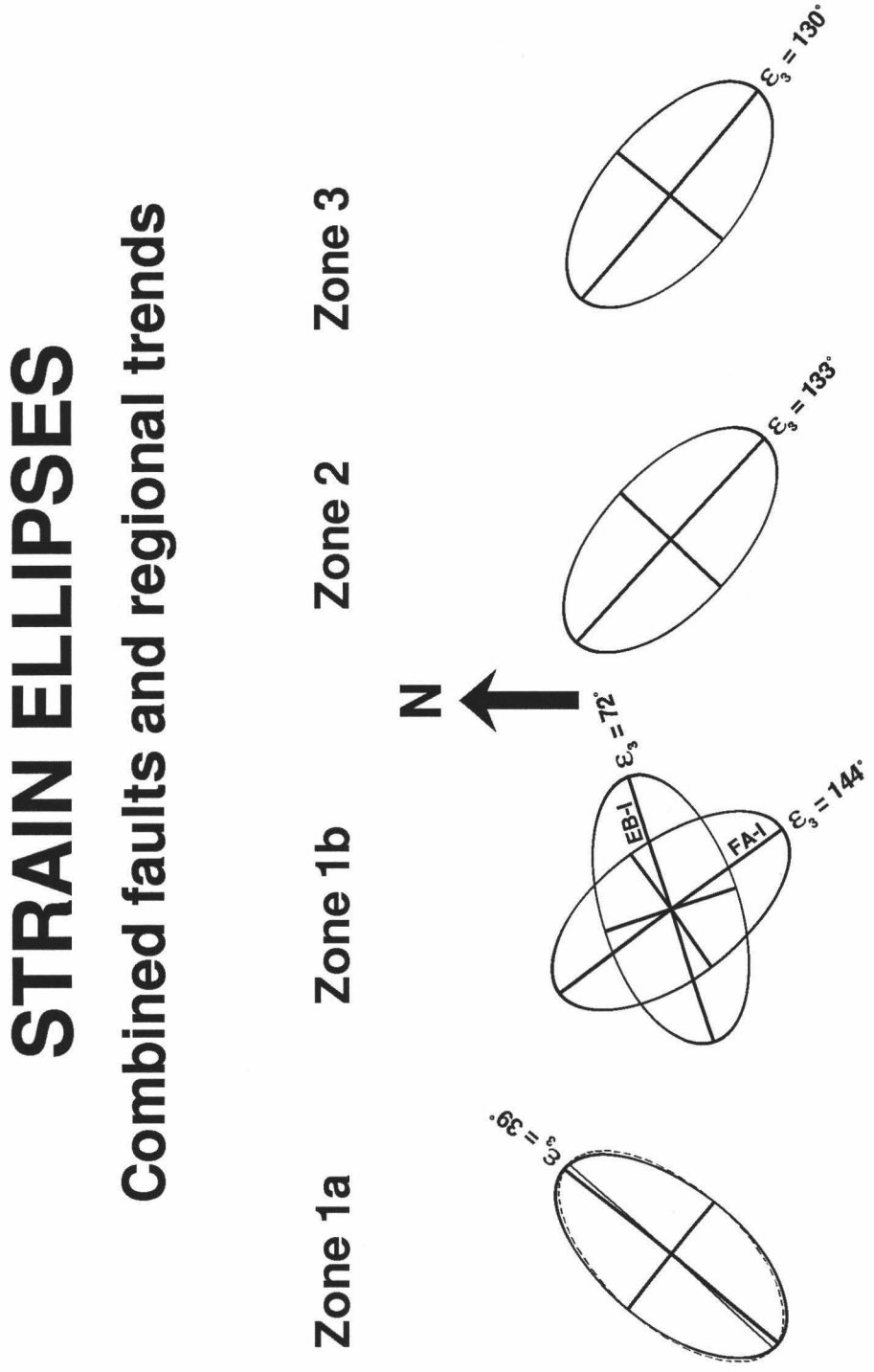

Fig. 20. Orientations of principal strain axes deduced from combined faults for each zone. Maximum extension is assumed perpendicular to the dominant mode, except in the case of zone 1b where the two modes are equal in magnitude, but not genetically related. Here extension may occur in two directions, being either space or time dependent. The ellipse labeled EB-I depicts the maximum extension direction of the EB-interference mode in zone 1b. Likewise, FA-I shows extension for the forearc-interference mode in zone 1b. The change in the maximum direction of extension, from zone 1a to zone 3, is 91°. The regional extension direction for the EBF estimated in figure 19b is shown by the dashed ellipse.

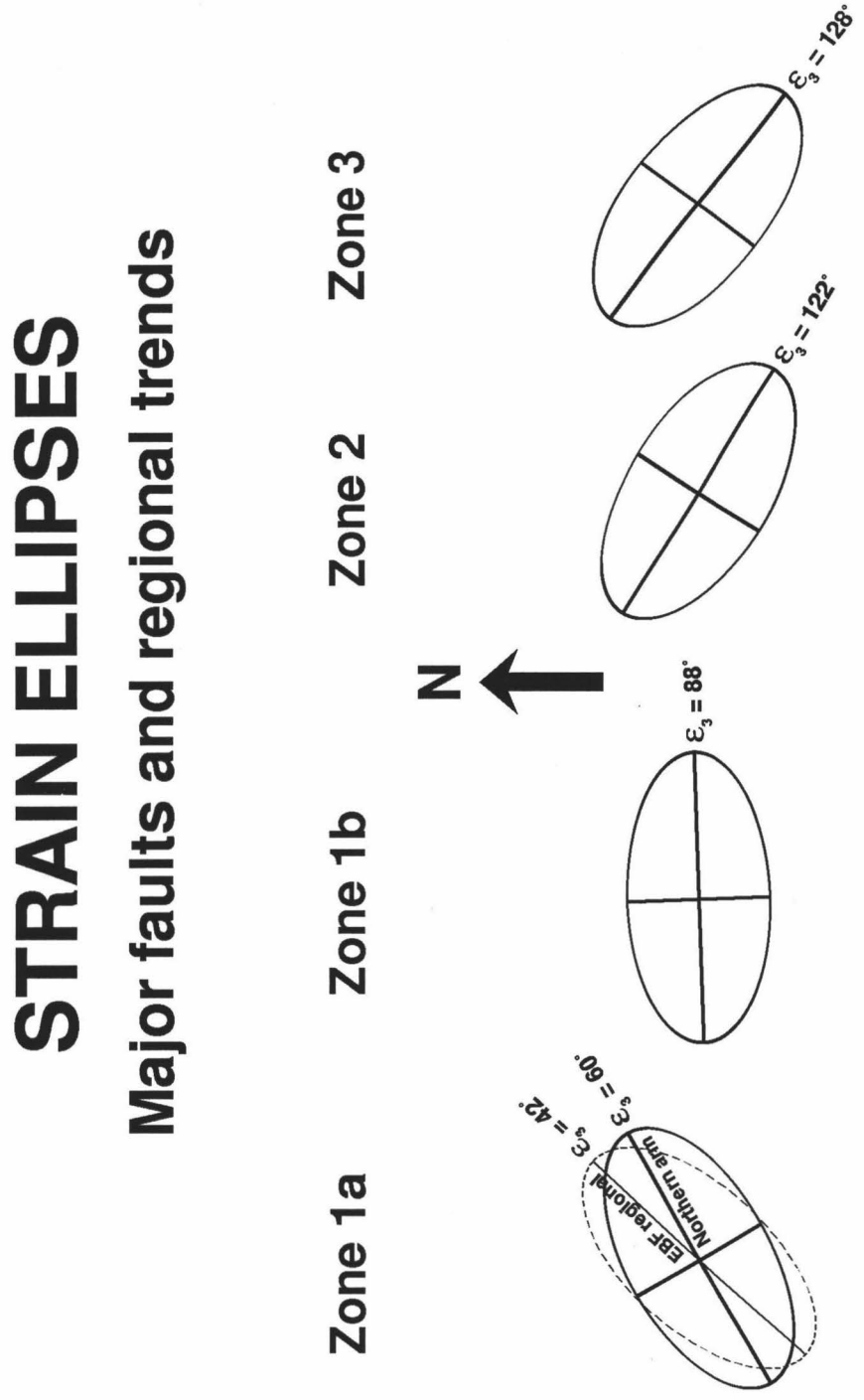

Fig. 21. Orientations of principal strain axes deduced from major faults for each zone. It is predominantly the major faults that exhibit orthorhombic symmetry. They represent a somewhat clearer picture of the strain associated with the major structures across the survey area. Again, the same systematic change in the strain field across the region is evident with the difference in extension from zones 1a to 3 being 68° locally and 86° regionally.

the northern Mariana backarc basin is distinct from that of the central and southern portions [*Beal*, 1987; *Stern et al.*, 1984]. Active spreading ridges identified in the backarc basin at 22° N by *Beal* [1987] and *Smoot* [1990] have an average trend of 329° (Figure 22). Earthquake solutions and structural characteristics indicate extension is perpendicular to the constructional ridges [*Eguchi*, 1984; *Karig et al.*, 1978], therefore maximum extension is oriented towards 59° (239°) in the northern part of the basin.

The principal strain orientation in the backarc basin coincides with that for the EB major faults and the principal forearc extensional strain direction closely parallels the highly oblique, relative Pacific plate motion at 22° N. The resultant analysis shows that the distribution of surface strain over a distance of about 220 km in the overriding Mariana platelet appears to be distinctly partitioned between the backarc and forearc (Figure 23). The transition to an orthogonal extension direction occurs across a narrow zone approximately 20 km wide that lies along the arc massif.

DISCUSSION AND CONCLUSIONS

To summarize, analysis of the data across the Mariana arc at 22° N reveal two distinct strain regimes with a difference in minimum principal strain direction of 86°- 91° (combined faults). The forearc fault population has a principal direction of 42° and is comprised of normal major faults arranged in orthorhombic symmetry with subparallel synthetic and anastomosing minor faults. The principal direction of the EB fault population has an azimuth of 129° (combined faults). Regionally, both the west and east boundary faults of the northern Mariana backarc basin display the typical zigzag expression of orthorhombic symmetry. The minor faults of zones 1a and 1b are predominantly antithetic and appear to alleviate small stresses within crustal blocks caused by movement along the major bounding faults. In zone 1b, which encompasses most of the interference region, the intermediate and minimum principal strain directions are nearly equal in magnitude with orientations midway between the forearc and EB directions and clearly represents a composite strain field. Interpretation of SeaMARC II and seismic reflection data indicate concurrent fault development of the two regimes and activity since the last sedimentary deposition. There is no clear evidence of strike-slip or reverse dip-slip motion. Minor volcanism is active in the backarc basin and along the EBF within the study area.

In an effort to explain the formation of two orthogonal extensional fault regimes within the Mariana platelet, I will discuss five scenarios. The first two possibilities stipulate that

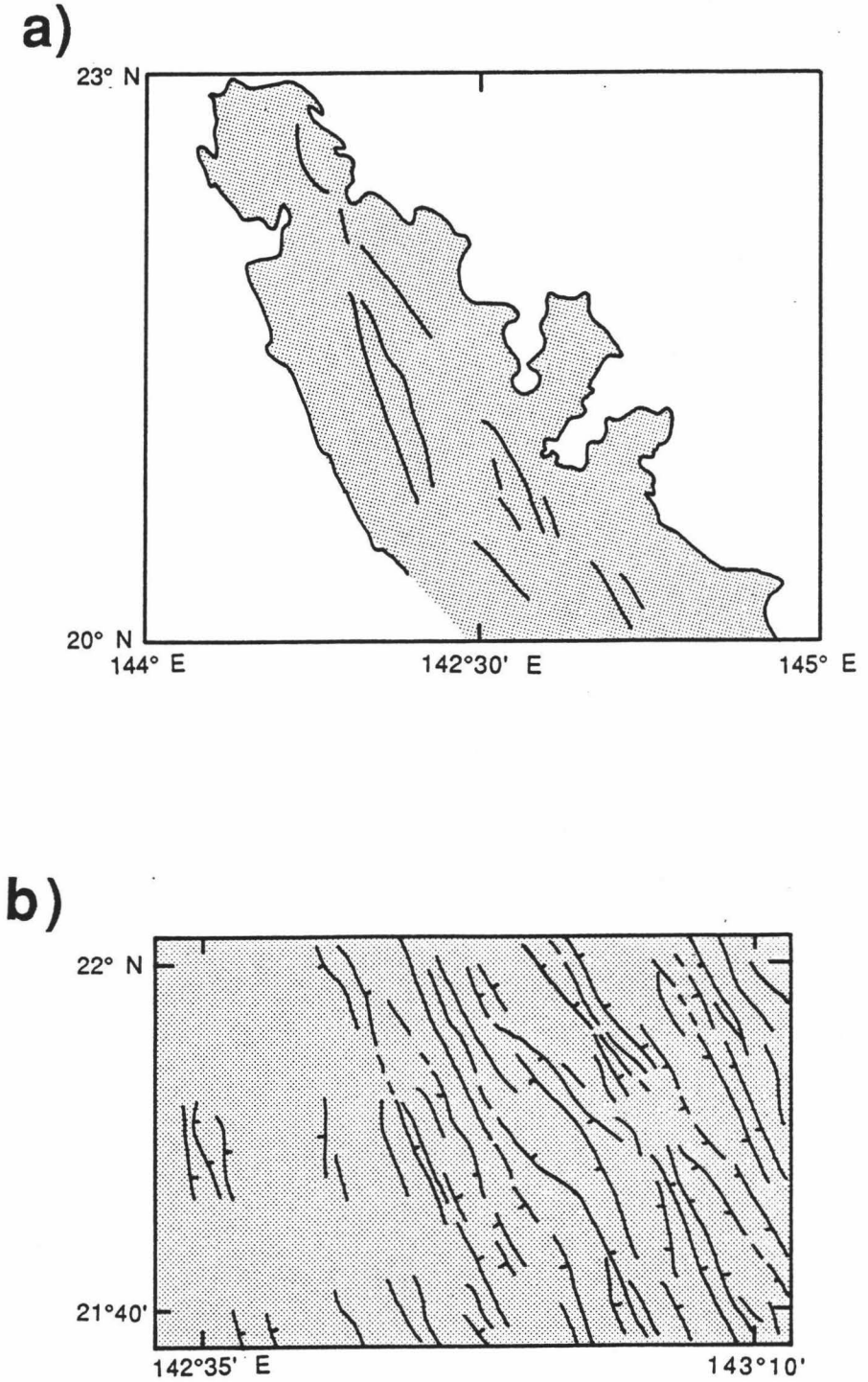

Fig. 22. a) Measurement of extensional ridges in the backarc basin near 22° N give an average trend of 329°. Backarc extension can be estimated for this northern region of the basin assuming perpendicular spreading to give a sense of regional strain. The backarc basin is shaded. a) Interpretation of major ridges off SASS bathymetry (modified from *Smoot* [1988]). Average trend is 330°. b) Interpretation of constructional ridges from SeaMARC II data (modified from *Beal* [1987]). Average trend is 328°.

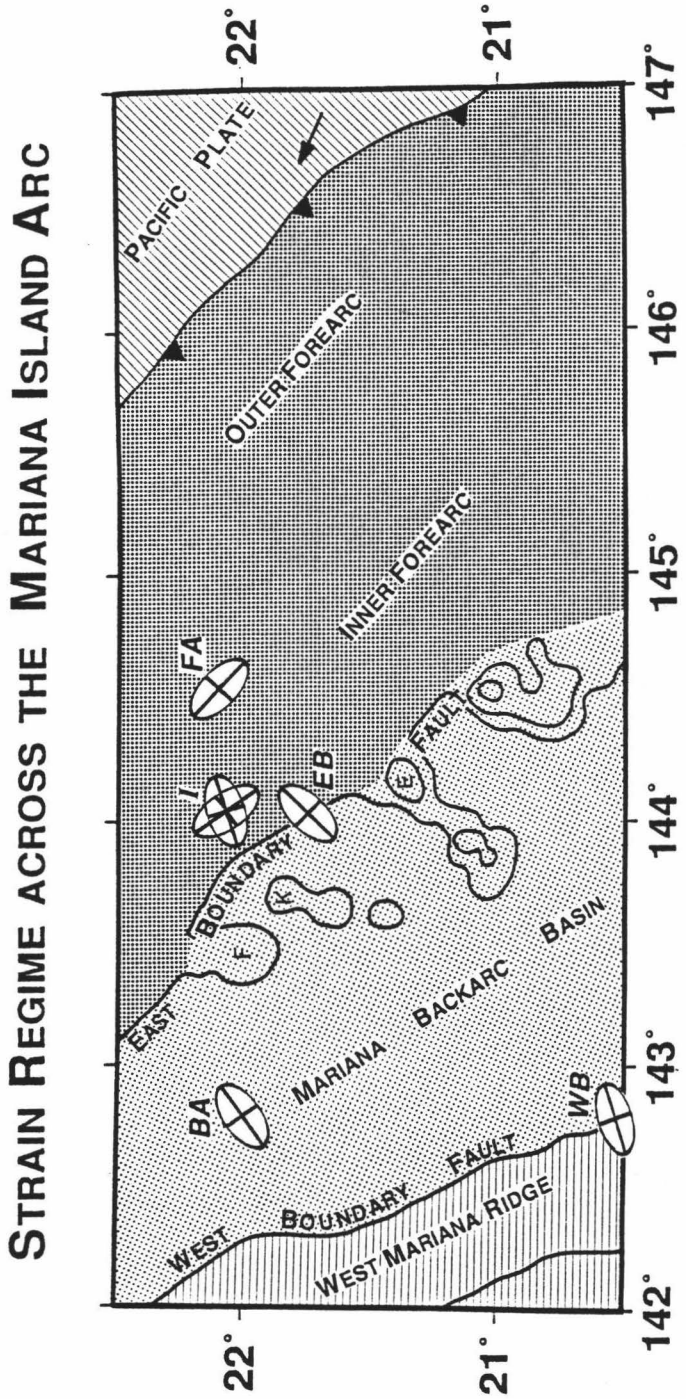

Fig. 23. Schematic diagram showing the strain regime across the northern Mariana arc based on both regional and local estimates. Note that the principal forearc mode is taken to be 42°, the mean of zones 2 and 3; and the principal EB mode is 129°, the dominant mode in zone 1a. The following submarine volcanoes are labeled as F for Fukujin, K for Kasuga and its associated volcanic cross-chain, E for Eifuku and its associated volcanic cross-chain. It is clear that the northern backarc basin displays a single strain regime that is orthogonal to that of the forearc. The transition in strain is distinct and abrupt occurring across the arc massif, along the back slope of the hanging wall of the EBF.

two generations of faulting have occurred, each in response to different stresses, and that the data is insufficient to establish relative ages. The first scenario (I), then, requires that the EBF is older and inactive, and therefore formed before the presently active forearc regime. Previous analyses of extension in the Red Sea rift have suggested that when rifting organizes into discrete spreading centers, extensional deformation becomes focussed from a broad area into a localized region about the spreading axis [*Cochran and Martinez*, 1988]. Therefore, an inactive EBF would imply that spreading has become organized and associated faulting is now confined within the backarc basin at 22° N. *Stern et al.* [1984], *Beal* [1987], and *Jackson* [1989] report evidence of spreading-related volcanism in the backarc basin as far as 23° N, though north of 21° the spreading center is not well defined [*Beal*, 1987; *Stern et al.*, 1984]. Perhaps low sedimentation rate along with gravity sliding and minor adjustments along the EBF, and its relatively high bathymetric relief compared to the surrounding region, have kept the EBF from accumulating any significant sediment to cover the faults in zone 1a. In this case, zone 1b can no longer be explained as the consequence of two interfering stress regimes. Instead, it may be the result of a deflection of stresses with proximity to the fault plane of the EBF. Simplistically, the frictional forces along the EBF plane perturbs the forearc stress field locally, causing the fractures to bend parallel to the fault plane as they propagate through the forearc crust towards the EBF. Therefore, scenario I is conceivable, but more information as to the relative ages of the fault populations and the state of development of the backarc basin spreading center is needed to test this hypothesis.

In the second scenario (II), the forearc regime precedes the EBF. This would entail that extension in the forearc would have ceased at least 3 Ma (youngest age estimated for the opening of the central part of the Mariana backarc basin) and that no further sedimentation of the forearc has occurred since to bury the faults. It would, however, be difficult to isolate the forearc completely from all sedimentary processes for any length of time. With explosive, shallow submarine and subaerial volcanic eruptions along the present-day arc to the north and south of the survey area, ash fallout would result in at least some sedimentation draping the faults. The data, however, exhibits recently faulted sediment with no evidence of sediment draping.

Taking into account the evidence for simultaneous deformation cited previously, the following three scenarios are based on both fault regimes being developed contemporaneously. In the third scenario (III), the two fault populations accommodating a single strain regime is considered. If the strain field consists of two equally extensional,

yet mutually perpendicular strain directions, this would produce a radial distribution of faults having no preferred direction, unless pre-existing structures have influenced the orientation of faulting. In the evolution of the Parece Vela-West Mariana-Mariana arc systems, each succeeding arc has become more arcuate in plan view. Since this process of deforming and stretching the forearc has occurred in the past, we might expect to find some inherited fabric in the forearc. Pre-existing structures, such as faults, can influence the way in which stress is released (and strain is accommodated), but identifying pre-existing faults after second generation faulting is virtually impossible with the present data. An alternative solution might be that a single extension direction lies between the two (EB and forearc) trends. This would require either both regimes to be pure strike-slip, (an improbable motion along the boundary faults to rift grabens) or that the EBF has a minor component of oblique slip and the forearc trend is predominantly compressional with some strike-slip motion. As the data best supports normal fault development with no component of shear or compression, this scenario is doubtful.

Speculating on the possibility of two separate strain regimes that are time-dependent, a fourth scenario (IV) might be that extensional activity is episodic, alternating between two directions over time. Unfortunately, it is difficult to find a tectonic mechanism that would cause the strain regime to alternate by such a high angle over relatively short time intervals. For this reason, I dismiss this explanation.

The fifth (V) and final scenario requires that contemporaneous fault development be spatially separated. This implies that the backarc basin at 22° N is undergoing extension broad enough to encompass the EBF. Previous models for the development of extensional styles of rifts propose a temporal relationship of the focussing of extensional deformation from a broad to a narrower region [*Buck*, 1990; *Chorowicz et al.*, 1987; *Cochran and Martinez*, 1988]. At a stage before spreading centers, having significant magmatic intrusions, are well developed in the rift basin, deformation is concentrated mainly along the bounding graben faults [*Chorowicz et al.*, 1987]. During this stage these rift flanks experience uplift [*Chorowicz et al.*, 1987; *Weissel and Karner*, 1989]. As rifting organizes into discrete spreading centers, deformation is further restricted to the central rift axis [*Cochran and Martinez*, 1988]. Following these hypotheses, present-day normal fault activity along the EBF indicates that spreading in the Mariana backarc basin at 22° N is not yet well-developed, but rather is in what *Chorowicz et al.* [1987] call the "typical rift stage".

Zone 1b and its borders reveal forearc faults that appear to bend as they approach the EBF. In the context of scenario V, zone 1b can be explained as either being affected by the frictional forces along the EBF plane (as in scenario I), or alternatively as an "interference" zone between two stress fields. The latter would entail that as the two opposing stress fields approach, the field lines rotate to accommodate the change in stress directions. This narrow sliver, approximately 20 km wide, incorporates most of the volcanic arc massif and acts as the transition zone between the two strain regimes. The lithosphere along the volcanic arc massif is thought to be weaker than the adjacent forearc lithosphere as a result of its crustal thickness and high thermal gradient [*Buck*, 1990; *Kusznir and Park*, 1987]. This may allow the lithosphere to behave structurally like a "neutral" (or more ductile) zone, enabling the narrow transition and "partitioning" of strain between the backarc and forearc. In addition, considering that the kinematics of the EBF rift flank serves to decouple the upper and lower parts of the extending lithosphere [*Weissel and Karner*, 1989], it might also enable further partitioning of some of the surface strain between the backarc and forearc. In the latter case, the narrow zone, represented predominantly by zone 1b, separates the backarc strain regime from the forearc strain regime. The former case necessitates that strain is partitioned at the EBF and that zone 1b is the resultant of the EB fault plane "edge effect".

The backarc regime is in extension approximately perpendicular to the local trend of the volcanic arc. The EBF is genetically related to the backarc extension and Figure 23 shows that the principal strain directions are approximately the same. Unfortunately, the causes of backarc extension are not well understood. One proposed mechanism is trench rollback—the seaward migration of the subduction hinge under the influence of gravity [*Dewey*, 1980; *Molnar and Atwater*, 1978]. The forearc regime is in extension parallel to the arc at 22° N. The breadth of this regime is at least 80 km and most likely extends beyond the inner forearc. Arc-parallel extension connotes increased arc curvature for the northern portion of the Mariana island arc.

Distinct partitioning of strain within an island arc has been observed in a few other arcs where plate convergence is oblique and detailed study has been accomplished. The distinct partitioning of strain of the supra-subduction zone has been observed in the Hikurangi forearc, New Zealand [*Cashman and Kelsey*, 1990]. The southern end of the Ryukyu arc displays arc-parallel extension in the forearc [*Kuramoto and Konishi*, 1989] with some strike-slip towards the western extremity and backarc extension sub-parallel to the arc. *Sibuet, et al.* [1987] interpreted this as en echelon extensional features as a consequence of

oblique subduction. The data from these two publications reveal the distinct and abrupt partitioning of strain from the backarc into the forearc.

Several models for backarc opening and arc curvature predict arc-parallel extension in the forearc. Radial expansion of the forearc as a consequence of pinning either the northern or both subduction hinges by aseismic ridges would create radial tension fractures as subduction progressed faster in the central part of the arc than at the ends [*Hsui and Youngquist*, 1985; *Karig et al.*, 1978; *Vogt et al.*, 1976]. Pinning of the northern end by the Ogasawara Plateau while the south is a free end, as suggested by *Karig et al.* [1978], would produce variable deformation from north to south along the Mariana forearc, with the northern end experiencing more tension. In addition, highly oblique plate convergence and decoupling along the subduction zone, as exists at the northern Mariana trench, might facilitate arc-parallel stretching of the forearc. The variable rate of hinge migration westward along the Izu-Bonin-Mariana arcs with a large increase from the central Mariana trench at 18° N to the Ogasawara Plateau at 27° N suggests that the forces that may cause trench rollback also cause increased arc-curvature that in turn deforms the forearc [*Carlson and Mortera–Gutierrez*, 1990].

In conclusion, scenario V appears to be the most realistic and compatible with the data from this study. To further test this hypothesis and its implications, detailed coverage using side-scan sonar and bathymetric swath mapping devises, will be necessary to map the extent and distribution of the faults and lineaments in the backarc and forearc. Migrated multi-channel seismics would better constrain fault dips and motion to enable quantitative extension measurements and 3-D strain analysis. Coring might enable the determination of the relative ages of fault populations. One would expect to find that extension increases in magnitude towards the trench, if the forearc were being deformed into an increasingly arcuate shape. More detailed data at 22° N would enable further insight as to the mechanisms and plate geometries responsible for such deformation at a convergent margin, and would shed light on the mechanics of backarc rifting, arc curvature, and forearc deformation.

Table 1a. Preferred model solutions of minor faults and lineaments from zone 1a

mode	2μ	h	2w	μ	w
1	228.4±3.4	18.1±1.3	245.5±20.3	114.2±1.7	122.8±10.1
2	81.7±5.6	8.1±1.2	321.4±55.7	40.9±2.8	160.7±27.9
R	–	0.9±1.4	–	–	–

Table 1b. Preferred model solutions of minor faults and lineaments from zone 1b

mode	2μ	h	2w	μ	w
1	111.3±5.3	7.9±0.8	288.4±38.4	55.6±2.7	144.2±19.2
2	307.5±6.7	5.8±0.6	303.6±48.3	153.8±3.3	151.8±24.2

Table 1c. Preferred model solutions of minor faults and lineaments from zone 2

mode	2μ	h	2w	μ	w
1	96.9±1.7	38.3±1.9	211.9±5.8	48.5±0.9	105.9±2.9
2	329.2±3.7	10.8±0.6	261.9±12.8	164.6±1.8	130.9±6.4

Table 1d. Preferred model solutions of minor faults and lineaments from zone 3

mode	2μ	h	2w	μ	w
1	85.3±0.9	47.3±2.1	225.2±3.7	42.6±0.4	112.6±1.8
R	–	0.7±0.1	–	–	–

Table 2a. Preferred model solutions of major faults from zone 1a

mode	2μ	h	2w	μ	w
1	298.9±1.4	14.1±0.7	317.2±11.0	149.4±0.7	158.6±5.5
R	–	0.5±0.1	–	–	–

Table 2b. Preferred model solutions of major faults from zone 1b

mode	2μ	h	2w	μ	w
1	356.1±9.0	4.4±0.6	232.6±28.4	178.1±4.5	116.3±14.2
2	104.8±15.5	2.0±0.5	232.0±35.5	52.4±7.7	116.0±17.7

Table 2c. Preferred model solutions of major faults from zone 2

mode	2μ	h	2w	μ	w
1	63.1±1.8	23.7±1.8	267.1±8.1	31.5±0.9	133.6±4.1
R	–	0.5±0.1	–	–	–

Table 2d. Preferred model solutions of major faults from zone 3

mode	2μ	h	2w	μ	w
1	76.0±1.6	24.7±2.1	230.5±4.8	38.0±0.8	115.2±2.4

Table 3a. Preferred model solutions of combined faults and lineaments from zone 1a

mode	2μ	h	2w	μ	w
1	257.1±2.7	28.5±2.7	332.3±29.5	128.6±1.3	166.1±14.7
2	77.2±4.5	10.6±0.7	294.6±57.0	38.6±2.2	147.3±28.5
R	–	1.4±0.0	–	–	–

Table 3b. Preferred model solutions of combined faults and lineaments from zone 1b

mode	2μ	h	2w	μ	w
1	107.4±12.9	10.1±1.1	321.9±64.1	53.7±6.4	161.0±32.0
2	324.4±13.4	8.8±1.1	291.5±61.1	162.2±6.7	145.8±30.6

Table 3c. Preferred model solutions of combined faults and lineaments from zone 2

mode	2μ	h	2w	μ	w
1	85.2±2.4	62.1±3.6	242.7±8.0	42.6±1.2	121.3±4.0
2	322.6±4.9	14.6±1.1	203.2±13.9	161.3±2.4	101.6±7.0
R	–	0.5±0.0	–	–	–

Table 3d. Preferred model solutions of combined faults and lineaments from zone 3

mode	2μ	h	2w	μ	w
1	80.6±1.0	68.1±3.9	251.4±4.1	40.3±0.5	125.7±2.0
2	259.2±1.9	2.0±0.2	135.5±11.2	129.6±1.0	67.7±5.6

Table 4a. Summary of preferred models of minor faults and lineaments for zone 1a

modes	Variance reduction	rms	Q	Significance
1	87.3 %	3.89 km	1.5×10^{-40}	100.0 %
2 + R	96.1 %	2.15 km	5.8×10^{-8}	99.4 %
3	96.4 %	2.07 km	9.0×10^{-7}	3.4 %

Table 4b. Summary of preferred models of minor faults and lineaments for zone 1b

modes	Variance reduction	rms	Q	Significance
1	83.3 %	2.28 km	7.6×10^{-8}	100.0 %
2	94.7 %	1.29 km	0.073	98.3 %
3	96.4 %	1.05 km	0.264	50.1 %

Table 4c. Summary of preferred models of minor faults and lineaments for zone 2

modes	Variance reduction	rms	Q	Significance
1	61.9 %	10.8 km	3.0×10^{-85}	99.5 %
2	95.3 %	3.81 km	1.0×10^{-21}	100.0 %
3	97.3 %	2.86 km	3.5×10^{-19}	52.2 %

Table 4d. Summary of preferred models of minor faults and lineaments for zone 3

modes	Variance reduction	rms	Q	Significance
1 + R	97.7 %	3.18 km	8.1×10^{-30}	100.0 %
2+ R	97.6 %	3.26 km	5.7×10^{-16}	22.0 %

Table 5a. Summary of preferred models of major faults for zone 1a

modes	Variance reduction	rms	Q	Significance
1 + R	90.2 %	2.81 km	4.6×10^{-84}	100.0 %
2 + R	93.2 %	2.34 km	2.8×10^{-72}	29.7 %

Table 5b. Summary of preferred models of major faults for zone 1b

modes	Variance reduction	rms	Q	Significance
1	86.8 %	3.26 km	1.1×10^{-85}	100.0 %
2	93.4 %	0.64 km	0.739	96.0 %
3	94.1 %	0.61 km	0.884	23.6 %

Table 5c. Summary of preferred models of major faults for zone 2

modes	Variance reduction	rms	Q	Significance
1 + R	96.0 %	2.44 km	0.001	100.0 %
2 + R	96.3 %	2.34 km	9.3×10^{-7}	40.5 %

Table 5d. Summary of preferred models of major faults for zone 3

modes	Variance reduction	rms	Q	Significance
1	96.8 %	2.30 km	0.924	100.0 %

Table 6a. Summary of preferred models of combined faults and lineaments for zone 1a

modes	Variance reduction	rms	Q	Significance
1	90.5 %	5.64 km	6.0×10^{-17}	100.0 %
2 + CR	96.8 %	3.30 km	0.0009	98.4 %

Table 6b. Summary of preferred models of combined faults and lineaments for zone 1b

modes	Variance reduction	rms	Q	Significance
1	90.3 %	2.40 km	0.028	100.0 %
2	96.1 %	1.52 km	0.653	95.4 %

Table 6c. Summary of preferred models of combined faults and lineaments for zone 2

modes	Variance reduction	rms	Q	Significance
1	83.7 %	11.70 km	1.9×10^{-35}	100.0 %
2 + CR	97.3 %	4.78 km	4.3×10^{-10}	99.9 %
3	98.9 %	2.97 km	3.7×10^{-9}	73.2 %

Table 6d. Summary of preferred models of combined faults and lineaments for zone 3

modes	Variance reduction	rms	Q	Significance
1	96.6 %	5.99 km	3.3×10^{-42}	100.0 %
2	98.3 %	4.17 km	6.0×10^{-5}	97.0 %
3	98.6 %	3.82 km	1.2×10^{-4}	18.7 %

APPENDIX A

ON THE DETERMINATION OF MULTIPLE MODES IN CIRCULAR DATA†

ABSTRACT

In many branches of the Earth sciences one seeks to determine the principal modes of a multi-modal, circular frequency distribution. This is especially true for analysis of directional features like drumlins and oriented features such as lineaments and fault traces. Although statistical procedures for analyzing single and bimodal distributions have been developed, for more than two modes the traditional approach has commonly been to group circular data in bins of a selected sector width and visually determine the modal directions from a rose or sector diagram of the binned data. Besides being subjective and possibly biased, shortcomings of this method include a lack of error estimates and significance estimates of the selected modes. If one assumes that the errors associated with a given data set approximately follow a normal distribution, these drawbacks are overcome by treating the problem as one of nonlinear curve fitting. By approximating each mode by a Gaussian density distribution function, one or more modes can be fit to the data set using standard techniques for solving nonlinear inverse problems. A goodness-of-fit measure is derived from χ^2, the chi-square statistic, and the criterion for determining how many modes are necessary to fit the data comes from the F-test using χ^2 values for two competing models differing in number of modes. We show examples of the versatility of this method using both synthetic and real data sets.

---

† Slightly modified from a paper by Pål Wessel and Jill K. Wessel submitted to *Journal of Structural Geology*, spring 1991.

INTRODUCTION

The determination of dominant trends in a data set of directional (having a unique azimuth) and oriented structures (being one of two opposite azimuths) in the plane is important in a variety of scientific disciplines. For example, in studies of structural geology and tectonics, the geologist may need to analyze the troughs of festoon cross-bedding (a directional structure) to find the direction of current flow [e.g., *Compton*, 1985] or a set of fault orientations to determine the directions of principal strains [e.g., *Ramsey*, 1967]. To avoid a biased interpretation it is desirable to select the dominant modes in a manner which is both objective and which relies on established statistical criteria for determining the error estimates and significance of a particular solution. Modes obtained by visual inspection of graphical representations of the data do not meet such rigorous criteria, and should be treated with some skepticism as to their accuracy and significance. However, it is clear that in some cases, the data distribution may allow the scientist confidently to pick the dominant modes, but more likely there will be overlap between modes and a more statistical approach is required. Nevertheless, the literature suggests it is quite common for geologists to rely on visual techniques when determining principal directions in their data sets [*Davis*, 1986]. Examples abound in tectonic studies on land [*Boccaletti et al.*, 1987; *Cello et al.*, 1985; *Kelsey and Cahsman*, 1983; *Lamb and Libby*, 1989], investigations of abyssal hill fabric from side scan sonar [*Kleinrock and Hey*, 1989; *Macdonald et al.*, 1986], inferences of regional stress field from micro-fractures [*Lespinasse and Pêcher*, 1986], a combination of borehole strain measurements along with fault, joint, slickensides, and stylolite orientations [*Greiner*, 1975], and directional analysis of magnetic fabric [*Rathore and Kafafy*, 1986]. This is not to say that the problems associated with visual techniques have gone unrecognized. Procedures for the statistical analysis of directional data assuming a unimodal, symmetric population have been described by many including *Krumbein* [1939], *Pincus* [1953; 1956], *Curray* [1956], *Steinmetz* [1962], *Jones* [1968], *Davis* [1986], and *Upton* [1989]. Several statistical models account for a skewed or bimodal sample distribution when calculating sample modes [*Jones and James*, 1969; *Mardia*, 1972]. However, these procedures fail when applied to multi-modal (more than 2 modes) samples. Furthermore, these techniques require that the number of modes be known *a priori*, which usually is not the case.

For most problems, the errors contributing to the scatter around each mode can be considered to be normally distributed. Hence, the complete data set may be approximated

by the superposition of one or more Gaussian functions, each characterized by its center position, width, and amplitude. The solution to the problem then becomes an exercise in nonlinear optimization, i.e., for a given number of modes, find the parameters that minimize the total misfit in a least-squares sense. Using standard techniques for solving a system of nonlinear equations, we obtain (i) unbiased estimates of the model parameters, (ii) error estimates on the parameters, (iii) a statistical measure of goodness-of-fit for the model, and (iv) a way to decide if one model is significantly better than a competing model at some predescribed level of confidence.

MULTI-MODAL MODELLING

The periodicity of circular distributions require special attention when selecting a function to represent them. Traditionally, the von Mises distribution [*Upton and Fingleton*, 1989] has been used to describe the statistical properties of a unimodal circular distribution. It is given by

$$f(x) = \frac{1}{2\pi I_0(\kappa)} \exp\{\kappa \cos(x - \mu)\}, \tag{1}$$

where κ is a measure of the concentration of the distribution about the direction μ, and I_0 is the modified Bessel function of the first kind and order zero. Although the von Mises distribution has certain pleasant properties like having its minimum and maximum 180° apart, we prefer to work with some type of normal distribution, as such distributions more accurately represent the nature of the errors in the data. A circular normal distribution may be closely approximated by the wrapped normal distribution

$$g(x) = \frac{1}{\sigma\sqrt{2\pi}} \sum_{j=-\infty}^{\infty} \exp\left\{-\frac{1}{2}\left(\frac{x + 360 \times j - \mu}{\sigma}\right)^2\right\}. \tag{2}$$

For circular data, $0° \le x < 360°$. In practice, one need only execute the summation over a finite window of width 12σ centered on μ. A model $m(x; \boldsymbol{a})$ allowing for multiple modes can now simply be described as a sum of M individual modes each represented by a wrapped Gaussian function centered at μ_j, with standard deviation σ_j and height h_j, i.e.

$$m(x; \mathbf{a}) = \sum_{j=1}^{M} g(x; \mu_j, \sigma_j, h_j). \tag{3}$$

The vector $\boldsymbol{a}$ contains the mode parameters μ_j, σ_j, and h_j for all modes. For a particular data set consisting of N data points, the problem to be solved consists of the N nonlinear equations

$$\boldsymbol{m}(\boldsymbol{a}) = \boldsymbol{y}, \tag{4}$$

where $\boldsymbol{y}$ is the observation vector. We linearize (4) by expanding the model in a Taylor series around an initial guess $\boldsymbol{a}_0$ [*Menke*, 1984]. The partial derivatives of the Gaussian are needed to compute the model gradient $\nabla \boldsymbol{m}$. The linearized system of equations then becomes

$$\nabla \boldsymbol{m}\, \Delta \boldsymbol{a}_{n+1} = \boldsymbol{y} - \boldsymbol{m}(\boldsymbol{a}_n). \tag{5}$$

Solving (5) includes providing an initial guess for the model parameters $\boldsymbol{a}_0$, and subsequently to iterate for improvements $\Delta \boldsymbol{a}$ until convergence is achieved, i.e., the reduction in misfit achieved by including $\Delta \boldsymbol{a}$ is less than a specified cutoff value. Such a scheme may successfully be implemented using standard nonlinear least-squares algorithms such as the Levenberg-Marquardt method [*Press et al.*, 1986]. The quantity to be minimized is

$$\chi^2(\boldsymbol{a}) = \sum_{i=1}^{N} \left[\frac{y_i - m(x_i; \boldsymbol{a})}{\sigma_i} \right]^2, \tag{6}$$

which gives us the least-squares solution we seek. If the σ_i all are independent and the errors are normally distributed with $\sigma_i = \sigma$, then minimization of (6) also gives us the maximum likelihood solution. We obtain standard error estimates for each model parameter from the diagonal elements of the covariance matrix $\mathbf{C} = [\nabla \mathbf{m}^T \nabla \mathbf{m}]^{-1}$.

To determine if the model actually fits the data reasonably well, we follow *Press et al* [1986] and compute the goodness-of-fit for a particular model described by M parameters

as the probability Q that a chi-square χ^2 value as poor as that given by (6) should occur by chance:

$$Q(\nu, \chi^2) = 1 - P\left(\frac{\nu}{2}, \frac{\chi^2}{2}\right) \tag{7}$$

Here, P is the incomplete gamma function and ν the degrees of freedom N-M. Small values of Q (<0.001) indicate that the model fits the data poorly. However, the estimate for Q will depend highly on the noise level assigned to the data. If the noise level is substantially underestimated, we are likely to find that even (presumably) good models will give minute values for Q. Regardless of value for Q, one is well advised always to plot the model and the data to determine if the solution looks acceptable.

For many inverse problems, the number of model parameters is not known a priori. Intuitively, a complicated model (i.e., in the sense it has more parameters, therefore more degrees of freedom) should provide a better fit to the data than a less complicated one. This fact begs the question: Does the more complicated model fit the data significantly better? We address this issue by comparing the different models using an F-test on the ratio of the relative variance between the data residuals [e.g., *Menke*, 1984]. In conclusion, the strategy we will adopt is to start solving for the best-fitting single mode, then add more parameters (i.e., modes) to the system of equations, and use the F-test to determine whether the inclusion of the Mth mode is significant compared to the previous solution. When the Mth mode is not significant at some predescribed confidence level (typically 95 %), we accept the previous solution consisting of M-1 modes as our best solution.

PRACTICAL EXAMPLES

We will now apply the method to both synthetic and real data sets and demonstrate the flexibility in the curve-fitting scheme and how it allows us to distinguish between significant and non-resolved dominant directions in circular orientation data. The theory outlined in the preceding section has been implemented in C [*Kernighan and Ritchie*, 1978] on a UNIX workstation. The program and test data sets used in this paper are available from the authors on request.

Synthetic Data Case

To test how well the method can resolve the parameters describing the best fitting solution, we generated a synthetic data set based on four modes of different center position, amplitude, and width (μ, h, w). Here, $w = 6\sigma$. The parameter values of the four modes were (80, 1000, 200), (200, 600, 150), (250, 500, 130), and (320, 400, 50). Two of the modes were closely spaced so that they would overlap to some degree. The synthetic model created by the superposition of the four modes (heavy line in Figure A-1a) was then binned using a 10° bin interval, and random Gaussian noise ($\sigma = 50$ m) was added to the binned amplitudes to make the experiment more realistic. Figure A-1a shows the binned data set and the individual modes as dashed curves on a linear azimuth–length diagram. For a more traditional viewpoint, a rose diagram of this data set and the model curves is plotted in Figure A-1b. The radius of each sector is proportional to the amplitude of each bin. Note that the modes m_2 and m_3 overlap considerably to create the impression of a single, much broader mode. One of the objectives of this test case was to investigate whether we would be able to separate out overlapping populations. After searching for candidates using the theory outlined above, Figures A-2a and A-2b presents three possible solutions, differing in the number of modes (2, 3, and 4) necessary to explain the data set. The numerical values for the resolved parameters are given in Table A-1 together with formal error estimates. As expected, the more complicated models gave better goodness-of-fit estimates Q. Table A-2 presents a statistical summary of the three possible models and how they compare to each other. Whereas the four-mode solution (dashed line) gave $Q_4 = 0.363$, the three-mode (solid line) and two-mode (dotted line) solutions produced $Q_3 = 0.007$ and $Q_2 \approx 10^{-16}$, respectively. However, at the 95 % confidence level, the F-test statistic indicated that the three-mode model was significantly better than just two modes, but that the subtle improvements offered by the four mode model were only significant at a confidence level of 78.8%. Although we know that the data set was generated from these four modes and the inversion scheme indeed was able to resolve all four modes fairly well, the fourth mode was deemed insignificant due to the noise level imposed on the data. Had the noise level been somewhat higher, the third mode would probably have been judged insignificant as well. We will now apply this technique to a real data set.

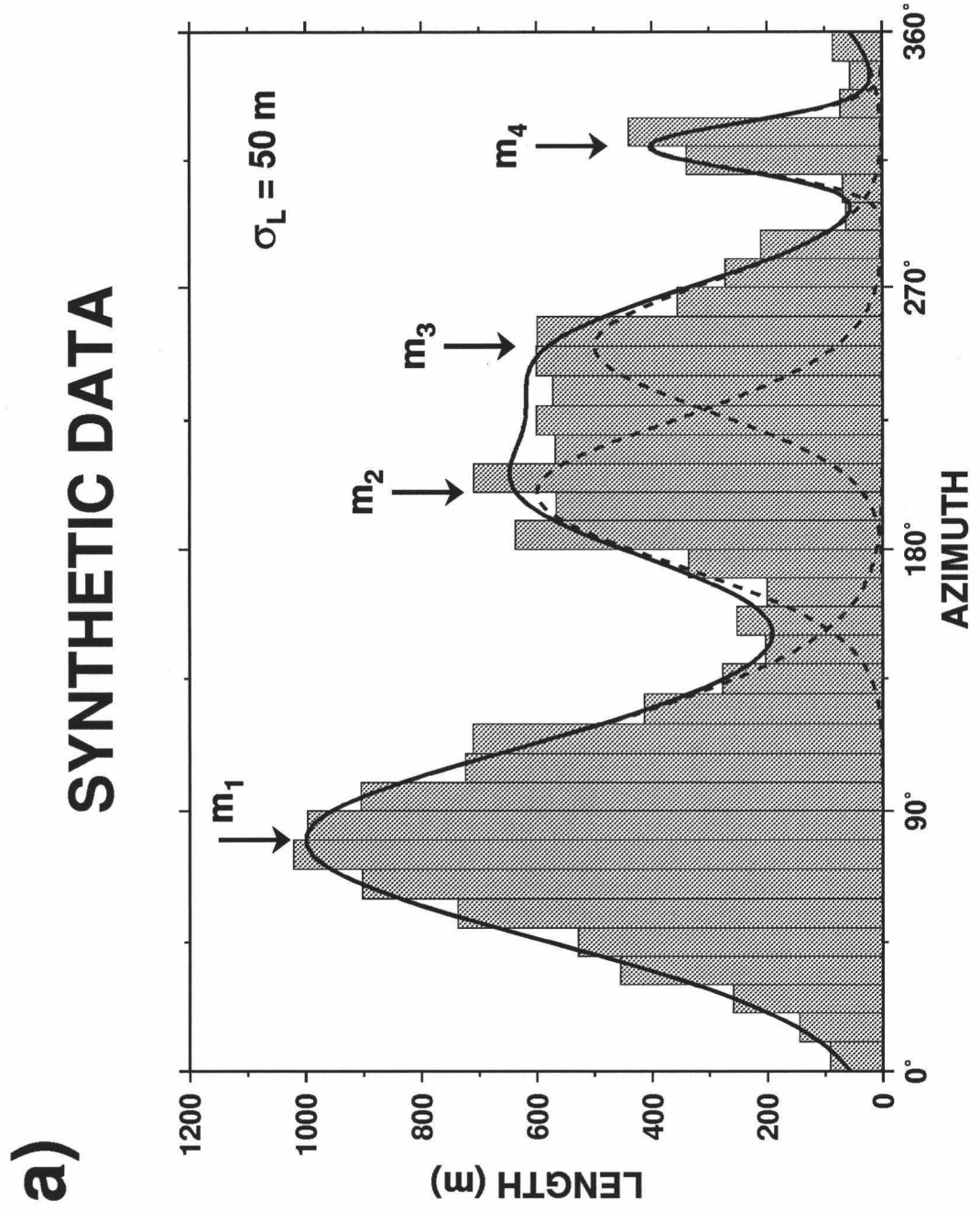

Fig. A-1a. Histogram of the synthetic data, using a 10° bin width. The noise level imposed when generating the model curves were 50 m (1 standard deviation). The center position, height, and full width (6σ) of the four modes are as follows: Mode 1 = (80, 1000, 200), mode 2 = (200, 600, 150), mode 3 = (250, 500, 130), and mode 4 = (320, 400, 50). The individual modes are drawn as dashed lines; the solid lines illustrates the combined model.

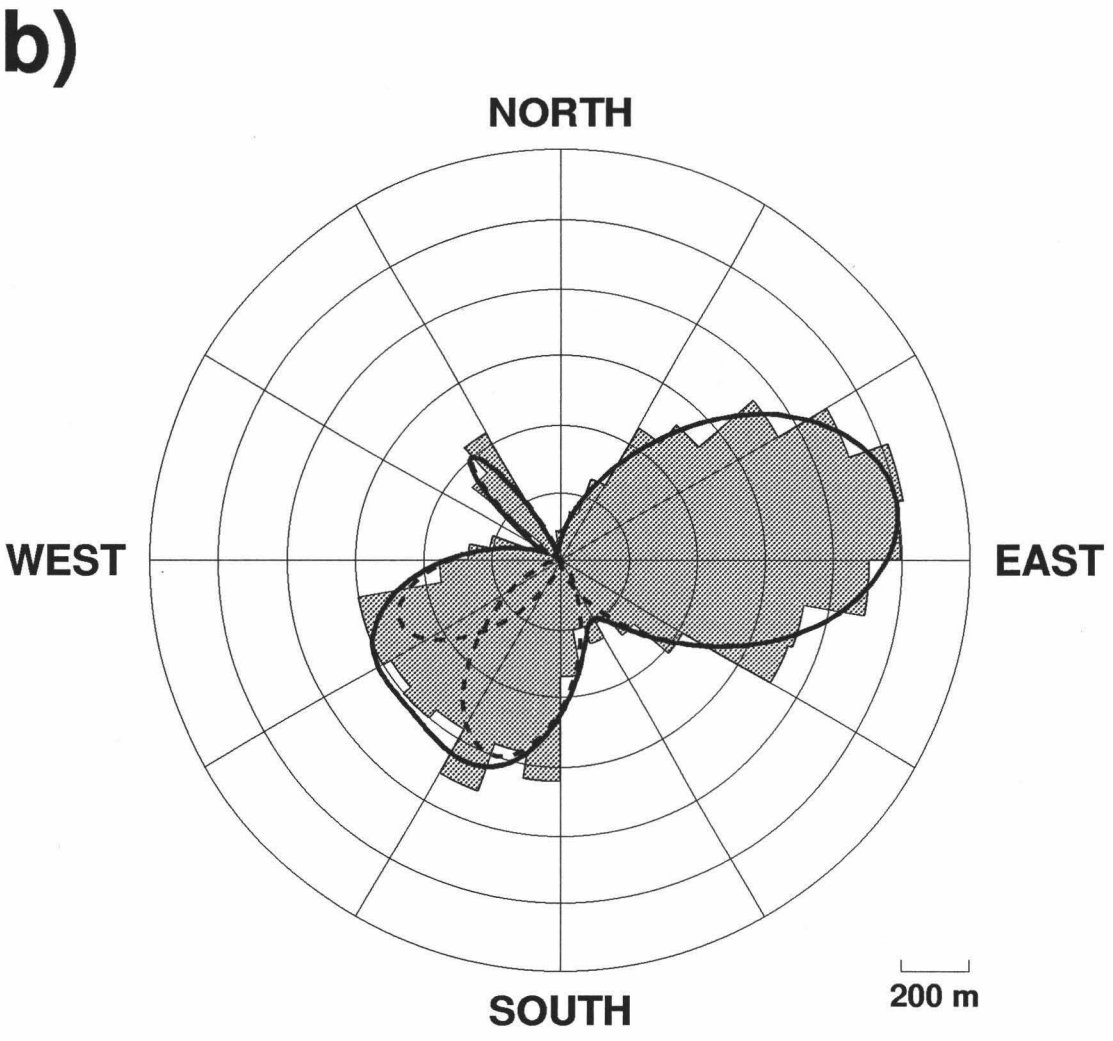

Fig. A-1b. The same synthetic data, this time displayed as a traditional sector (type of rose) diagram. The radius of the sectors are proportional to the total fracture length of each bin.

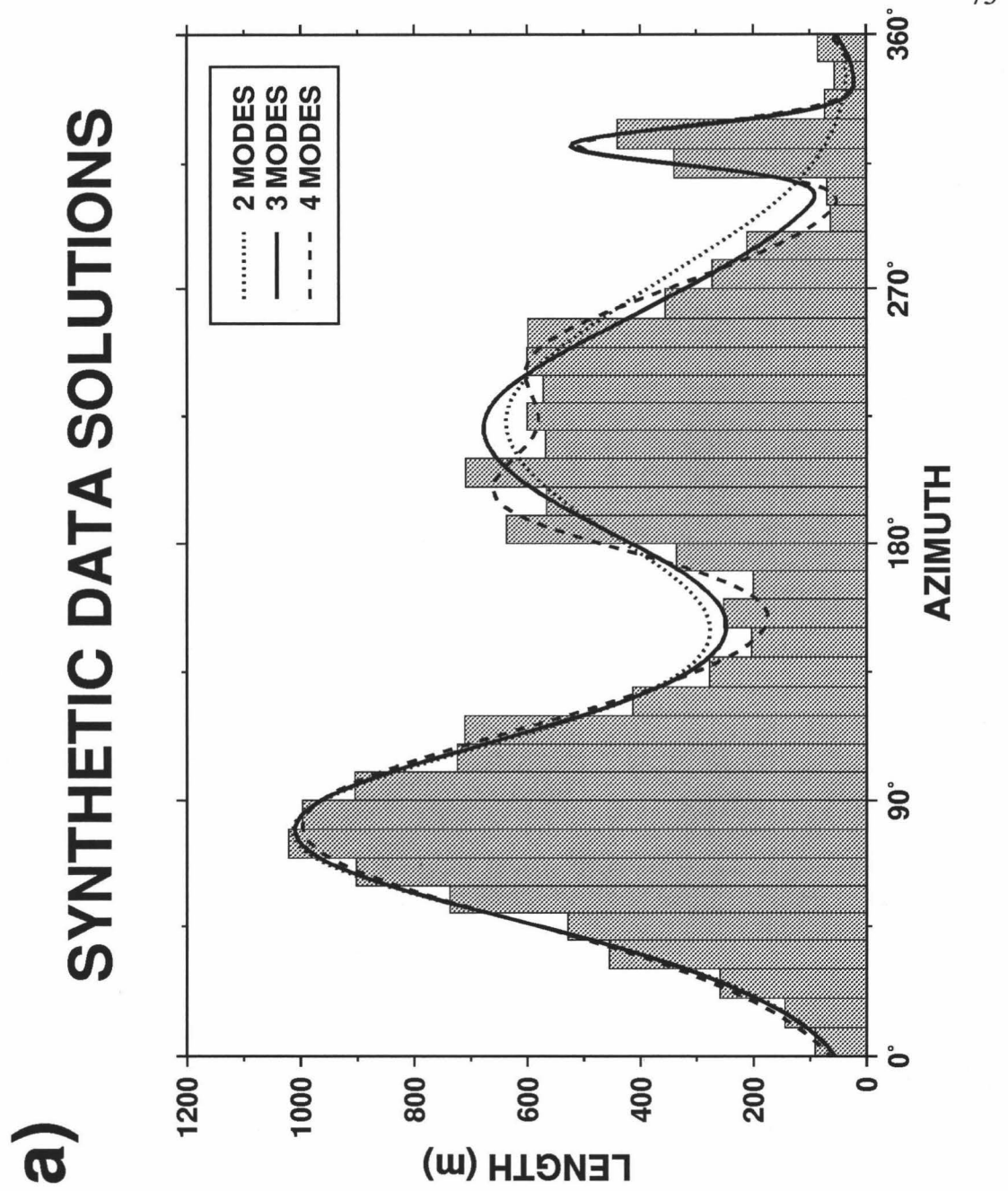

Fig. A-2a. Histogram of the synthetic data with three different solutions superimposed. The dotted line shows the two-mode solution, the solid line represents the preferred three-mode solution, whereas the dashed line illustrates the four-mode solution. Although the data was made up of four modes as resolved by the four-mode solution, it was not a significant improvement over the three-mode solution at the 95% confidence level. Table A-1 gives the numerical values for each mode.

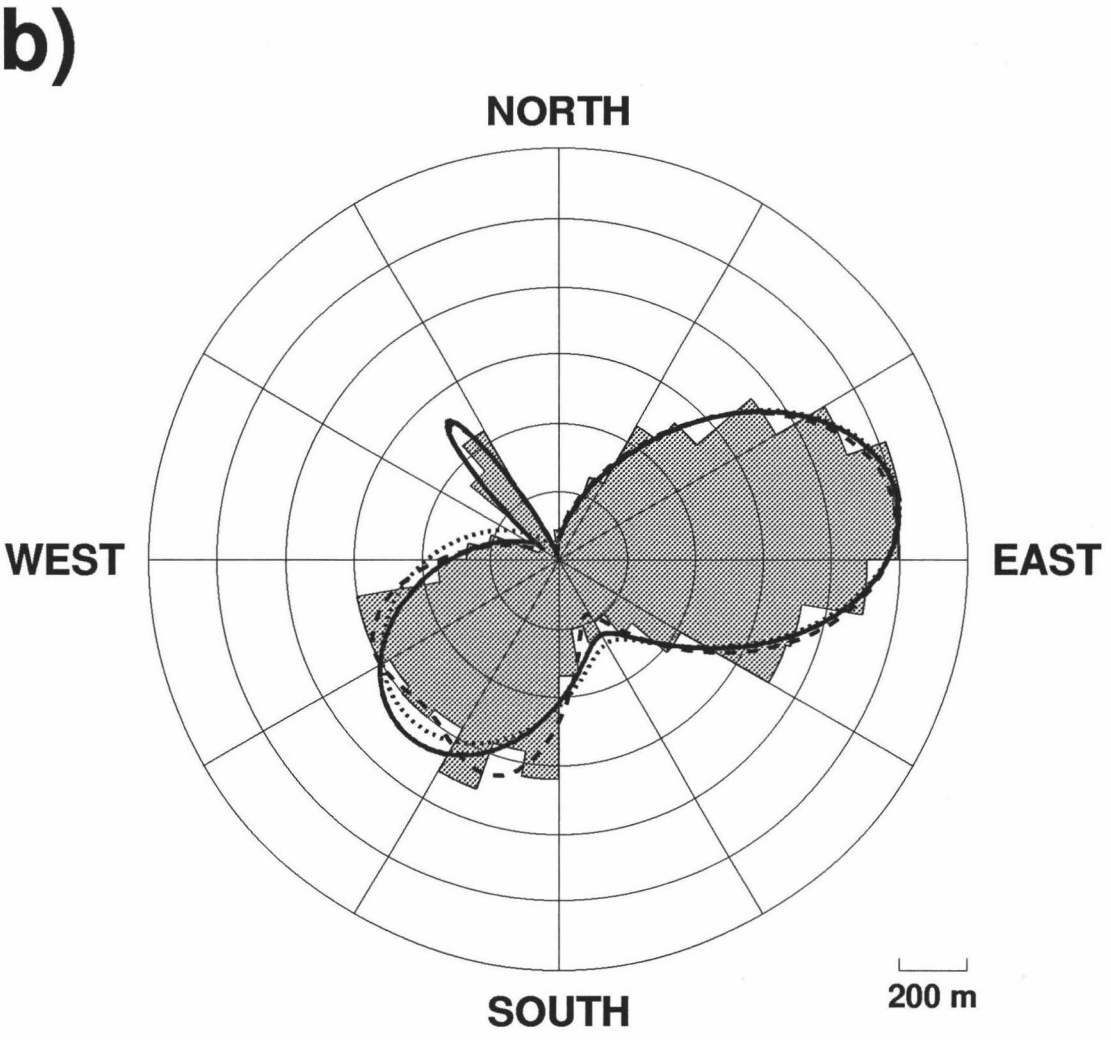

Fig. A-2b. Same as a), but plotted as a sector diagram. The radius of the sectors are proportional to the total fracture length of each bin.

Real Data Case

Figures A-3a and A-3b depict an area of the northern Mariana inner forearc where dense, high angle, normal faults were mapped using seismic reflection profiles, SeaMARC II acoustic imagery and bathymetric data [*Mahoney and Fryer*, 1988; 1989]. In order to study fault orientation and geometry as a function of strain at the time of formation, it is first essential to identify possible fault populations and their relationship to one another [*Ramsey*, 1967]. For our example we will consider a subset of the data – those faults with less than 100-m throws in the vicinity of the volcanic island arc bordered by the East Boundary Fault (the shaded region in Figure A-3b). In this region it seems obvious that these small faults are related to the slumping along the East Boundary Fault, but are they also influenced by other large structures that appear to abut, if not cross, the arc such as the major forearc faults? Since fault traces are oriented features, opposite angles for each fracture are appended to the data set making their orientation unbiased when displayed in a sector-type rose diagram (Figure A-4a). Note that the sector diagram is not areally correct which henceforth deludes the eye somewhat, but is of the form most frequently presented [*Upton and Fingleton*, 1989].

In our analysis we use a technique first considered for oriented data by *Krumbein* [1939] in which the azimuth of each lineament is doubled (Figure A-4b). This is because a fault trace may be expressed as either of two opposite directions. The doubling of the azimuth allows us to calculate, among other statistics, the parameters of each mode without any ambiguity. The result is that the principal orientation(s) of the sample will be preserved regardless of which directional sense the lineaments were recorded in. To recover the true modes, the calculated values and the associated errors are divided by 2 [*Davis*, 1986; *Krumbein*, 1939].

Measurement errors in remotely sensed data, such as this, occur in fracture location. Certainly locating one's exact position at sea over a morphological feature on the sea floor has always been difficult. These "regional" errors in fracture location, which result from errors in navigation, are more likely to shift the true location of a surveyed area rather than alter the distances between faults and skew their orientation with respect to one another. Thus, we assume that navigational errors do not significantly affect azimuth (α) or fracture length (L). The most significant source of error comes from the flat bottom assumption used in the side-scan processing [e.g., *Johnson and Helferty*, 1990]. Where the ocean

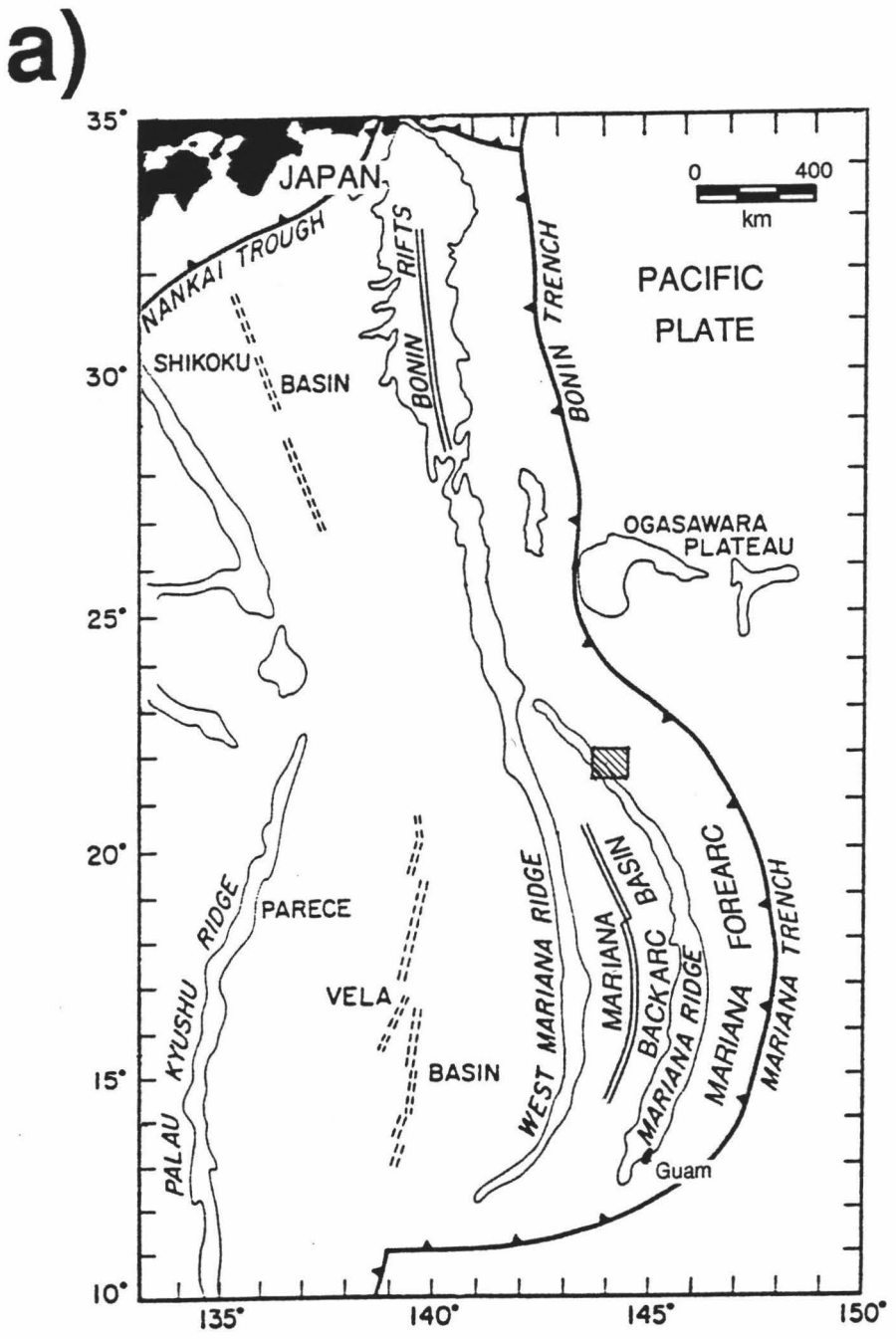

Fig. A-3a. Tectonic setting and location of the Mariana Island Arc. The shaded region in the northern part of the arc shows the location of Figure A-3b.

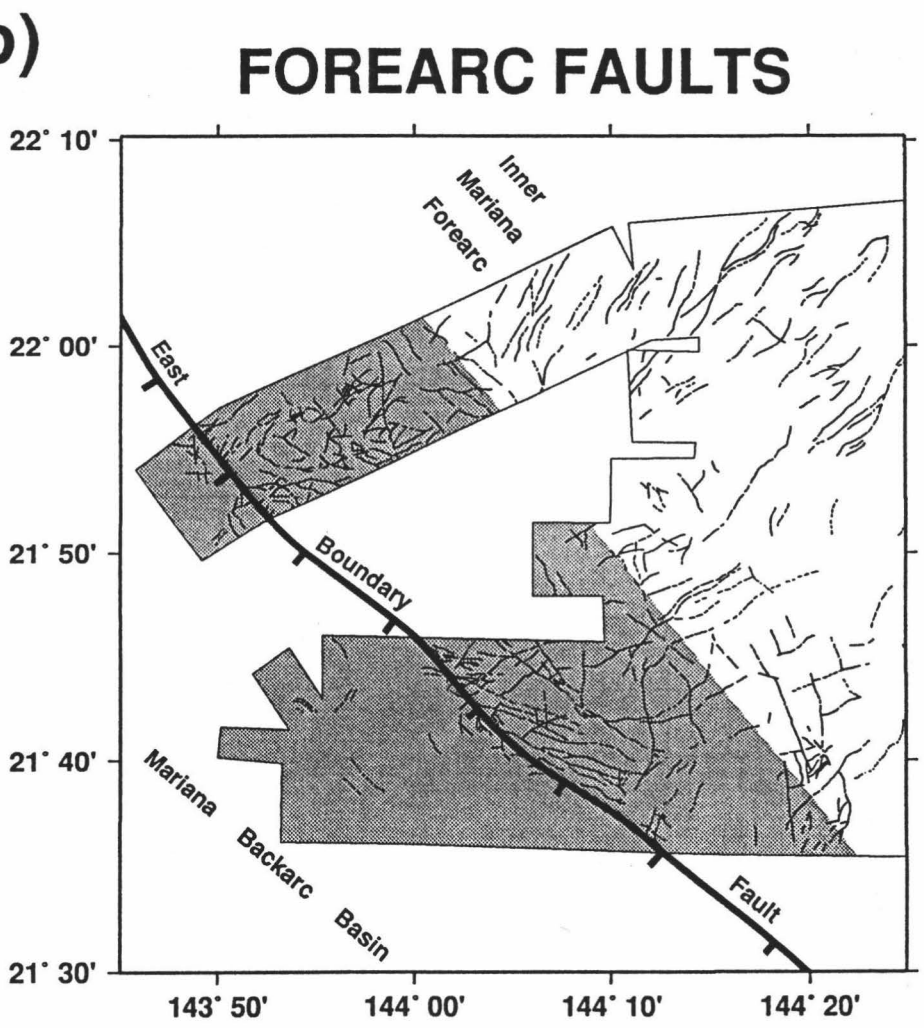

Fig. A-3b. A line drawing of faults (with less than 100m throws) mapped from various remote sensing devises. The East Boundary Fault, along which the volcanic arc trends, marks the division between the backarc basin and the forearc. The shaded region shows the subset of faults used in the statistical analysis. (Fault dip directions have been removed to avoid cluttering the map.)

a)

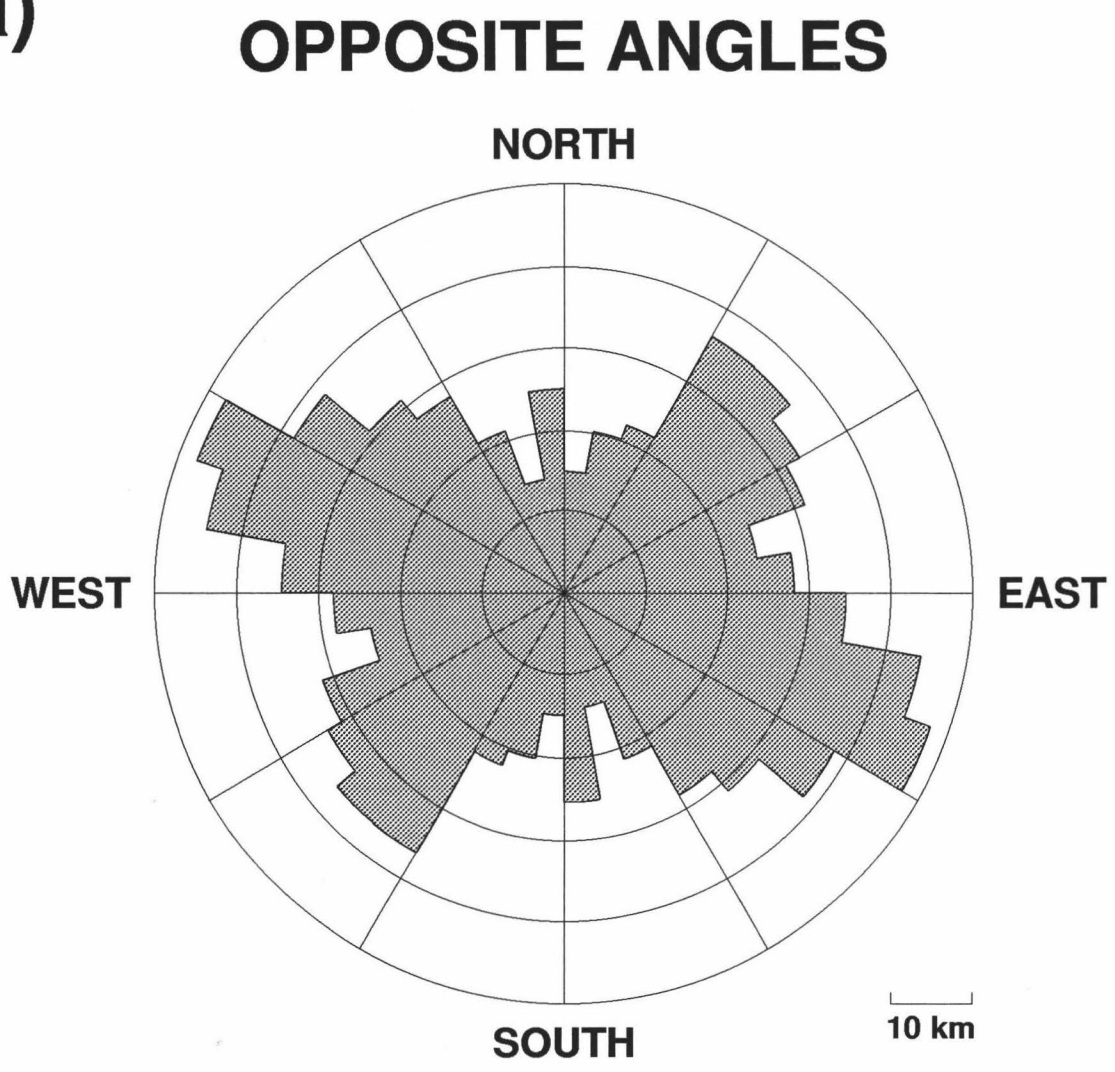

Fig. A-4a. Orientation directions of faults (from the shaded region in Figure A-3b) plotted in a sector diagram in which data has been binned in 10° sectors. A 10 km radial grid representing the fracture length is used. For each measured azimuth, its opposite is also plotted so as not to bias the data set, as fault traces are orientational, that is, double headed vectors.

b)

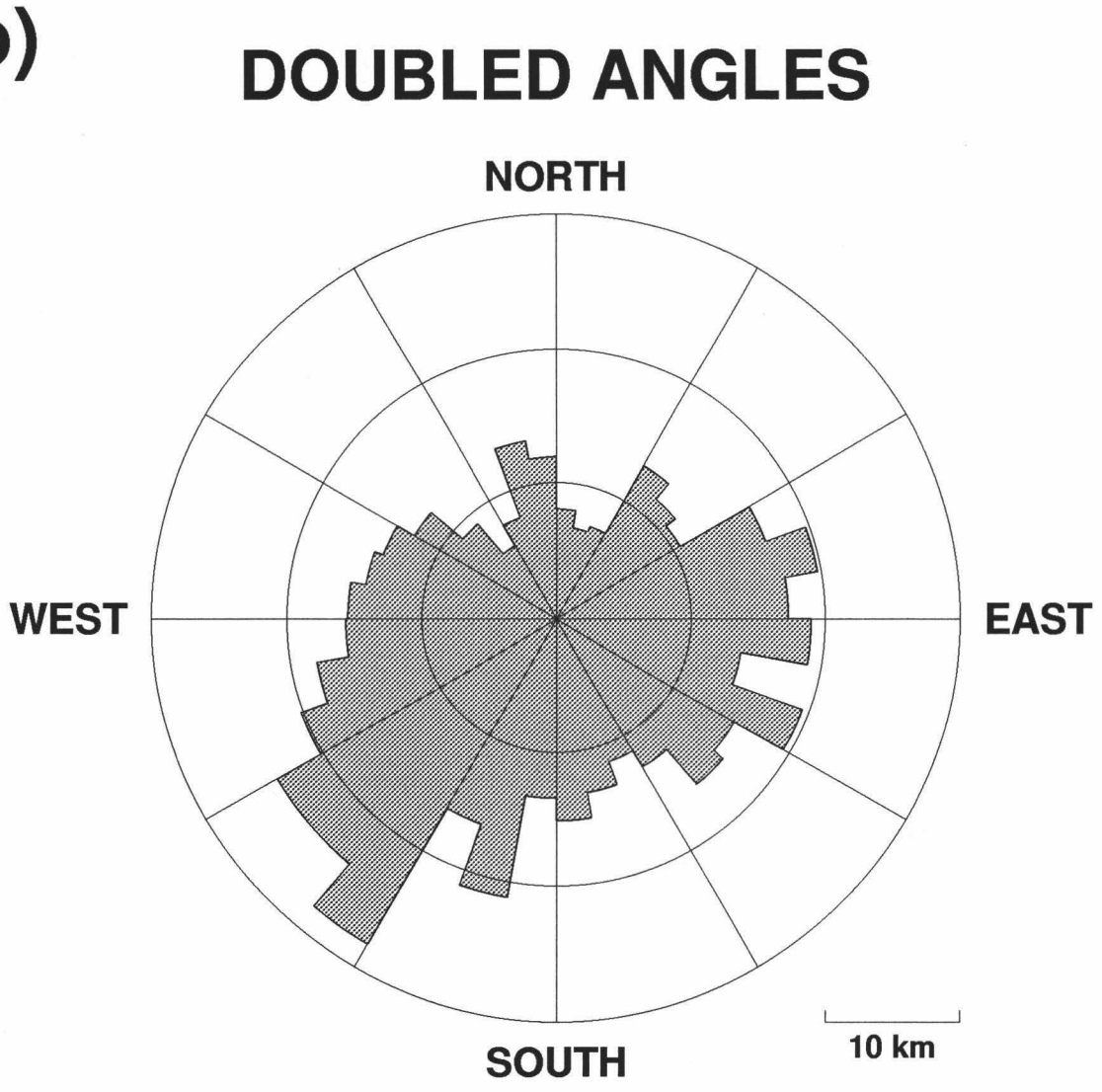

Fig. A-4b. Each azimuthal measurement from the original data has been doubled then plotted as a sector diagram, again binned in 10° sectors. For oriented data, doubled angles are required in order to uniquely calculate the parameters of each mode.

bottom is sloping, the point on the ocean floor closest to the sonar is not vertically beneath it. This produces calculated (apparent) positions that differ from the true position in a manner that depends on the slope. This uncertainty affects the fault azimuth as well as the length.

The one sigma error in location of a digitized point along a fracture, σ_P, was approximated at 50 m as a cumulative consequence of errors in interpreting location, distortion in drafting, and accuracy of digitizing. The error in azimuth, $\Delta\alpha$, depends on the distance between two digitized points; for most segments used in this study $\Delta\alpha$ is less than 10°, the bin width chosen for the data. We assume these errors in azimuth will not significantly affect the overall shape of the data set. The error in length ΔL however, has a maximum of $\sqrt{2}\,\sigma_P$ (using the standard deviation of the difference between two means). For segments with a cumulative fracture length less than $\sim 3\sigma_P$ the error in length will approach σ_P, because the fracture length between any two points defining a fault must always be positive. The total fault length for a given bin is made up of contributions from many segments of individual faults. Therefore, the error associated with each bin will depend on the number of continuous segments and the estimated error of each segment. The data, as presented in Figure A-4a, have error bars of different length, and in general, the longer the total fault length for a given bin, the larger the error.

Considering Figure A-4a, two visually apparent trends in the fault data cluster about 45° and 115° with a hint of a possible third mode at 175°, but are these trends statistically significant at, say, the 95% confidence level? The single and multiple mode models calculated for this data set using the theory described in this paper are presented in Table A-2, and graphically illustrated in Figure A-5a. We will refer to these models as solution I. The dashed line shows the first, single-mode solution with a mean direction of 191°. Although it explains most of the variance (93%) the model does not appear to fit the data very well. The solid curve, being the bimodal solution, clearly fits the data better, both visually and statistically, but because of the high noise level associated with this particular data set the improvements offered over the single mode solution are only significant at the 90% confidence level. The more elaborate three-mode solution (dotted line) further reduces the root-mean-square (rms) misfit somewhat, but is significant only at the 73% confidence level. Therefore, at a 95% confidence level only the single mode model, with a mean direction of 191°, is acceptable with additional modes being insignificant improvements. A summary of these solutions is given in Table A-3.

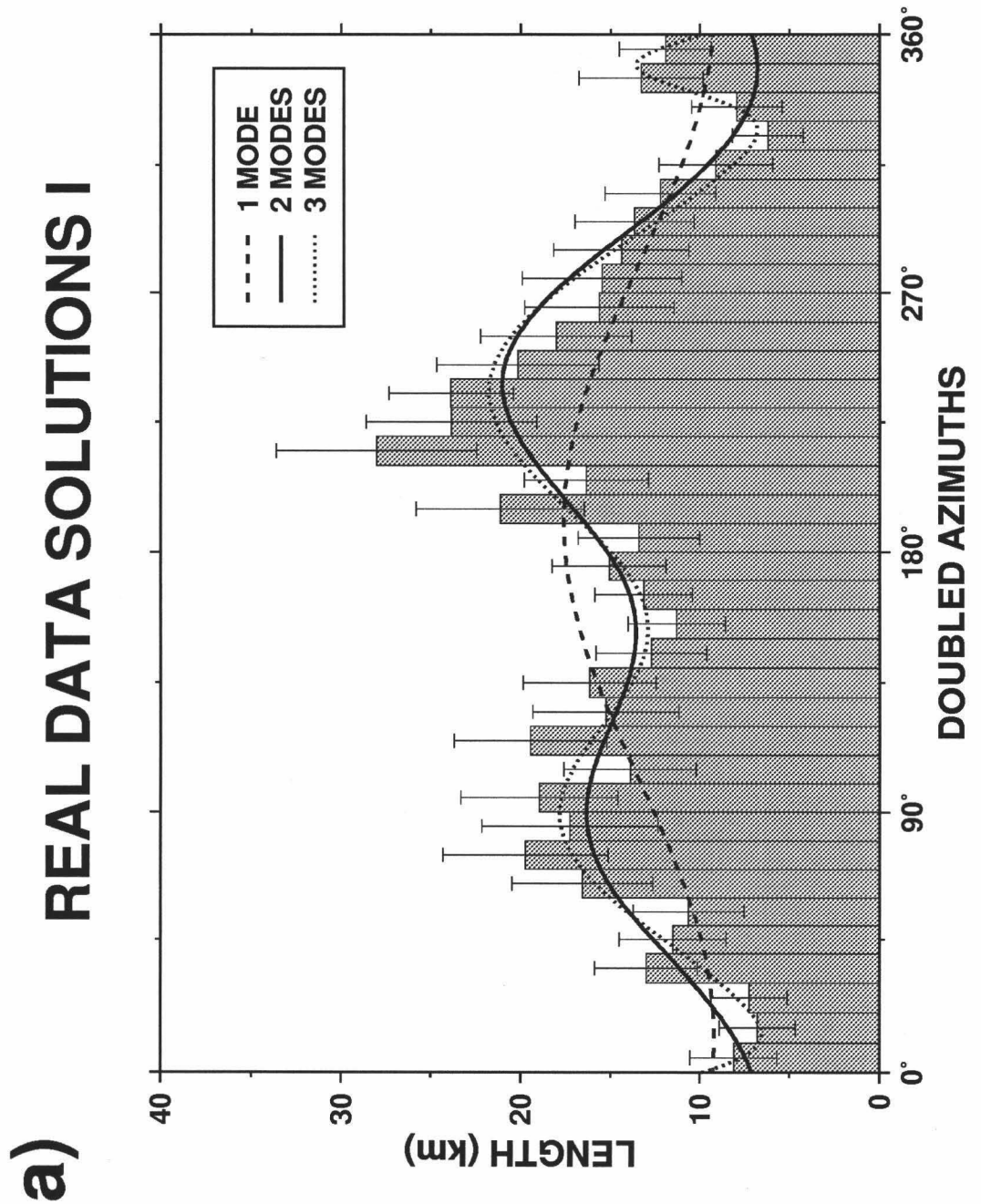

Fig. A-5a. Histogram of doubled azimuthal data (from Figure A-4b) in 10° bins showing the error in length for each set of binned faults, and three possible best fit models from solution I. The dotted line shows the three-mode solution, the solid line represents the preferred two-mode solution, whereas the dashed line illustrates the one-mode solution. At a 95% confidence level, only the single-mode model is valid, due to the amount of background noise that the the gaussian curves are trying to compensate for. Note the large discrepancies in all three models in fitting the data.

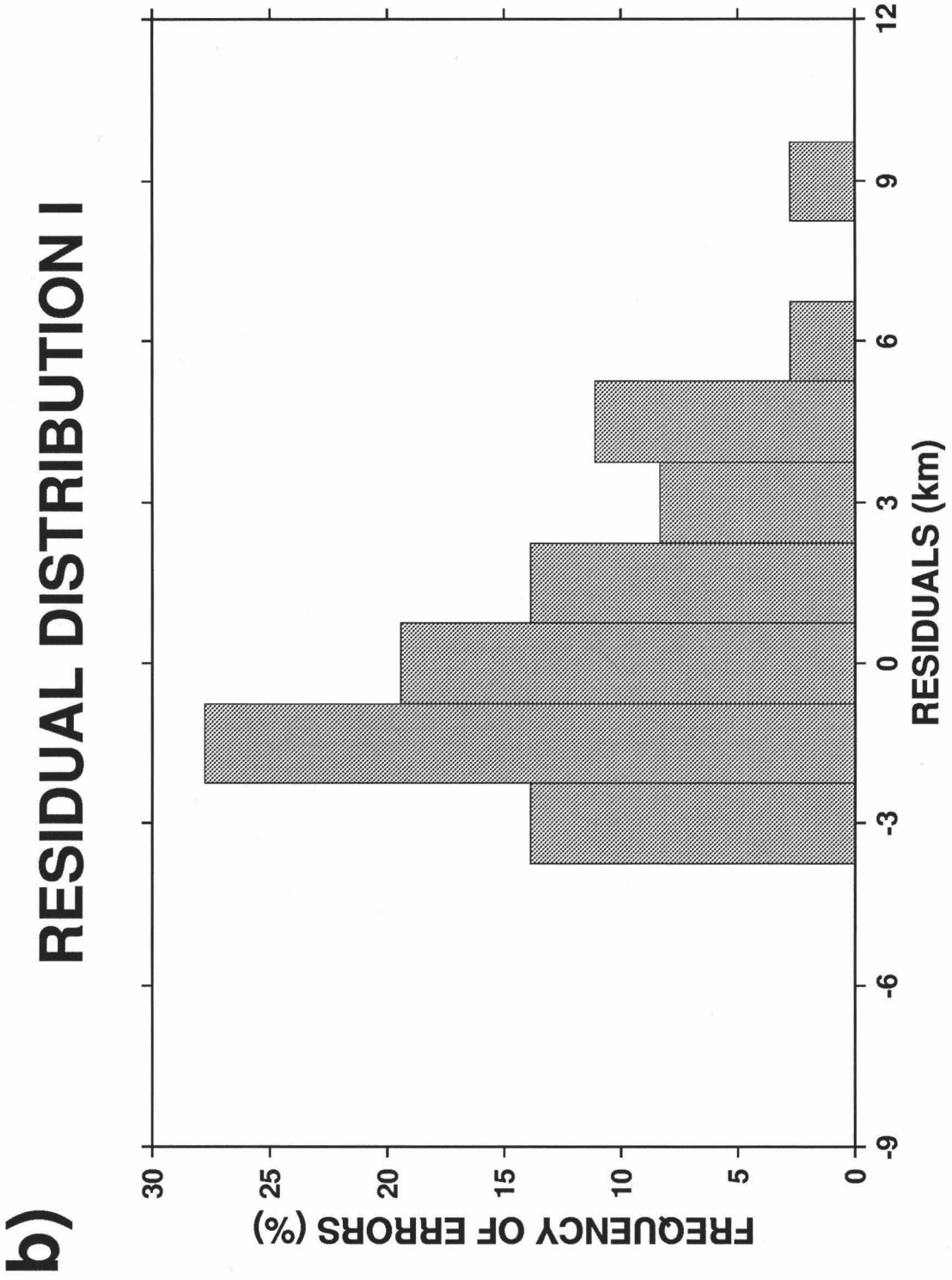

Fig. A-5b. The residuals after the two-mode model of solution I has been removed from the data set. Note the distribution is not Gaussian.

Acceptance of a model depends not only on the certainty with which one chooses to evaluate the data and the goodness of fit, but also on whether the model looks acceptable visually. Again, we emphasize that one should no more be led to a conclusion by only a visual analysis of plotted data than solely by statistical arguments. Clearly Figure A-5a shows that, visually, the single mode model does not represent the data well. The two-mode model visually and statistically fits the data better with a Q of 0.716; so with 90% certainty, we could conclude that the faults are loosely scattered about two principal directions of 85° and 241° (double azimuth). The fairly small improvement offered by the second mode suggests that there exists wide, almost random scattering among the two preferred directions – enough scattering to mask the clarity of the less dominant mode.

It was assumed that the errors in the data are normally distributed, implying that the difference between the data and the model should have a gaussian distribution about a zero mean. Figure A-5b presents a histogram of the residuals after the bimodal solution has been removed from the data. The distribution is fairly asymmetrical and strictly speaking not Gaussian. One cause of non-Gaussian residuals may be the presence of outliers in the data, which least squares methods traditionally do not handle well [e.g., *Menke*, 1984]. However, before leaping to the obvious conclusion – that the data errors themselves are not Gaussian – let us first consider that the occurrence of non-Gaussian residuals can also be created by a model that fails to describe the data well. A closer inspection of Figure A-5a reveals that the slopes of the two dominant data peaks are steeper than the best fitting gaussian curves. This suggests that the trends alluded to in the data are superimposed on an ~8 km background "noise floor". Realizing that a gaussian curve is a rather poor representation for such uniform noise, we chose to investigate this possibility by including an extra parameter to model this apparent noise level.

The solutions presented in Table A-4 and illustrated in Figure A-6a are similar to the ones just discussed, except they all include a free parameter to explain the observed background noise level. We refer to these models as solution II. Whereas in Figure A-5a the gaussian curves had to explain both the broad noise level and the localized peaks, causing the gaussians to be wider and less well resolved, the curves in Figure A-6a are narrower and overall follow the data much more closely. Here, the bimodal model is a clear improvement over the single mode, being a significant improvement at the 99.5% level. The presence of uniform noise also explains why the inclusion of the third mode in solution I seemed to be fairly significant (at the 73.7% confidence level): It contributed

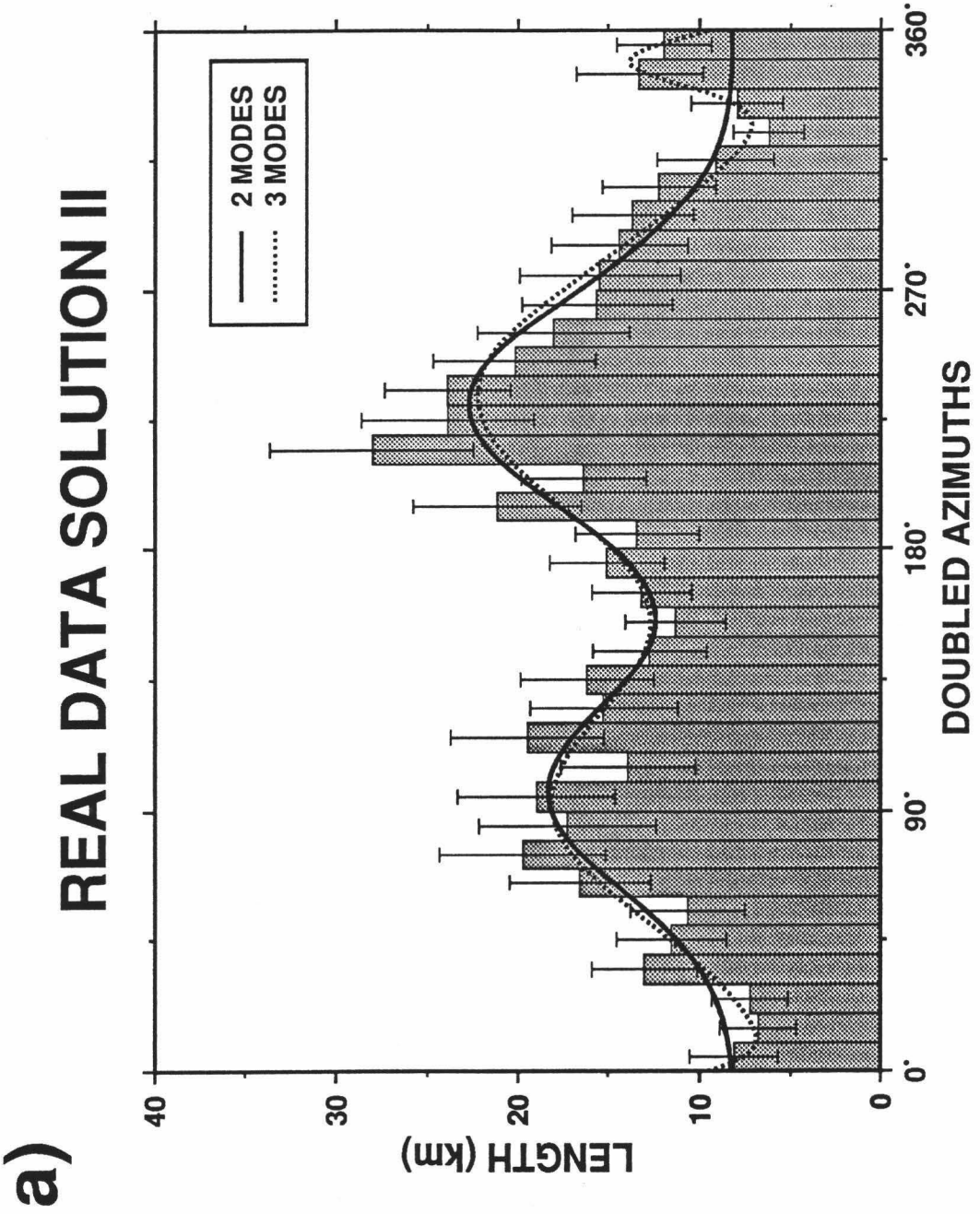

Fig. A-6a. Histogram of doubled azimuthal data (from Figure A-4b) in 10° bins showing the error in length for each set of binned faults, and two possible best fit models from solution II accounting for uniform background noise. Although the two-mode model is visually almost the same as in solution I, statistically the goodness-of-fit and level of significance are much higher with the second mode being a vastly significant improvement over one-mode. The remaining scatter in the data unmatched by the two-mode model is attributed to random noise.

more towards modelling the large noise level than the possible peak it was intended for. With most of the uniform noise explained by the noise level parameter, the third mode of solution II clearly becomes an insignificant improvement (significant only at the 35.4% level). Perhaps the best evidence for our theory that the data are better explained as two peaks of gaussian shape superimposed on a uniform floor of background noise is that the residuals between the data and the bimodal solution II follow a nearly perfect gaussian distribution (Figure A-6b).

Even though the difference between the two-mode models from solutions I and II is very slight, the improvement from a single-mode to a two-mode model is very significant, once uniform background noise is statistically taken into account. Using the F-test we find that solution II's bimodal model is a meaningful improvement over the single mode model from solution I in Table A-2, at a 98.3% confidence level. Thus, at the 95% confidence level, we conclude that the faults with throws of less than 100 meters do, in fact, cluster about two dominant directions of 48° and 115° (true azimuth), as illustrated in Figure A-7. The latter trend is comprised of sub-parallel, small, slump faults on the face of the 2 km high East Boundary Fault of the backarc basin. The less dominant directional trend centered about 48°, corresponds roughly to the direction of rifting further east in the inner forearc [*Mahoney and Fryer*, 1988; 1989]. A high level of uniform background noise accounts for approximately 8 km of fractures in all directions which obscures the dominant fault trends (see Table A-3). In this region, a geologic cause for such uniform noise could be attributed to the alleviation of small stresses within the rigid blocks bounded by the two interfering sets of major faults after movement along these faults (Figures A-3b and A-6a). In addition, some random noise contributes to the large error bars which ultimately make the visually apparent third mode in Figures A-5a and A-6a insignificant.

DISCUSSION

The preceding section has demonstrated the usefulness of knowing confidence limits and significance of the accepted solution. With unbiased estimates of the principal directions one can more confidently make geological interpretations of the data at hand. When the data are somewhat obscure and a choice has to be made between competing models, the test for significance will allow the scientist to select the most probable solution and state the confidence level at which the decision was made.

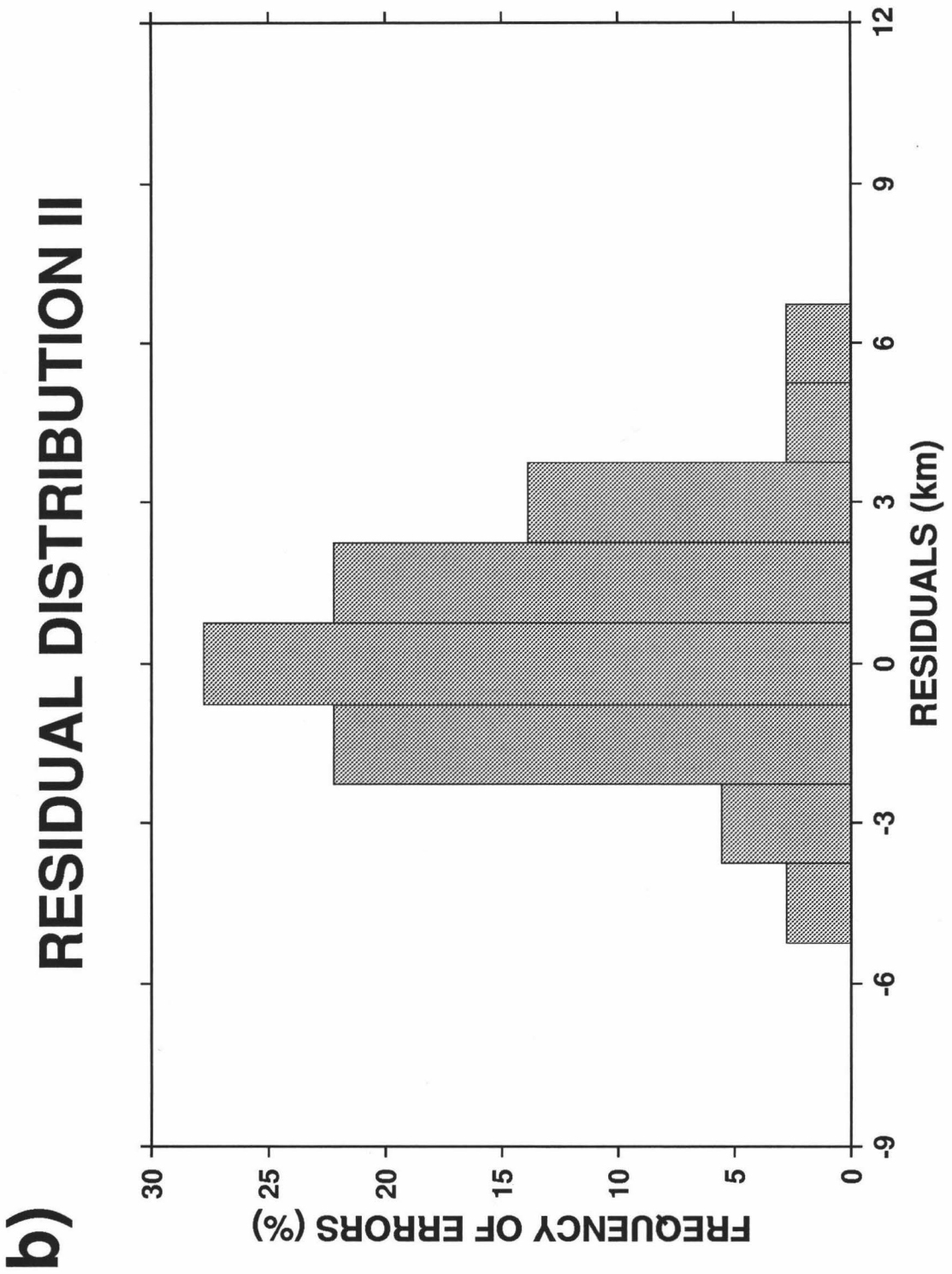

Fig. A-6b. The residuals after the two-mode model of solution II (accounting for uniform background noise) has been removed from the data set. Note the distribution is now fairly Gaussian.

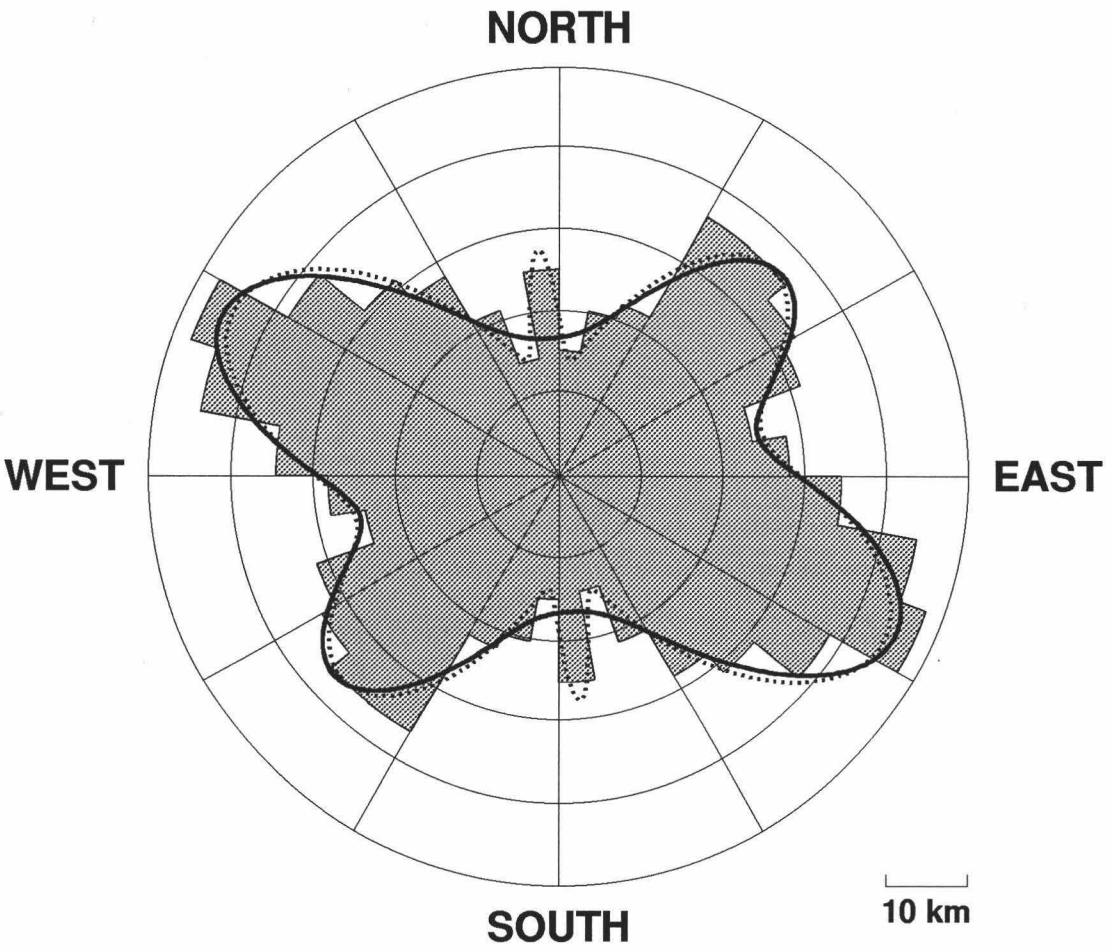

Fig. A-7. The two- and three-mode models from solution II (in which the modes and corresponding widths have been divided by two) superimposed on the undoubled, opposite angle data set.

Based on the cases examined in this paper, it is clear that it is of major importance to have a good knowledge of the magnitude of the errors associated with the data. The goodness-of-fit parameter Q will depend strongly on the error level. If the errors are over-estimated, one can expect to obtain high values for Q for most reasonable models, but also find that most of those models are not significantly different. If the errors are under-estimated, only a near perfect fit will give high values for Q. On the other hand, the models are more likely to be significantly different than in the case with over-estimated errors. We therefore strongly suggest that the nature and magnitude of the data errors be carefully assessed before the curve-fitting scheme is employed. If no reliable *a priori* estimates for the error are readily available, we follow *Press et al.* [1986] and recommend the following course of action: (1) Assign an arbitrary constant σ to represent the errors, (2) solve for the best solution as outlined above, (3) compute the rms error, (4) use the rms error to recompute the best-fitting solution. Note, however, that this method makes an independent assessment of the goodness-of-fit impossible, but at least it provides reasonable error bars in a situation where the noise level is unknown.

The test for significance can also be used to compare a model determined by the method outlined in this paper to another solution based on other criteria. For example, one may have independent knowledge of what the principal directions should be in a certain tectonic environment, or simply want to test if the determined solution is significantly different from another region or from predictions by numerical modelling of lithospheric deformation.

In many situations the processes that create fractures and lineaments are time-dependent in that the direction of forces responsible for the rifting are slowly varying with time. Although the scattering about a principal direction for a given time period may be assumed to be Gaussian, the superimposed lineaments observed today would have non-Gaussian errors due to the change in rifting direction over time. In such cases one may choose to divide the area into smaller regions where the direction of rifting has been nearly constant and solve for principal directions within each region. With the errors for each region being more or less normally distributed, the method presented in this paper may directly be applied.

The curve-fitting technique is, of course, not limited to circular data. By allowing for non-periodic data with a regional trend, it is possible to determine multiple modes in other types of data, e.g., power spectra estimates. Furthermore, it would be relatively easy to extend the method to three dimensions, making it possible to solve for the principal directions in vector data like magnetization and fold axes.

Although geoscientists have worked with directional measurements and plotted them in various diagrams for years, rigorous statistical techniques to test the significance and veracity of conclusions drawn from those diagrams have not been extensively applied. In this paper, we have shown that, in most cases, one can address these important issues with the aid of an unbiased, least-squares curve-fitting formalism.

Table A-1a. Synthetic data one-mode solution

Mode	μ_j	h_j	w_j
1	123.8±3.4	640.7±15.1	598.0±12.4

Table A-1b. Synthetic data two-mode solution

Mode	μ_j	h_j	w_j
1	78.9±1.0	1008.7±25.8	191.9± 6.6
2	223.1±2.0	637.2±21.8	282.9±13.2

Table A-1c. Synthetic data three-mode solution

Mode	μ_j	h_j	w_j
1	79.8±1.0	1008.9±25.6	197.3± 6.5
2	220.9±1.7	677.8±23.6	242.0±11.2
3	321.4±0.9	490.6±78.9	37.6± 7.8

Table A-1d. Synthetic data four-mode solution

Mode	μ_j	h_j	w_j
1	81.1±1.0	997.2±25.1	208.2± 6.4
2	194.2±4.3	567.7±90.4	115.6±17.4
3	245.0±5.9	581.2±46.3	149.9±24.9
4	321.3±0.9	500.3±65.6	41.0± 6.9

Table A-2. Summary of synthetic solution models

Solution	Variance reduction	rms	Q	Significance
1–mode	79.1 %	239.4 m	10^{-152}	100.0 %
2–modes	96.4 %	99.7 m	10^{-16}	100.0 %
3–modes	98.8 %	57.9 m	0.007	98.8 %
4–modes	99.4 %	42.3 m	0.363	78.8 %

Table A-3a. Solution I one-mode model

Mode	$2\mu_j$	h_j	$2w_j$	μ_j	w_j
1	190.9±10.8	17.43±1.01	661.8±28.0	95.5±5.4	330.9±14.0

Table A-3b. Solution I two-mode model

Mode	$2\mu_j$	h_j	$2w_j$	μ_j	w_j
1	85.3±13.5	15.86±1.53	339.1±104.9	42.6±6.7	169.6±52.4
2	241.0±10.4	20.65±1.62	332.6± 79.4	120.5±5.2	166.3±39.7

Table A-3c. Solution I three-mode model

Mode	$2\mu_j$	h_j	$2w_j$	μ_j	w_j
1	85.8±7.8	17.26±1.69	279.2±54.0	42.9±3.9	139.6±27.0
2	236.7±7.1	21.69±1.59	330.2±50.4	118.3±3.6	165.1±25.3
3	349.8±3.2	8.90±2.69	57.0±19.5	174.9±1.6	28.5± 9.8

Table A-4. Summary of solution I models

Solution	Variance reduction	rms	Q	Significance
1–mode	93.0 %	4.12 km	0.026	100.0 %
2–modes	96.7 %	2.85 km	0.716	91.1 %
3–modes	97.9 %	2.28 km	0.989	73.7 %

Table A-5a. Solution II one-mode model with background noise

Mode	$2\mu_j$	h_j	$2w_j$	μ_j	w_j
1	218.0±18.8	4.40±1.59	357.3±188.0	109.0±9.4	178.7±94.0
–	–	10.53±1.25	–	–	–

Table A-5b. Solution II two-mode model with background noise

Mode	$2\mu_j$	h_j	$2w_j$	μ_j	w_j
1	96.3± 7.4	10.23±2.13	201.1±46.6	48.1±3.7	100.6±23.3
2	230.3± 5.7	14.63±2.04	229.4±38.2	115.2±2.9	114.7±19.1
–	–	8.07±1.18	–	–	–

Table A-5c. Solution II three-mode model with background noise

Mode	$2\mu_j$	h_j	$2w_j$	μ_j	w_j
1	91.1±8.9	13.47±3.96	244.0±64.2	45.6±4.5	122.0±32.1
2	233.6±7.1	17.72±4.08	279.4±61.8	116.8±3.5	139.7±30.9
3	349.4±3.2	7.95±3.19	50.1±25.2	174.7±1.6	87.4±12.6
–	–	4.48±4.21	–	–	–

Table A-6. Summary of solution II models with background noise

Solution	Variance reduction	rms	Q	Significance
1–mode	90.3 %	4.86 km	0.001	68.81 %
2–modes	97.6 %	2.39 km	0.911	99.9 %
3–modes	98.0 %	2.19 km	0.987	33.4 %

REFERENCES

Boccaletti, M., G. Cello, and L. Tortorici, Transtensional tectonics in the Sicily channel, *J. Struct. Geol., 9,* 869–876, 1987.

Cello, G., G. M. Crisci, S. Marabini, and L. Tortocici, Transtensive tectonics in the strait of Sicily: structural and volcanological evidence from the island of Pantelleria, *Tectonics, 4,* 311–322, 1985.

Compton, R. R., *Geology in the field,* 398 pp., John Wiley & Sons, New York, 1985.

Curray, J. R., The analysis of two-dimensional orientation data, *Jour. Geology, 64,* 117–131, 1956.

Davis, J. C., *Statistics and data analysis in geology*, 2 edition, 646 pp., John Wiley & Sons, New York, 1986.

Greiner, G., In-situ stress measurements in southwest Germany, *29,* 265-274, 1975.

Johnson, H. P., and M. Helferty, The geological interpretation of side-scan sonar, *Rev. Geophys., 28,* 357–380, 1990.

Jones, T. A., Statistical analysis of orientation data, *Jour. Sed. Pet., 38,* 61–67, 1968.

Jones, T. A., and W. R. James, Analysis of bimodal orientation data, *Math. Geol., 1,* 129–135, 1969.

Kelsey, H. M., and S. M. Cahsman, Wrench faulting in northern California and its tectonic implication, *Tectonics, 2,* 565–576, 1983.

Kernighan, B. W., and D. M. Ritchie, *The C programming language*, pp., Prentice-Hall, Englewood Cliffs, New Jersey, 1978.

Kleinrock, M. C., and R. N. Hey, Migrating transform zone and lithospheric transfer at the Galapagos 95.5 °W propagator, *J. Geophys. Res., 94,* 13,859–13,878, 1989.

Krumbein, W. C., Prefered orientation of pebbles in sedimentary deposits, *Jour. Geology, 47,* 673-706, 1939.

Lamb, S. H., and H. M. Libby, The last 25 Ma of rotational deformation in part of the New Zealand plate-boundary zone, *J. Struct. Geol., 11,* 473–492, 1989.

Lespinasse, M., and A. Pêcher, Microfracturing and regional stress field: a study of the preferred orientations of fluid-inclusion planes in a granite from the Massif Central, France, *J. Struct. Geol., 8,* 169–180, 1986.

Macdonald, K. C., D. A. Castillo, S. P. Miller, P. J. Fox, K. A. Kastens, and E. Bonatti, Deep tow studies of the Vema fracture zone 1. Tectonics of a major slow slipping transform fault and its intersection with the Mid-Atlantic ridge, *J. Geophys. Res., 91,* 3334–3354, 1986.

Mahoney, J. K., and P. Fryer, Stress field re-orientation of the inner Mariana Forearc at 22°N, *EOS, 69,* 1443, 1988.

Mahoney, J. K., and P. Fryer, Rifting and associated volcanism of the inner Mariana forearc at 22°N, *EOS, 70,* 1319, 1989.

Mardia, K. V., *Statistics of directional data*, 357 pp., Academic Press, Inc., New York, 1972.

Menke, W., *Geophysical data analysis: Discrete inverse theory*, 260 pp., Academic Press, Orlando, Florida, 1984.

Pincus, H. J., The analysis of aggregates of orientation of pebbles in sedimentary deposits, *Jour. Geology, 61,* 482–509, 1953.

Pincus, H. J., Some vector and arithmetic operations on two-dimensional orientation variates with applications to geologic data, *Jour. Geology, 64,* 533–557, 1956.

Press, W. H., B. P. Flannery, S. A. Teukolsky, and W. T. Vetterling, *Numerical recipes*, 818 pp., Cambridge Univ. Press, New York, 1986.

Ramsey, J. G., *Folding and fracturing of rocks*, pp., McGraw-Hill, New York, 1967.

Rathore, J. S., and A. M. Kafafy, A magnetic facric study of the Sharp region in the English Lake district, *J. Struct. Geol., 8,* 69–77, 1986.

Steinmetz, R., Analysis of vectorial data, *Jour. Sed. Pet., 32,* 801–812, 1962.

Upton, G. J. G., and B. Fingleton, *Spatial data analysis by example: catagorical and directional data*, Probability and mathematical statistics, vol. 2, 416 pp., John Wiley & Sons, Chichester, 1989.

APPENDIX B

The following program was written and used for determining the azimuths and corresponding lengths of sinuous lineaments and faults in the thesis study area. This method involves digitizing points along a lineament or fault trace in which the segment between any two points can be approximated as a straight line. Next, based on the inverse Transverse Mercator projection, the actual length of each segment is calculated. This enables weighting of the lineaments and fractures. In essence, each lineament or fault trace is comprised of a series of straight line segments, each having a unique azimuth and corresponding length (or weight), rather than an average. This allows for a more detailed and accurate analysis of preferred orientation and strain.

```
ccccccccccccccccccccccccccccccccccccccccccccccccccccccccccccccccccccccccc
c                                                                       c
c   This program calculates azimuth per unit length of lineaments      c
c   (based on the shortest segment) given points of latitude and        c
c   longitude along their linear segments.                              c
c   ------------------------------------------------------------        c
c   Written by Jill Mahoney (Wessel).............September 1988        c
c   Modified & Debugged by JKM (Wessel)...........1989/1990             c
c                                                                       c
c=======================================================================c
c    INPUT/OUTPUT:                                                      c
c    Enter & Open I/O files in a shellscript.  Input file (8) needs     c
c    to be in the form of "file.out.trax" output generated from         c
c    program (T)UNMERC, which consists of a flag (1 indicates the       c
c    beginning of a lineament), latitude, and longitude.                c
c    Set environment for 2 output files (9,10):                         c
c      "filename.az"--a listing of all values (lin#,seg#,lat1,lon1,     c
c                lat2,lon2,az,len);                                     c
c      "filename.az.rose"--computational values (az, length).           c
c-----------------------------------------------------------------------c
c    This program will run on either a Sun or the Alliant, however      c
c    the shellscripts are different.                                    c
c      SHELLSCRIPT to run on ALLIANT:                                   c
c        setenv FOR008 file.out.trax                                    c
c        setenv FOR009 file.az                                          c
c        setenv FOR010 file.az.rose                                     c
c        aazfar                                                         c
c      SHELLSCRIPT to run on SUN:                                       c
c        ln -s file.out.trax fort.8                                     c
c        ln -s file.az fort.9                                           c
c        ln -s file.az.rose fort.10                                     c
c        azfar                                                          c
c-----------------------------------------------------------------------c
```

```
c   *COMMENTS:                                                          c
c    This program is presently set up to interface its file.az.rose    c
c    output file with GMT-SYSTEM program "psrose".  The output file    c
c    is in the form: azimuth(degrees), weight(# of unit lengths of     c
c    each azimuth segment {where "unit length" is the shortest linear  c
c    segment of the data set}).                                        c
ccccccccccccccccccccccccccccccccccccccccccccccccccccccccccccccccccccccc
c*********************************************************************
c  Dimension statements:
c*********************************************************************
      PARAMETER (N = 15000)
      integer flag(N), lin(N), seg(N)
      real lat(N), lon(N), dist(N), wt(N), az(N)
      real lat1, lat2, lon1, lon2
      integer lcount, npoint, numseg, pts
c*********************************************************************
c  Read arguments:
c*********************************************************************
      read (8,*)pts
30    format(i4)
      npoint = 1
      read(8,10,end=21) flag(npoint), lat(npoint), lon(npoint)
20    read(8,10,end=21) flag(npoint), lat(npoint), lon(npoint)
      npoint = npoint + 1
      goto 20
21    continue
10    format (4x, i1, 6x, f9.5, 5x, f10.5)
      if (npoint.eq.1) then
         print*,'no points read, aborting program'
         stop
      end if
c*********************************************************************
c  Initialize
c*********************************************************************
      do 40 i=1, npoint-1
        dist(i)=0
        az(i)=0
c        wt(i)=0
40    continue
c*********************************************************************
c  Main Loop:
c*********************************************************************
      lcount=1
      numseg=0
      do 50 i=1, npoint-1
        if (flag(i) .eq. 1) then
          lcount = lcount + 1
        else
          if (flag(i+1) .ne. 1) then
            numseg=numseg+1
            lat1 = lat(i)
            lat2 = lat(i+1)
            lon1 = lon(i)
            lon2 = lon(i+1)
            lin(i) = lcount
```

```
            seg(i) = numseg
            dist(i) = distance (lat1, lat2, lon1, lon2, az(i))
          endif
        endif
50    continue
c**************************************************************************
c  Finds the shortest segment (distance in km between 2 points).  Let
c  this distance = the unit distance by which all the other line
c  segments are weighted.
c**************************************************************************
      u = dist(1)
      do 70 i=2, npoint-1
        if (dist(i) .ne. 0.0) then
          u = amin1(u,dist(i))
        endif
70    continue
      if (u.eq.0.0) then
         print*,'u = 0.0, I can not continue.'
         stop
      end if
c**************************************************************************
c  Divides each line segment into number of unit distances (weight)
c  --normalizes length.
c**************************************************************************
c      do 80 i=1, npoint-1
c         if (dist(i) .ne. 0.0) then
c           wt(i) = dist(i)/u
c         endif
c80    continue
c**************************************************************************
c  Write Headers to output file:
c**************************************************************************
      write (9,110) u
      write (9,120)
c**************************************************************************
c  Write Arrays to output files:
c**************************************************************************
      do 90 i=1, npoint-1
        write (9,140) lin(i), seg(i), lat(i), lon(i), lat(i+1),
     +  lon(i+1), az(i), dist(i)*1000.0
90    continue
      do 100 i=1, npoint-1
c   *1000 converts dist in km to meters
          if (seg(i) .ne. 0) write (10,150) az(i), dist(i)*1000.0
100   continue
c**************************************************************************
c  Format statements for writing output files:
c**************************************************************************
c110   format ('unit length (km) = ',e11.2)
110   format ('min. length (km) = ',e11.2)
120   format (' LINE#',2x,'SEG#',5x,'LAT 1',7x,'LON 1',8x,'LAT 2',
     + 7x,'LON 2',3x,'AZIMUTH(deg)',3x,'LENGTH(m)')
140   format (1x,i4,2x,i4,4x,f9.5,2x,f10.5,4x,f9.5,2x,f10.5,4x,f5.1,6x,
     + f9.2)
150   format (1x,f5.1,4x,f12.2)
```

```
c**********************************************************************
      stop
      end

c======================================================================c
c  External FUNCTION subprogram:  distance                             c
c----------------------------------------------------------------------c
c  Converts lat/lon into distance in km for Transverse Mercator        c
c  projections; then calculates the distance between 2 points of a     c
c  line segment.                                                       c
c----------------------------------------------------------------------c
c     Input arguments:                                                 c
c       lat1 = real value of the initial latitude (in minutes) for     c
c              each line segment between 2 points.                     c
c       lat1, lat2 = latitude expressed as minutes from the equator    c
c       lon1, lon2 = longitude expressed as minutes from the meridian  c
c     Output arguments:                                                c
c       lac = # of km for a degree of latitude                         c
c       loc = # of km for a degree of longitude                        c
c     Output function value:                                           c
c       distance = distance in km between 2 points                     c
c----------------------------------------------------------------------c
c  Equations below are part of a series which use the World System     c
c  Ellipsoid of 1972.  From Bowditch, 1981, American Practical         c
c  Navigator, vII(9), p5.                                              c
c----------------------------------------------------------------------c
      function distance (lat1, lat2, lon1, lon2, azimuth)
      real d, ac, oc, lac, loc, r, lat1, lon1, lat2, lon2, azimuth
      data r /.1745329e-1/
      d = lat1
      ac=111132.92-559.82*cos(2*d*r)+1.175*cos(4*d*r)-0.0023*cos(6*d*r)
      oc=111412.84*cos(d*r)-93.5*cos(3*d*r)+0.118*cos(5*d*r)
      lac = ac/1000.
      loc = oc/1000.
      xkm = (lon2-lon1) * loc
      ykm = (lat2-lat1) * lac
      distance = sqrt((xkm**2) + (ykm**2))
      azimuth = atan2 (xkm, ykm) / r
      if (azimuth .lt. 0.0) azimuth = azimuth + 360.0
      return
      end
c======================================================================
```

REFERENCES

Anderson, E. M., *The dynamics of faulting*, 183 pp., Oliver & Boyd, London, 1951.

Beal, K. L., *The opening of a back-arc basin: northern Mariana Trough*, M.S., University of Hawaii, 56 pp., 1987.

Belderson, R. H., N. H. Kenyon, and A. H. Stride, Comparison between narrow-beam and conventional echo-soundings from the Mediterranean Ridge, *Mar. Geol., 12,* M11–M15, 1972.

Buck, W. R., Modes of continental lithospheric extension, *J. Geophys. Res.,* submitted, 1990.

Carlson, R. L., and P. J. Melia, Subduction hinge migration, in *Geodynamics of back-arc regions*, vol. 102, edited by R. L. Carlson and K. Kobayashi, 399–411, Tectonophysics, 1984.

Carlson, R. L., and C. A. Mortera–Gutierrez, Subduction hinge migration along the Izu-Bonin-Mariana Arc, *Tectonophys., 181,* 331–344, 1990.

Cas, R. A. F., and J. V. Wright, *Volcanic Successions*, 528 pp., Allen & Unwin Ltd., London, 1987.

Cashman, S. M., and H. M. Kelsey, Forearc uplift and extension, southern Hawke's Bay, New Zealand: mid-Pleistocene to Present, *Tectonics, 9,* 23–44, 1990.

Chase, C. G., Extension behind island arcs and motions relative to hot spots, *J. Geophys. Res., 83,* 5385–5387, 1978.

Chorowicz, J., J. L. Fournier, and G. Vidal, A model for rift development in Eastern Africa, *Geologic J., 22,* 495–513, 1987.

Cloud, P. E., R. G. Schmidt, and H. W. Burke, Geology of Saipan, Mariana Islands; part 1, general geology, *U.S. Geol. Surv. Prof. Paper 280-A,* 126 pp., 1956.

Cochran, J. R., and F. Martinez, Evidence from the northern Red Sea on the transition from continental to oceanic rifting, *Tectonophys., 153,* 25–53, 1988.

Damuth, J. E., Echo character of the western equatorial Atlantic floor and its relationship to the dispersal and distribution of terrigenous sediments, *Mar. Geol., 18,* 17–45, 1975.

Damuth, J. E., Use of high-frequency (3.5–12 kHz) echograms in the study of near-bottom sedimentation processes in the deep-sea: A review, *Mar. Geol., 38,* 51–75, 1980.

Davis, J. C., *Statistics and data analysis in geology*, 2 edition, 646 pp., John Wiley & Sons, New York, 1986.

Dewey, J. F., Episodicity, sequence and style at convergent plate boundaries, in *The continental crust and its mineral deposits*, Spec. Pap., vol. 20, edited by D. W. Strangway, 553–573, Geol. Assoc. Can., 1980.

Eguchi, T., Seisomtectonics around the Mariana Trough, *Tectonophysics, 102,* 33–52, 1984.

Freund, R., and M. Merzer, The formation of rift valleys and their zigzag fault patterns, *Geol. Mag., 113,* 561–568, 1976.

Fryer, P., J. A. Pearce, L. B. Stokking, et al., Conical Seamount: SeaMARC II, Alvin Submersible, and seismic-reflection studies, *Proc. ODP, Init. Repts.*, vol. 125: College Station, TX (Ocean Drilling Program), 69–80, 1990.

Hobbs, B. E., W. D. Means, and P. F. Williams, *An outline of structural geology*, 571 pp., John Wiley & Sons, Inc, New York, 1976.

Hsui, A. T., and S. Youngquist, A dynamic model of the curvature of the Mariana Trench, *Nature, 318,* 455–457, 1985.

Hussong, D. M., and P. Fryer, Back-arc seamounts and the SeaMARC II seafloor mapping system, *EOS, Trans. Am. Geophys. Union, 64,* 627–632, 1983.

Hussong, D. M., and S. Uyeda, Tectonic processes and the history of the Marinana arc: A synthesis of the results of deep sea drilling project leg 60, in *Initial Rep. Deep Sea Drill Proj.*, vol. 60, 909–929, 1981.

Isacks, B. L., J. Oliver, and L. R. Sykes, Seismology and the new global tectonics, *J. Geophys. Res., 73,* 5855–5900, 1968.

Jackson, M. C., *Petrology and petrogenesis of recent submarine volcanics from the northern Mariana arc and back-arc basin*, Dissertation, University of Hawaii, 277 pp., 1989.

Jarrard, R. D., Causes of compression and extension behind trenches, *Tectonophysics, 132,* 89–102, 1986.

Johnson, H. P., and M. Helferty, The geological interpretation of side-scan sonar, *Rev. Geophys., 28,* 357–380, 1990.

Karig, D. E., R. N. Anderson, and L. D. Bivee, Characteristics of back arc spreading in the Mariana Trough, *J. Geophys. Res., 83,* 1213–1226, 1978.

Kelsey, H. M., and G. A. Carver, Late Neogene and Quaternary tectonics associated with northward growth of the San Andreas transform fault, northern California, *J. Geophys. Res., 93,* 4797–4819, 1988.

Krantz, R. W., Multiple fault sets and three-dimensional strain: theory and application, *J. Structural Geol., 10,* 225–237, 1988a.

Krumbein, W. C., Prefered orientation of pebbles in sedimentary deposits, *Jour. Geology, 47,* 673–706, 1939.

Kuramoto, S., and K. Konishi, The southwest Ryukyu Arc is a migrating microplate (forearc sliver), *Tectonophysics, 163,* 75–91, 1989.

Kusznir, N. J., and R. G. Park, The extensional strength of the continental lithophere: its dependense on geothermal gradient, and crustal composition and thickness, in *Continental Extensional Tectonics*, Geological Society Special Publication No. 28, edited by M. P. Coward, J. F. Dewey and P. L. Hancock, 35–52, 1987.

Lowell, J. D., *Strucural styles in pretroleum exploration*, 477 pp., OGCI Publications, Oil and Gas Consultants International, Inc., Tulsa, 1985.

Malinverno, A., and W. B. F. Ryan, Extension in the Tyrrhenian Sea and shortening in the Apennines as result of arc migration driven by sinking of the lithosphere, *Tectonophysics, 5,* 227–245, 1986.

Molnar, P., and T. Atwater, Interarc spreading and Cordilleran tectonics as alternates related to the age of subducted oceanic lithosphere, *Earth Planet. Sci. Let., 41,* 330–340, 1978.

Oertel, G., The mechanism of faulting in clay experiments, *Tectonophysics, 2,* 343–393, 1965.

Oliver, J., and B. Isacks, Deep earthquake zones, anomalous structures in the upper mantle, and the lithosphere, *J. Geophys. Res., 72,* 4259–4275, 1967.

Ramsey, J. G., *Folding and fracturing of rocks*, 412 pp., McGraw-Hill, New York, 1967.

Reches, Z., Faulting of rocks in three-dimensional strain fields II. Theorectical analysis, *Tectonophysics, 95,* 133–156, 1983.

Reches, Z., and J. H. Dieterich, Faulting of rocks in three-dimensional strain fields I. Failure of rocks in polyaxial, servo-control experiments, *Tectonophysics, 95,* 111–132, 1983.

Reed, T. B., and D. Hussong, Digital image processing techniques for enhancement and classification of SeaMARC II side scan sonar imagery, *J. Geophys. Res., 94,* 7469–7490, 1989.

Rosendahl, B. R., Architecture of continental rifts with special reference to East Africa, *Ann. Rev. Earth Planet. Sci., 15,* 445–503, 1987.

Sender, K. L., A. N. Shor, and R. A. Hagen, SeaMARC II side-scan processing techniques, *EOS Trans. Am. Geophys. Un., 70,* 1304, 1989.

Sibuet, J., J. Letouzey, F. Barbier, J. Charvet, J. Foucher, T. W. Hilde, M. Kimura, C. Ling-Yun, B. Marsset, C. Muller, and J. Stephan, Back arc extension in the Okinawa Trough, *J. Geophys. Res., 92,* 14041–14063, 1987.

Smoot, N. C., The growth rate of submarine volcanoes on the South Honshu and East Mariana ridges, *J. Volcanol. Geotherm. Res., 35,* 1–15, 1988.

Smoot, N. C., Mariana Trough by multi-beam sonar, *Geo-Marine Let., 10,* 137–144, 1990.

Stern, R. J., P. Lin, J. D. Morris, M. C. Jackson, P. Fryer, S. H. Bloomer, and E. Ito, Enriched back-arc basin basalts from the northern Mariana Trough: implications for the magmatic evolution of back-arc basin, *Earth Planet. Sci. Lett., 100,* 210–225, 1990.

Stern, R. J., N. C. Smoot, and M. Rubin, Unzipping of the Volcano arc, Japan, *Tectonophysics, 102,* 153–174, 1984.

Tucker, P. M., and H. J. Yorston, *Pitfalls in seismic interpretation*, Monogrph Series, vol. 2, 50 pp., Soc. Exploration Geophys., Tulsa, 1973.

Upton, G. J. G., and B. Fingleton, *Spatial data analysis by example: catagorical and directional data*, vol. 2, 416 pp., John Wiley & Sons, Chichester, 1989.

Vogt, P. R., A. Lowrie, D. R. Bracey, and R. N. Hey, Subduction of aseismic oceanic ridges: effects on shape, seismicity, and other characteristics of consuming plate boundaries, *Geol. Soc. Am. Spec. Paper, 172,* 1–17, 1976.

Vogt, P. R., and B. E. Tucholke, Imaging the ocean floor: History and state of the art, in *The geology of North America*, vol. M, edited by P. R. Vogt and B. E. Tucholke, 19–44, Geol. Soc. Am., 1986.

Weissel, J. K., and G. D. Karner, Flexural uplift of rift flanks due to mechanical unloading of the lithosphere during extension, *J. Geophys. Res., 94,* 13919–13950, 1989.

Wessel, P., and J. K. Wessel, On the determination of multible modes in circular data, *J. Structural Geol.,* submitted.